ENGINE BEARING ANALYSIS AND DESIGN

by

Gary Alan Clayton

Thesis submitted to the University of Leeds
for the degree of Doctor of Philosophy

The University of Leeds
Department of Mechanical Engineering
Leeds LS2 9JT

February 1990

SYNOPSIS

The work described in this thesis, Engine Bearing Analysis and Design, is directed towards the prediction of the performance characteristics of full central circumferentially grooved journal bearings. Due to the complexities of a full solution of such bearings, several simplifications have been made, including the assumptions of rigid circular journal and bearing and that a thin isoviscous Newtonian lubricant exists between the bounding solids.

The work presented can be split into three main areas of research. These are theoretical predictions in relation to the performance predictions of steadily and dynamically loaded cases, and the subsequent verification of the transient solution techniques developed by carrying out an extensive experimental investigation. The tests were carried out on the front main bearing of a single cylinder engine; the Ricardo Hydra.

For the research into the performance of steadily loaded journal bearings, extensive design charts have been generated for the dimensionless load and shear power loss variation with eccentricity ratio at a range of dimensionless oil supply pressures. The total oil flow rate data, considering coupled surface velocities and oil supply pressure, was found to be represented accurately by a single curve. There was only a 4% difference between this and the pressure flow equation. The cavitation algorithm of Elrod and Adams (1974) was used for this part of the research work, with a view to its extension to transient cases. However, the excessive time required for a solution point meant that it would be impractical for transient situation where it would be solved several hundred times for a complete journal orbit.

Subsequent to the analysis of steadily loaded bearings, attention was focused on the solution of dynamically loaded cases. A simplified oil film history solution was developed which reduced the computer run time for a converged journal centre orbit considerably. In addition, simple preditive techniques have been developed based on the pressure flow equation and a fully flooded bearing for purposes of shear power loss predictions. This approach for the full central circumferentially grooved bearings considered gave excellent agreement with the more rigorous analysis.

The transient analyses developed have been verified by comparison with a significant amount of experimental data which was collected for the front main bearing of a single cylinder gasoline engine. It was found that simple expressions for the oil flow rate and power loss provided a good prediction of the experimental data. There was found to be no justification in carrying out a rigorous film history solution, and from a design point of view the range of tolerances on the journal and bearing could give a diametral bearing clearance which could vary by a factor of 2.4. This has a more significant effect on the bearing side leakage than any uncertainties involved in the performance predictions themselves.

CONTENTS

CHAPTER 3 THE MOBILITY METHOD

CHAPTER 4 THE FILM HISTORY SOLUTION

CHAPTER 5 EVALUATION OF THE AUTHOR'S PREDICTIVE TECHNIQUES

CHAPTER 6 THE TEST ENGINE AND EXPERIMENTAL INVESTIGATION

CHAPTER 7 ANALYSIS AND DISCUSSION OF THE EXPERIMENTAL DATA

CHAPTER 8 CONCLUSIONS AND SUGGESTIONS FOR FUTURE WORK

List of Tables

List of Figures

Page No.

NOTATION

b	Bearing width (1 land)
c	Bearing radial clearance
C_d	Bearing diametral clearance
C_p	Oil specific heat
d	Bearing diameter
e	Eccentricity
g	Switch function
$h, h_{cav}, h_{min}, h_{max}$	Oil film thicknesses (general, cavitation, minimum and maximum)
H, H_{SH}, H_{SQ}, H_p	Power Loss (total, shear, squeeze and pressure induced components)
$J_1^{00}, J_3^{11}, J_3^{02}, J_3^{20}$	Journal bearing integrals
K	Proportion of power loss transmitted to the journal and bearing surfaces
$M, M^x, M^y, M^\epsilon, M^\phi$	Mobilities
P, P_s	Oil pressure and oil supply pressure
Q, Q_p, Q_s, Q_T, Q_v	Oil flow rates (total, pressure, steady state, translational and velocity components)
r	Bearing radius
R_f	Relaxation factor
t	Time
T_{in}, T_o	Oil temperatures (bearing inlet and outlet)
T_{av}, T_e, T_5	Efffective oil temperatures
U, U_B, U_s	Surface velocities (total, bearing and shaft)
V	Journal centre velocity
w	Bearing specific load
W, W_A, W_N	Bearing load (total and along and normal to the journal/bearing line of centres)

β	Oil bulk modulus (Chapter 2). Angle between load line and bearing/journal line of centres. (Chapter 3)
γ	Sommerfeld angle
η	Oil dynamic viscosity
$\theta, \theta_1, \theta_2$	Angles measured from maximum oil film thickness position (General, film reformation and film rupture) (Chapter 3)
$\theta, \theta_T, \theta_{T+1}$	Dimensionless oil density or proportion of a mesh square full of oil, (General and on successive iterations)
ν	Oil kinematic viscosity (centistokes cS)
ρ, ρ_c	Oil density (General and at cavitation pressure)
ϕ	$\dot{\psi} - \bar{\omega}$
ψ	Attitude angle
$\bar{\omega}$	$\frac{\Omega_s + \Omega_B}{2} - \omega_L$
ω_L	Load angular velocity
Ω_B, Ω_s	Bearing and shaft rotational velocities
$-$	above a character denotes a normalized quantity
$\cdot$	above a character denotes rate of change (d/dt)

SI units are used throughout this thesis except for the oil kinematic viscosity, (ν), which is in centistokes (cS). The notation followed is that used widely in the available literature. Hence, the same symbol has been used for two different variables in several cases. Where this occurs close to each other in the text an explanation is given.

Dimensionless Groups

$$\bar{H} = \frac{H\left(\frac{c}{r}\right)}{bd^2\eta\Omega} \qquad \bar{P} = \frac{P\left(\frac{c}{r}\right)^2}{\eta\Omega}\text{(steady)} \qquad \bar{P} = \frac{P\left(\frac{c}{r}\right)^2}{\eta\dot{\phi}}\text{ (dynamic)}$$

$$\bar{Q} = \frac{Q\eta}{Pc_d^{\,3}} \qquad \bar{W} = \frac{W\left(\frac{c}{r}\right)^2}{bd\eta\Omega} \qquad \bar{\beta} = \frac{\beta\left(\frac{c}{r}\right)^2}{\eta\Omega}$$

ACKNOWLEDGEMENT

I would like to express my appreciation to my thesis supervisor, Dr. C.M. Taylor, for his advice and guidance throughout the course of this research work.

The suggestions made by Mr. A.R. Heath and Mr. D.J. Lacy of Ricardo Consulting Engineers plc are gratefully acknowledged.

I would like to thank Mr. R.T. Harding for his help in the specification of the test engine modifications and the engine instrumentation. His work on the detailed design is acknowledged with thanks. The technical assistance of the staff of the Department of Mechanical Engineering (University of Leeds) and Ricardo Consulting Engineers plc is also acknowledged with thanks.

The assistance of Mr. R.J. Catchpole (Ricardo Consulting Engineers plc) during the experimental part of this work is gratefully acknolwedged.

This thesis has been typed by Mrs. C.M. Goulborn and Mrs. S. Moore. Their help and patience in typing the numerous tables and sinuous equations is appreciated.

I am indebted to each and everyone of these people. My apologies to anyone omitted from these acknowledgements.

CHAPTER 1

CHAPTER 1

INTRODUCTION

1.1 Reynolds' Equation

The equation governing the pressure generation in a thin viscous film was first derived by Osborne Reynolds (1886). The resulting equation is a 2nd order partial differential equation, which provides an equilibrium of the pressure and viscous shear forces acting on an a elemental package of fluid, in addition to ensuring continuity of lubricant flow in the oil film. Reynolds' equation may be written as:-

$$\frac{\partial}{\partial x}\left(h^3 \frac{\partial P}{\partial x}\right) + \frac{\partial}{\partial y}\left(h^3 \frac{\partial P}{\partial y}\right) = 6\eta U \frac{dh}{dx} + 12\eta \frac{dh}{dt} \qquad (1.1)$$

Equation 1.1 is for an isoviscous, incompressible fluid and relates the film pressure (P) to the film thickness (h), the oil dynamic viscosity (η), the bounding surface velocities ($U = U_S + U_B$) and the rate of change of the oil film thickness (dh/dt).

For the case of a fluid film journal bearing subjected to a load (W) and with journal and/or bearing rotation, the journal centre takes up an eccentric position within the bearing. This is denoted by (e) or in dimensionless form by,

$$\varepsilon = \frac{e}{c} \qquad (1.2)$$

where (c) is the radial clearance between the journal and bearing surfaces. The motion of the surfaces causes lubricant to be drawn into the convergent gap between the journal and bearing surfaces and hydrodynamic film pressures are generated. These balance the externally applied load. This is shown diagramatically in Figure 1.1.

The calculation of the bearing performance characteristics is based on determining the pressure distribution in the lubricant film by integration of Equation 1.1. An approximate, analytical solution can be effected using the 'short' journal bearing theory of Dubois and Ocvirk (1953). This is valid for bearings with a small width-to-diameter ratio, and in such cases the circumferential pressure gradients are considered to be negligible in comparison with the axial pressure gradients.

The 'infinite' bearing assumption also provides an approximate analytical solution to the Reynolds equation. For this approximate solution the axial pressure gradient is considered to be zero, and hence, this approximation is applicable to bearings of very large width-to-diameter ratios.

However, with the advent of digital computers, solutions in which the pressure gradients in both the axial and circumferential directions are considered are now possible. Such solutions may involve expressing the Reynolds equation in finite difference form and solving the resulting system of equations using the Gauss-Seidel technique.

1.2 Boundary Conditions for the Reynolds Equation

In hydrodynamic journal bearings the oil film may not remain continuous due to the formation of air cavities in the divergent part of the bearing clearance. This is caused by

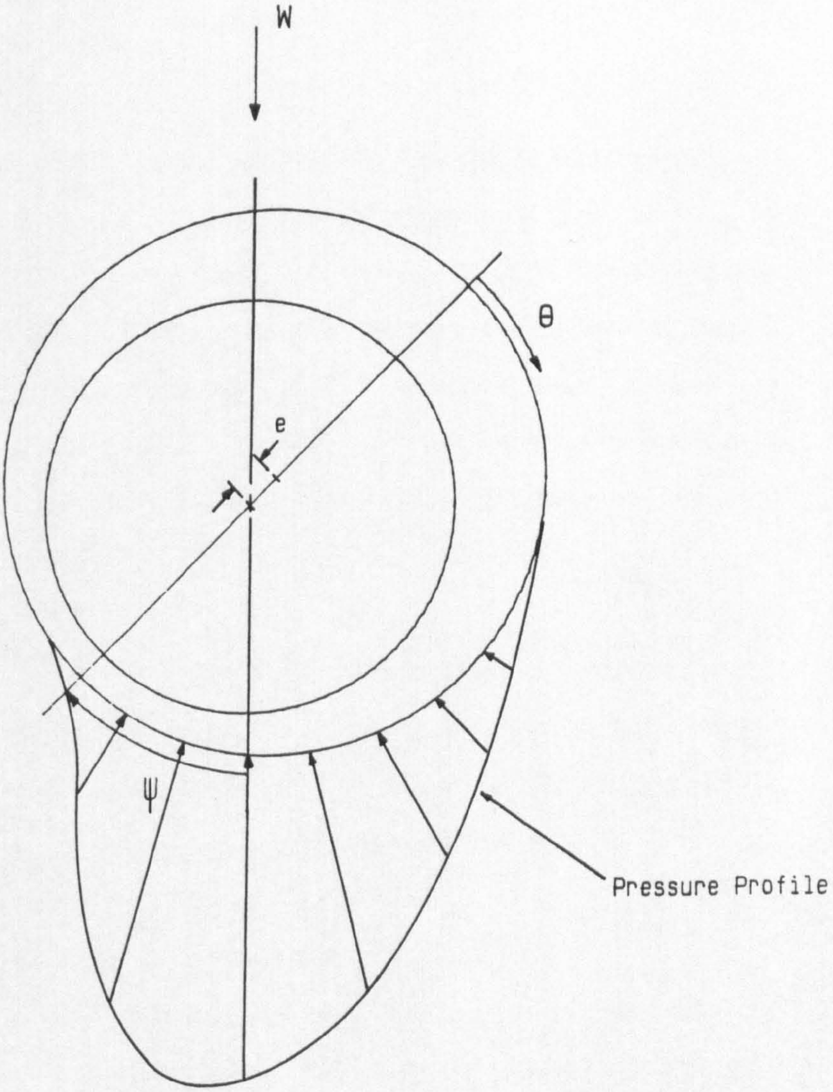

Figure 1.1 Pressure Generation In A Fluid Film Journal Bearing.

insufficient oil being available to provide a full width oil film, and hence, the oil flows in streamers (or striations) through this region. This is shown for the case of a full circumferential groove bearing in Figure 1.2.

For a steadily loaded bearing the cavitation region usually starts downstream of the minimum film thickness position, at what is termed the rupture boundary, and the lubricant film re-establishes at the position where sufficient oil becomes available to form a full width film. This is termed the reformation boundary and for the case shown in Figure 1.2 can be seen to be in the divergent region. The actual position is dependent on the bearing geometry and operating characteristics.

Hence, it can be seen that imposing the correct boundary conditions on the Reynolds equation requires the correct positioning of the cavitation region. Several boundary conditions are shown diagramatically in Figure 1.3 and are discussed below:-

(i) **Sommerfeld Boundary Condition**

A fully flooded bearing is assumed and the oil is considered to be able to sustain large sub-ambient pressures. Hence an anti-symmetric pressure profile is obtained in the bearing.

(ii) **Gümbel-Everling (½ Sommerfeld)**

The pressure is considered to be generated in the convergent film region between the maximum and minimum film thickness positions.

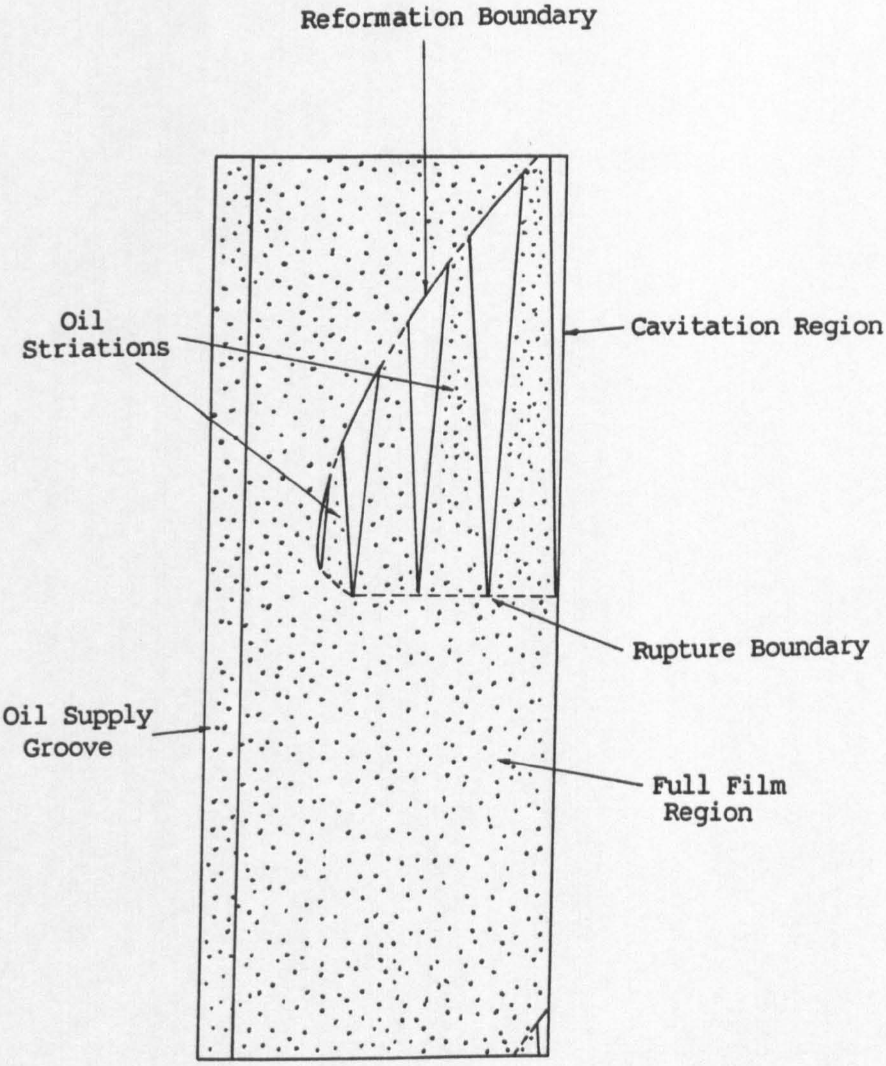

Figure 1.2 Cavitation Region In Full Circumferentially Grooved Bearing

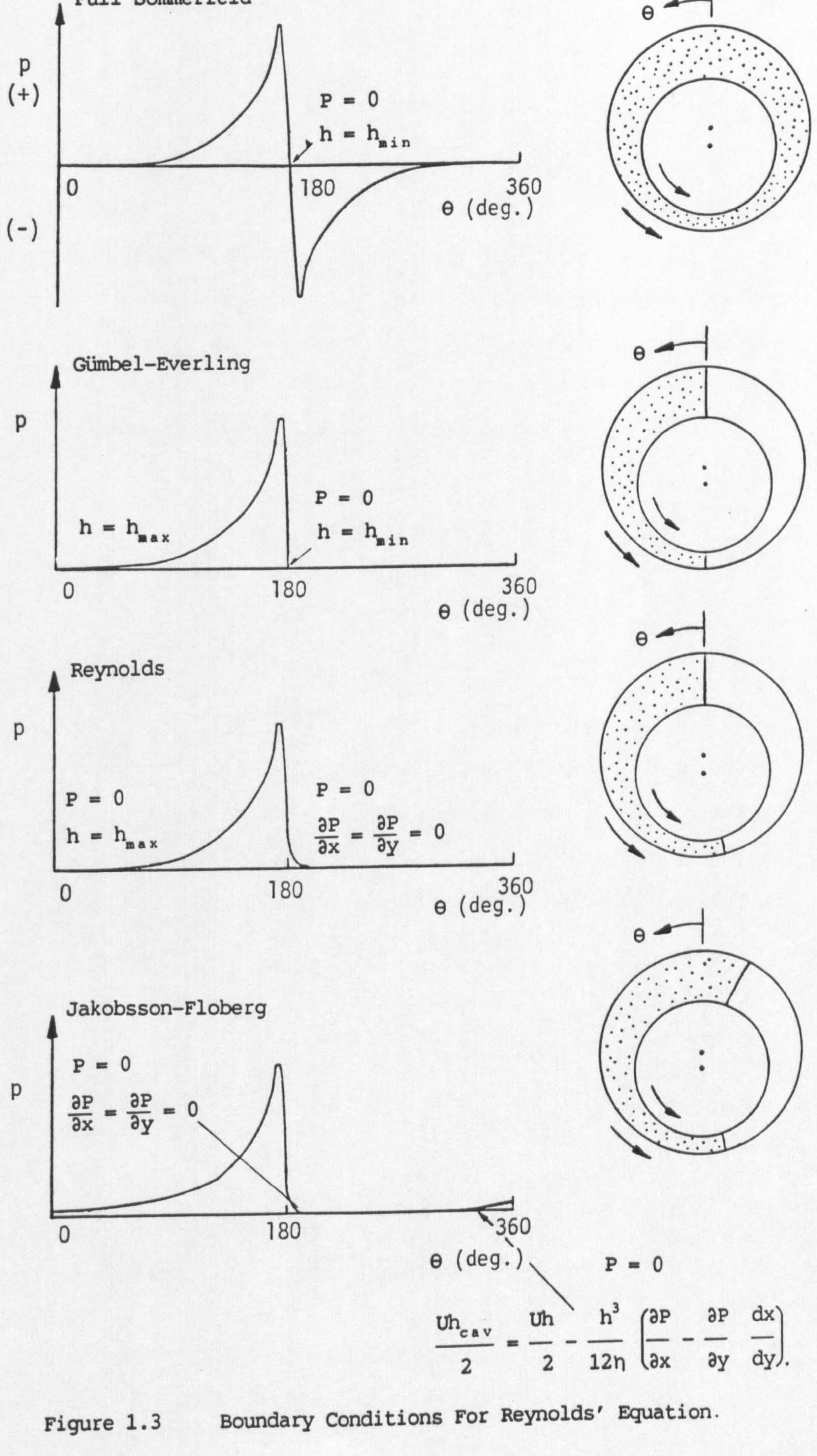

Figure 1.3 Boundary Conditions For Reynolds' Equation.

(iii) Reynolds' Boundary Condition

The lubricant film is assumed to cavitate at the cavitation pressure (P_c) and the pressure gradients at rupture are set equal to zero. (The cavitation pressure is usually considered to be equal to the atmospheric gauge pressure). The reformation boundary can easily be positioned at the maximum film thickness position or by setting the pressure gradients at reformation to zero. Hence, the boundary conditions for the latter case are:-

$$\left.\begin{array}{l} P = 0 \\ \dfrac{\partial P}{\partial x} = \dfrac{\partial P}{\partial y} = 0 \end{array}\right\} \text{ at rupture and reformation} \qquad (1.3)$$

(iv) Jakobsson - Floberg (1957)

Jakobsson and Floberg applied the principle of oil flow continuity at film rupture and reformation to derive their boundary conditions. It was assumed that in the cavitation region the pressure was equal to the cavitation pressure (P_c) and that the oil flowed in a number of thin streamers. The boundary conditions derived were:-

$$\left.\begin{array}{l} P = 0 \\ \dfrac{\partial P}{\partial x} = \dfrac{\partial P}{\partial y} = 0 \end{array}\right\} \text{ at rupture}$$

and (1.4)

$$\left.\begin{array}{l} P = 0 \\ \dfrac{Uh_{CAV}}{2} = \dfrac{Uh}{2} - \dfrac{h^3}{12\eta}\left(\dfrac{\partial P}{\partial x} - \dfrac{\partial P}{\partial y}\dfrac{dx}{\partial y}\right) \end{array}\right\} \text{ at reformation}$$

(v) Jakobsson - Floberg - Ollson Boundary Condition

For the case of a dynamically loaded bearing, where the rupture and reformation boundary positions are changing with time, Ollson (1965) derived boundary conditions based on oil flow continuity considerations. The analysis was similar to that of Jakobsson and Floberg (1957) and hence the boundary conditions are referred to as the Jakobsson-Floberg-Ollson (JFO) boundary condition.

The 'film history' solution is often used to impose the (JFO) boundary condition. This involves the solution of the Reynolds equation and the determination of the cavitation boundary movements from the resulting Couette (velocity) and Poiseuille (pressure) oil flow rate components. This will be discussed in considerable detail in Chapter 4.

The consideration of cavitation in liquid lubricated bearings has, in the main, been restricted to approaches designed to locate the position of film rupture. While this may provide an accurate estimate of the bearing load capacity, and even power loss for certain operating parameters, the predictions of the bearing oil side leakage can show significant discrepancies when compared with predictions where film reformation is considered. The reason for this is that for load capacity calculations an accurate prediction of the rupture boundary is required, since this is the region of high film pressure generation. Similarly, for oil flow rate predictions, the reformation boundary position must be predicted accurately. The axial flow rate in the vicinity of the reformation boundary is a significant proportion of the total flow rate, and its accurate determination depends upon a precise location of the boundary.

1.3 The Design of Steadily Loaded Journal Bearings

A comprehensive procedure for hydrodynamic journal bearing design has been available for some time (ESDU Item No.66023 (1966)). This approach enables data obtained from solutions of the Reynolds equation (taking the lubricant as isoviscous) to be employed in conjunction with an iterative thermal balance. The design document covers a spectrum of potential feed groove arrangements including a full central circumferential groove. However, certain limitaions of the quantitative information are apparent. It has been assumed that the load capacity and power loss for a full circumferential groove bearing can be taken to be the same as for a bearing with a groove at the maximum film thickness position. In addition, for this oil feed arrangement an engineering judgement (without justification in depth) was adopted to determine the oil flow rate. This method will now be discussed.

It has become the custom in determining the flow rate required by a journal bearing to sum two separate components, the pressure and velocity induced elements. This is, strictly speaking, inaccurate because the differing boundary conditions for the independent solutions means they may not be linearly added. The pressure flow (Q_p) is that induced into the bearing clearance space by virtue of the lubricant supply pressure, taking surface velocities to be zero. The velocity induced flow component (Q_v) is that which results from the surface motion with the supply pressure considered to be zero gauge. For the special case of a full fluid film, with no lubricant cavitation, the summation of these two components is precisely correct. Figure 1.4 depicts the two flow components for a full central circumferential groove bearing. The

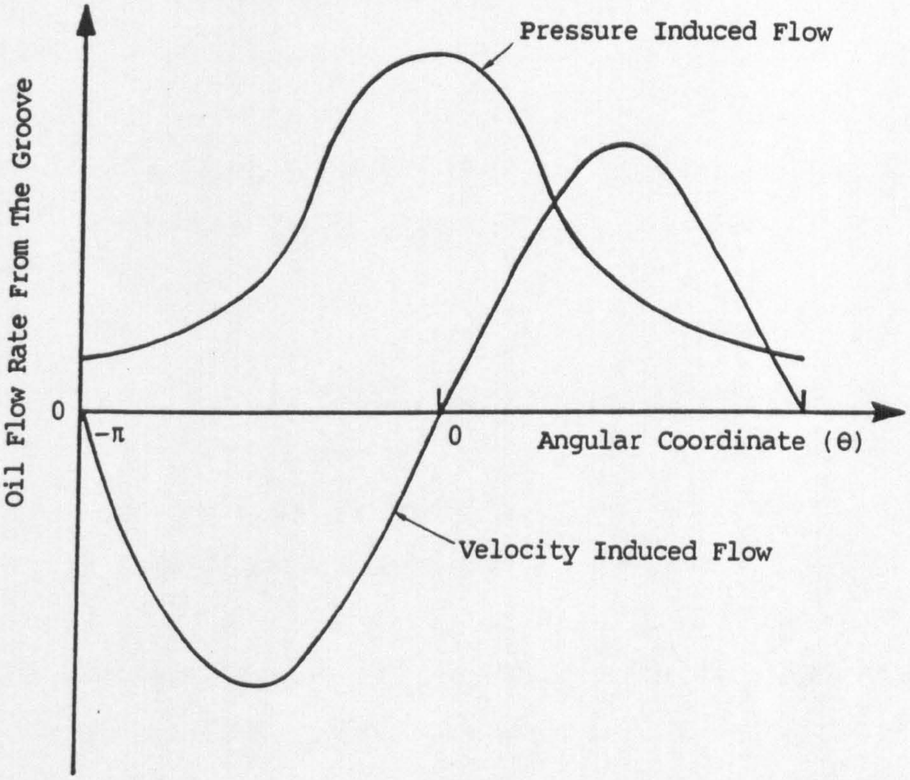

Figure 1.4 Oil Flow In Full Circumferential Groove Bearing

film thickness variation around the bearing is given by,

$$h = c + e \cos\theta \qquad (1.5)$$

with $\theta = 0$ at the maximum film thickness position. The symmetry of the film shape about the line of the bush and journal means that:-

(i) The pressure induced flow rate peaks at the maximum film thickness position and is symmetrical on either side of this.

(ii) The velocity induced flow rate is anti-symmetrical about the line of centres. This is due to the generation of positive gauge pressures in the converging film region and negative gauge pressures in the divergent region.

Such considerations are only true for a full fluid film where no cavitation occurs. It will be seen from Figure 1.4 that the velocity induced flow rate into the groove in the converging film region is balanced by that from the groove in the diverging region. The total flow rate may therefore be calculated by determining the pressure flow component (Q_p).

The approach outlined above was adopted in ESDU Item No. 66023 (1966), even though it was recognised that cavitation will occur for the vast majority of situations, and that the arguments underpinning the method of flow prediction might therefore be unsound. According to the above scheme the pressure induced flow rate was given by,

$$Q_p = 0.0327 \frac{P_s c_d^3}{\eta} \left(\frac{d}{b} \right) (1.5\varepsilon^2 + 1) \qquad (1.6)$$

where (b) is the width of one bearing load, and the flow is from one side of the bearing only. In due course this design document was replaced by ESDU Item No.84031(1984) which omitted any consideration of bearings with circumferential grooving. This reflected uncertainty concerning design data for such grooving situations.

1.4 The Design of Dynamically Loaded Journal Bearings

In the analysis of dynamically loaded journal bearings, such as those occurring in the internal combustion engine, the prediction of the shaft orbit and the minimum oil film thickness during the engine cycle have attracted much of the attention of designers. The mobility method of journal centre orbit determination (Booker(1965)) has been used extensively over a period of some twenty five years, firmly establishing itself as a practical design tool. A rapid solution to the orbit prediction is obtained, since the solutions of the governing Reynolds equation have been curve fitted to provide dimensionless ratios of journal centre velocity to the applied load.

However, the technique involves a series of assumptions and approximations and a proper consideration of oil flow continuity, incorporating film reformation and oil availability within the bearing, are not considered. Hence, researchers have developed more complex analysis techniques involving the solution of the Reynolds equation, perhaps several hundred times, to obtain a journal centre orbit. These techniques are, however, time consuming, and only find limited use, with the mobility method providing the designer with a useful everyday design aid.

1.5 Objectives of the Present Research Work

The trend towards smaller and lighter engine components, combined with the current increase in the computing power available to researchers and designers, means that there is a requirement for more rigorous design procedures for all engine components. The design of fluid film lubricated journal bearings is no exception to this optimization procedure, and the research work outlined in this thesis deals with the development of such a procedure. The envisaged objectives of the work in relation to a full central circumferential grooved bearing were:-

(1) The development of a simple preditive technique. This would be based on the mobility method and simple expressions for the prediction of the oil flow rate and power loss. This would provide a bench mark for the more complex work undertaken.

(2) A rigorous design procedure, incorporating a proper consideration of the cavitation region extent and movement within the bearing, was to be developed. However, the computer run time was to be kept to a minimum, and while film history considerations were to be accounted for, the analysis would still inevitably incorporate several assumptions. These would include limiting the analysis to rigid circular components with an iso-viscous incompressible Newtonian lubricant.

(3) An extensive experimental investigation was to be undertaken. This would involve the instrumentation on an

engine main bearing, and experimental data for the oil flow rate and temperature would be important parameters.

The present study is limited to the case of full central circumferentially grooved bearings. It is recognised that there is widespread use of partial circumferential groove and oil hole fed bearings and that there is a requirement for improved design data in relation to these.

CHAPTER 2

CHAPTER 2

STEADILY LOADED FULL CIRCUMFERENTIAL GROOVE JOURNAL BEARINGS

2.1 Introduction

The consideration of cavitation in liquid lubricated bearings has in the main been restricted to approaches designed to locate the position of film rupture, with relatively few design procedures attempting to account for the effects due to consideration of reformation of the lubricant film. The importance of an accurate determination of the film extent has been pointed out in Chapter 1, where various proposed boundary conditions were described. A widely accepted reformation boundary condition is that of Jakobsson and Floberg (JF), a condition derived from flow continuity considerations across the reformation interface.

Lundholm (1969), McCallion et al (1971), Elrod and Adams (1974), Ruddy (1979) and Miranda (1983) have all developed methods, or applied various techniques for imposing the (JF) boundary condition. From these, two main methods of approach can be identified. The first and most complex is that used by Lundholm (1969), McCallion et al (1971) and Ruddy (1979). This requires the solution of Reynolds' equation and the subsequent determination of pressure gradients or flow rates at the reformation boundary. Comparison of these conditions with those required to satisfy the (JF) boundary condition gives a criterion for the correct positioning of the reformation boundary. The second method, first suggested by Elrod and Adams (1974), and later refined by Elrod (1981), has the great advantage that it does not require explicit recourse to the rupture or reformation boundary conditions.

A universal differential equation which was applicable to the caviation and full film regions was developed.

Brief descriptions of both types of approach are given here. The first is a description in relation to the work of Ruddy (1979), the second is that of the cavitation algorithm of Elrod (1981), the analysis approach used initially in the present work for steadily loaded situations, with a view to development for application to transient conditions.

2.2 Ruddy's Solution Technique

Ruddy (1979) carried out a numerical analysis of circumferential groove bearings as part of a more extensive programme of work, concerning both static and dynamic analyses of various fluid film journal bearing types.

An initial estimate of the cavitation region extent was made by setting all negative gauge pressures obtained during the finite difference solution of Reynolds' equation to zero. A curve fit defined by a quadratic polynomial was then made to the first three non-zero pressures outside the cavitation region. This enabled the internodal position at which the pressure first falls the zero, and the pressure gradient at this point to be determined for each mesh line. A variable mesh size for nodes just outside the cavitation boundary had thus been set up, and the Reynolds equation was then applied to the new full film region. Thus, a converged solution for the pressure profile included the positioning of the reformation boundary.

For any converged pressure profile and cavitation region boundary the flows into the bearing at the groove, and out of the bearing at the edges were calculated. If a balance of oil flow within a preset tolerance was achieved the analysis was assumed to be completed. Otherwise, the pressure gradients on the reformation boundary were calculated from the (JF) boundary condition expression and compared with those determined from the curve fit polynomial. For internodal points where the agreement was within a preset tolerance the reformation boundary position was kept unchanged. For points where this was not the case, the boundary was moved so as to reduce the error.

The Reynolds equation was re-solved for the new cavitation region and the previously described method repeated until convergence of the axial flows into and out of the bearing was obtained.

2.3 Elrod's Cavitation Algorithm

A detailed description of the algorithm is given by Miranda (1983) and for this reason only a brief summary of the solution technique is given here. Elrod (1981) postulated the following expressions for the Couette and Poiseuille mass flow rate components (per unit width) in the (x) co-ordinate direction,

$$\dot{m}_{x_{\text{convective}}} = \frac{\rho_c U}{2} \left[\theta_{-1} h_{-1} \ (1-g_{-1}) + g_{-1} h_{-1} + \frac{g_o g_{-1}}{2} \ (h_o - h_{-1}) \right] \quad (2.1)$$

$$\dot{m}_{x_{\text{pressure}}} = \left(\frac{h^3}{12\eta} \right)_{\text{average}} \beta \rho_c \left[\frac{g_{-1} \ (\theta_{-1}-1) - g_o \ (\theta_o - 1)}{\Delta x} \right] \quad (2.2)$$

where Equation 2.2 has been obtained by the following substitution

$$P = \beta\,(\theta - 1) \tag{2.3}$$

This represents the relationship between the film pressure (P), bulk modulus (β), and the dimensionless oil density (θ). For points within the cavitation region this expression does not apply, the switch function (g) ensures that the pressure flow falls to zero, and (θ) in this case becomes the fractional film content, or proportion of any mesh square width (in the (y) co-ordinate direction) full of oil. The value of (g) was set according to Equations 2.4.

$$\left.\begin{array}{ll} g = 0 & \text{when } \theta < 1 \quad \text{(cavitated region)} \\ g = 1 & \text{when } \theta \geq 1 \quad \text{(full film region)} \end{array}\right\} \tag{2.4}$$

Equation 2.1, 2.2 and similar expressions for the (y) co-ordinate direction were then substituted into the continuity equation, which for a steadily loaded bearing is given by:-

$$\Delta\dot{m}_x\,\Delta y + \Delta\dot{m}_y\,\Delta x = \Delta x \Delta y h \,\frac{\partial(\rho\theta)}{\partial t} \tag{2.5}$$

The right hand side of the equation represents the gain in oil mass in the control volume considered, and for the final converged steady state solution will become equal to zero. For this reason Miranda (1983) ignored the term, but it was left in the equation in the current analysis. Normalization of Equation 2.5, after substitution of the expressions for the mass flow rates in the (x) and (y) co-ordinate directions allowed the following equation for $\theta_T(i,j)$ to be derived,

$$\theta_T(i,j) = \frac{\left(\frac{\pi}{24}\right)\Delta\overline{x\beta}\left(\frac{d}{\bar{b}}\right)^2 E12 + \left(\frac{\Delta\bar{y}}{2}\right)E10 + \left(\frac{\Delta\bar{y}}{192\pi}\right)\bar{\beta}\,E11 - \dfrac{2\pi\Delta\bar{x}\Delta\overline{yh}\,\theta_{T-1}(i,j)}{\Delta\bar{T}}}{\left(\frac{\pi}{24}\right)\Delta\overline{x\beta}\left(\frac{d}{\bar{b}}\right)^2 E9 + \left(\frac{\Delta\bar{y}}{2}\right)E8 + \left(\frac{\Delta\bar{y}}{192\pi}\right)\bar{\beta}\,E7 - \dfrac{2\pi\Delta\bar{x}\Delta\overline{yh}}{\Delta T}} \tag{2.6}$$

where
$$E7 = \frac{g_{i,j}\ (\bar{h}_j + \bar{h}_{j-1})^3 + g_{i,j}\ (\bar{h}_j + \bar{h}_{j+1})^3}{\Delta\bar{x}}$$

$$E8 = \bar{h}_j\ (1 - g_{i,j})$$

$$E9 = \frac{2\bar{h}_j{}^3 g}{\Delta\bar{y}}$$

$$E10 = E3 - E1$$

$$E11 = E2 + E4 + E7$$

$$E12 = E5 + E6 + E9$$

$$E1 = g_{i,j}\ \bar{h}_{i,j} + \frac{g_{i,j}\ g_{I,j+1}}{2}\ (\bar{h}_{j+1} - \bar{h}_j)$$

$$E2 = \frac{(\bar{h}_{j+1} + \bar{h}_j)^3\ g_{i,j+1}\ (\theta_{i,j+1} - 1)}{\Delta\bar{x}}$$

$$E3 = \theta_{i,j-1}\ \bar{h}_{j-1}\ (1 - g_{i,j-1}) + g_{i,j-1}\ \bar{h}_{j-1} + \frac{g_{i,j-1}\ g_{i,j}}{2}\ (\bar{h}_j - \bar{h}_{j-1})$$

$$E4 = \frac{(\bar{h}_j + \bar{h}_{j-1})^3\ g_{i,j-1}\ (\theta_{i,j-1} - 1)}{\Delta\bar{x}}$$

$$E5 = \frac{\bar{h}_j{}^3\ g_{i-1,j}\ (\theta_{i-1,j} - 1)}{\Delta\bar{y}}$$

$$E6 = \frac{\bar{h}_j\ g_{i+i,j}\ (\theta_{i+1,j} - 1)}{\Delta\bar{y}} \qquad (2.7)$$

Equation 2.6 is applicable to the whole of the lubrication regime and greatly simplifies the location of the reformation boundary. However, the boundary is never defined with a spacial tolerance of less than the grid spacing, which may provoke concern about the algorithms ability to mimic accurately the (JF) boundary condition. Elrod (1981) did however show that good accuracy can indeed be achieved for a mesh size of 20 x 8 (20 circumferential nodes x 8 axial nodes). Equation 2.6 was solved iteratively, and the solution was terminated when every node had converged according to the following criteria:-

$$g_T = g_{T-1}$$

$$\frac{|\ \theta_T - \theta_{T-1}\ |}{\theta_{T-1}} \leq \text{tolerance} \qquad (2.8)$$

For a converged (θ) profile the bearing load capacity, lubricant side flow rate and shear power loss were calculated.

2.4 Additional Description of Elrod's Algorithm Application with Respect to the Current Investigation of Full Circumferential Groove Bearings

Figure 2.1 shows a flow chart of the present solution technique. No detailed investigation was made into the optimum mesh size (M x N), relaxation factor (R_f) or dimensionless bulk modulus ($\bar{\beta}$). It was thought that a more worthwhile approach would be to produce design charts for a wide range of dimensionless input data. This, in so many cases has not been the approach, and several authors have only produced, or at least only published results relating to a few random cases. Miranda (1983) provided a detailed investigation into the effects of mesh size, relaxation factor and bulk modulus on the time to convergence and accuracy of the final solution. This was for the case of an axial groove bearing for which extensive design charts were also produced.

It was felt that with reference to published work, and without an extensive investigation, suitable values could be determined.

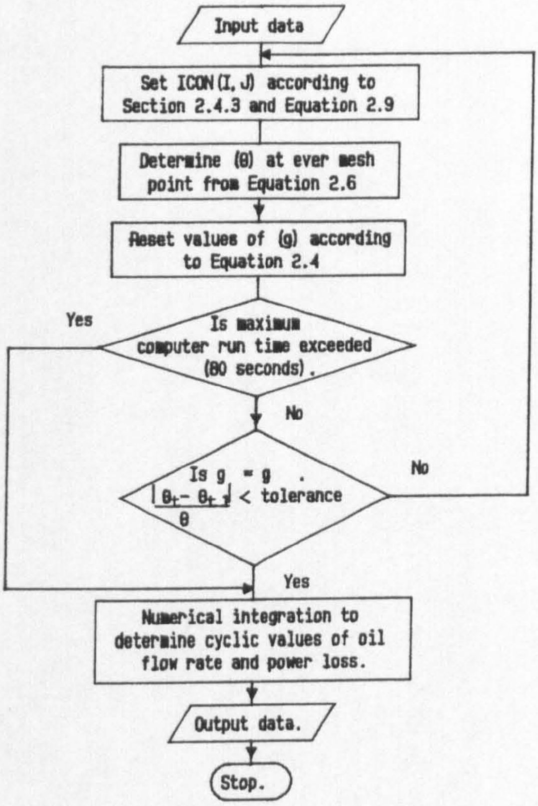

Figure 2.1 Flow Chart For Solution Of Elrod's Cavitation Algorithm.

2.4.1 Mesh Size

AUTHOR(S)	MESH SIZE
Lundholm (1969)	36 x 6
Ruddy (1979)	36 x 36
Elrod (1981) *	20 x 8
Miranda (1983) *	91 x 19 (Variable Mesh Size)
Jakeman (1984)	72 x 14
Vijayaraghaven and Keith (1988) *	61 x 6

* Elrod's Algorithm

Table 2.1 Mesh-sizes chosen by several authors

The final mesh size chosen for the present analysis was 51 x 11, a mesh size used for much of the work of Miranda (1983), although Miranda finally settled on a 91 x 19 variable mesh. The reasons for the choice are as follows:

(1) Several of the authors in Table 2.1 used mesh sizes more coarse than that used in the present work. Elrod (1981) used a 20 x 8 mesh which corresponded to a 18° circumferential mesh spacing. For a rupture or reformation boundary which lies between a node with a positive film pressure and a pressure equal to zero, the boundary could be incorrectly positioned by as much as $\pm 9^\circ$. However, the boundary is also constrained to lie between specific nodes in the axial direction, and this limits the positional tolerance of a curved boundary drawn between cavitated and non-cavitated nodes. Elrod (1981) gives examples to show that good accuracy can be achieved with this mesh spacing.

(2) Even though Miranda (1983) used a 91 x 19 variable mesh for the purpose of producing design data and charts, the finer mesh was only generated at the axial groove position. The reason for this was that in order to obtain accurate flow rate predictions, a mesh size giving at least 3 non-zero pressures within the full film region around the groove was required. For positions elsewhere in the bearing, the angular spacing of the mesh lines would not be significantly smaller than that used in the present work.

(3) Of the other referenced mesh sizes, only Jakeman (1984) used a significantly finer mesh in the circumferential direction, and Ruddy (1979) in the axial direction. Jakeman's fine mesh is considered excessive, while Ruddy (1979) probably chose a fine axial mesh as the pressure gradients for short bearings are changing more rapidly in the axial than circumferential direction.

(4) Trial and error using finer meshes gave little satisfaction in obtaining values of (β) and (R_f) which gave convergence for a wide range of input data.

2.4.2 Bulk Modulus (β) and (R_f)

The values of (β) and (R_f) used in the present analysis were 0.5 and 1.5 respectively. It was found that for a 51 x 11 mesh these valves gave converged solutions for most of the cases considered. Overflow (as encountered by Miranda (1983)) never occurred, although several points were encountered where the solution converged to the wrong (θ) profile. In addition, points which did not converge within the preset maximum program run time were found to be few in number, and always on the reformation boundary. This is discussed in more detail in Sections 2.4.3 and 2.4.4.

The values of (β) and (R_f) used by Miranda (1983) were significantly different to those used in the present analysis. Values of (β) as high as 50 were used, and Miranda (1983) suggested using a relaxation factor of 1. For relaxation factors slightly above 1.0 he reported overflow problems. In the present analysis it was found that the optimum values of (β) and (R_f) were 0.5 and 1.0. This provided convergence for most of the solution points.

The reasons for the differences in the optimum values of (β) and (R_f) between the analysis of Miranda (1983) and the present analysis have not been fully explored.

2.4.3 Introduction of an Additional Convergence Criterion

The two criteria for convergence of the solution are given by Equations 2.8. However, these criteria alone did not provide a satisfactory test for convergence, since several nodes on the reformation boundary converged very slowly, or did not converge within the preset maximum run time. It was found that some nodes on the reformation boundary remained unconverged several hundred iterations after the majority of those in the lubrication regime had satisfied the criteria. Time was therefore wasted by recalculating values of (θ) which were not changing from one iterative cycle to another.

Hence, a variable ICON(i,j) was introduced into the computer coding. After each iterative sweep through the finite difference mesh the variable ICON(i,j) was assigned to every node according to Equations 2.9.

$$\frac{|\theta_T - \theta_{T-1}|}{\theta_{T-1}} \leq \text{tolerance, then } \mathrm{ICON}_{(i,j)}=1$$

$$\frac{|\theta_T - \theta_{T-1}|}{\theta_{T-1}} > \text{tolerance, then } \mathrm{ICON},_{(i,j)} = 0 \qquad (2.9)$$

If the solution had not converged after 60 seconds computer run time, converged nodes were held constant, and only unconverged nodes iterated. The iterations were completed after an additional 20 seconds run time or when all the nodes converged, whichever was the sooner.

This additional coding produced beneficial results for some of the input parameters. However, some points still remained unconverged, usually due to just one node oscillating between the full film and cavitation region.

2.4.4 Effect of Unconverged Nodes on the Output Data

The effect of unconverged nodes is not expected to influence any of the output parameters by any significant amount. The nodes which may cause concern are always in the region of low hydrodynamic pressure generation, and will therefore have negligible effect on the bearing load capacity. The effect on shear power loss will also be negligible since the values of (θ) on consecutive iterative cycles were usually so close. To demonstrate this the case of a bearing with (b/d) equal to 0.2, operating at an eccentricity ratio of 0.4, and with a dimensionless groove pressure of 0.1 will be considered. In this case only one node oscillated between the full film and cavitation region, and after a computer run time of 80 seconds the value of (θ) on consecutive iterative cycles were 0.999991 and 1.01296. This caused other neighbouring nodes to oscillate, but these values were still converged to 0.1%.

The oscillations in (θ) will also have negligible effect on the predicted oil flow rate. For the case mentioned above the dimensionless oil flow rates were 0.197 from the bearing edge and 0.193 from the groove. The difference in the groove and side flow rates could, however, be as high as 5 or 10%, but this discrepancy was due to errors in the flow prediction at the groove. The proximity of the cavitation region and unconverged nodes to the oil supply groove meant that pressure gradients at the groove often had to be determined from curve fits to 2 or 3 nodes, as opposed to 4 at the bearing side. For this reason, the side flow rate was taken as the correct oil flow rate from the bearing.

2.5 Discussion and Presentation of Results

Computations were carried out for the following range of independent variables.

Bearing width to diameter ratio (b/d) = 0.1, 0.2, 0.3, 0.4, 0.5.

Dimensionless supply pressure $(\bar{P}_s)$ = (0.001), 0.01, 0.05, 0.1, 0.5, 1.0.

Eccentricity ratio (ε)=0.1 in steps of 0.1 to 0.9 in steps of 0.01 to 0.99.

A judgement had to be made upon the range of non-dimensional supply pressure to be examined. Two sample calculations presented in Table 2.2 will serve to illustrate the possibilities with an effective temperature of 60°C being assumed.

Supply Pressure (P_s) (N/m^2)	Diametral Clearance Ratio (c_d/d)	Lubricant ISO Grade	Dynamic Viscosity(η) at 60°C (Ns/m^2)	Rotational Frequency (Hz)	Non-dimensional Pressure ($\bar{P}_s$)
1×10^5	0.001	100	0.034	40	0.012
3×10^5	0.002	22	0.0096	20	1.0

Table 2.2 Sample calculations for non-dimensional supply pressure

2.5.1 Comparison with Some Previous Theoretical Results

Output from the computer program developed has been compared with the limited published results. Figures 2.2, 2.3 and 2.4 show a comparison of load capacity, shear power loss, and oil flow rate predicted during the current investigations with predictions made by several authors. The close agreement is apparent.

Figure 2.5 shows the variation of the product of the dimensionless flow rate ($\bar{Q}$) and the bearing (b/d) ratio in the range 0.1 to 0.5, and for dimensionless supply pressures of 0.01 to 3. The close agreement with the pressure flow equation of ESDU Item No. 66023 (1966) is apparent, and the scatter of the points is an indication of how universal the variation of dimensionless flow rate is with eccentricity ratio for the range of width-to-diameter ratios considered. It should be noted that for some input operating conditions the ESDU curve gave larger discrepancies than those shown in the figure.

In view of the previous discussion the general form of the pressure flow equation, given in ESDU Item No. 66023 (1966) and Martin and Lee (1982), is considered to describe accurately the

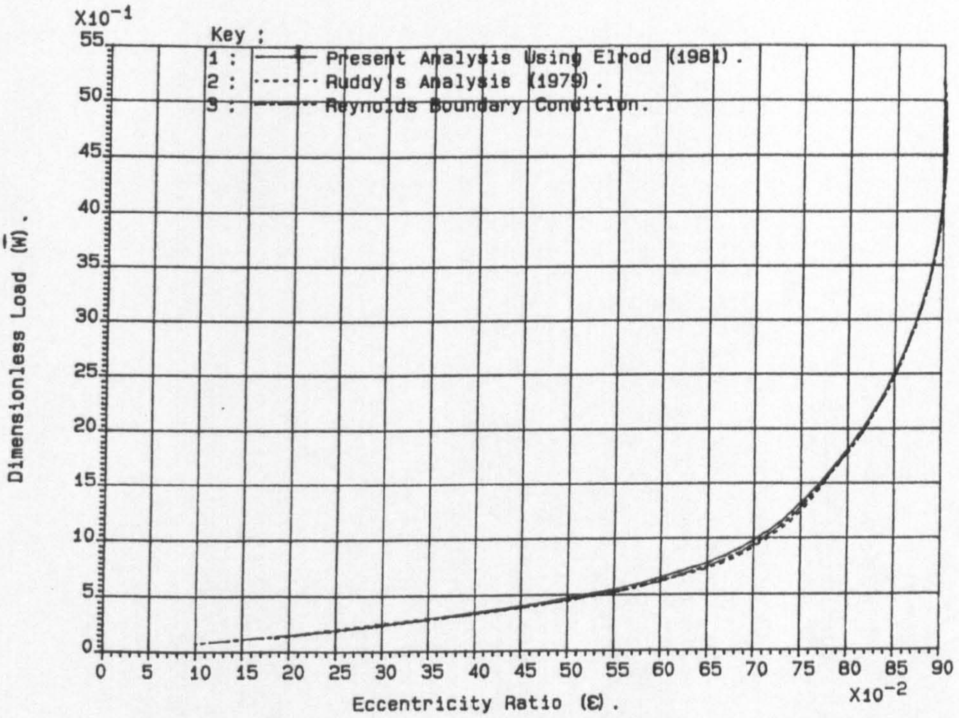

Figure 2.2 Dimensionless Load Variation With Eccentricity Ratio (b/d=0.5 $\bar{P}_s$ =1.0).

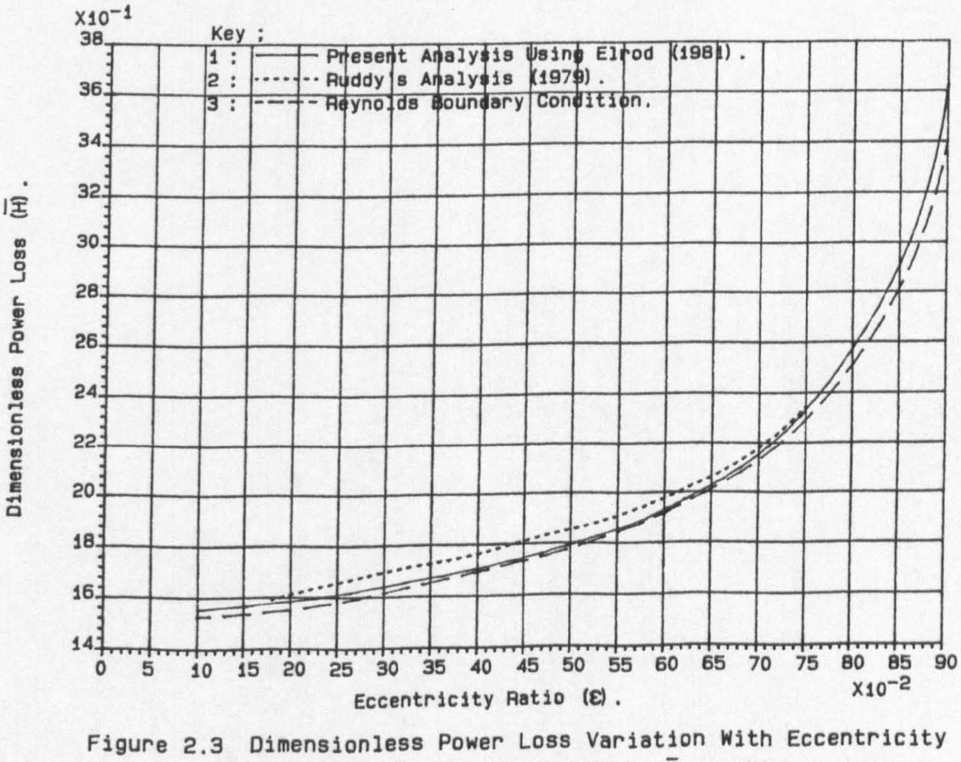

Figure 2.3 Dimensionless Power Loss Variation With Eccentricity Ratio (false origin b/d=0.5 $\bar{P}_s$ =1.0).

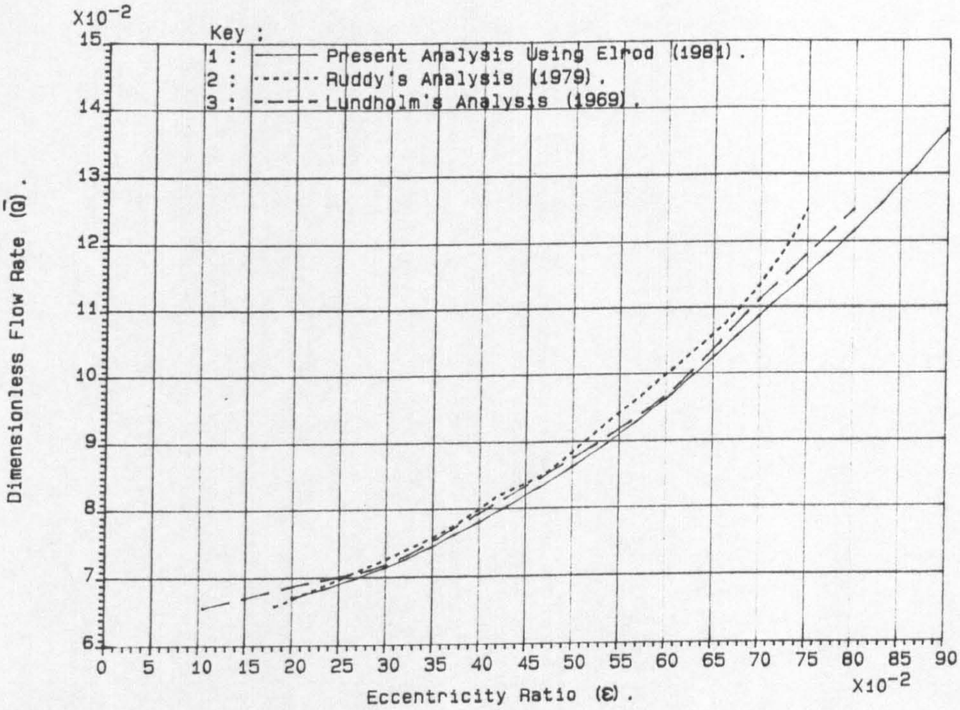

Figure 2.4 Dimensionless Flow Rate Variation With Eccentricity Ratio (false origin b/d=0.5 $\bar{P}_s$ =1.0).

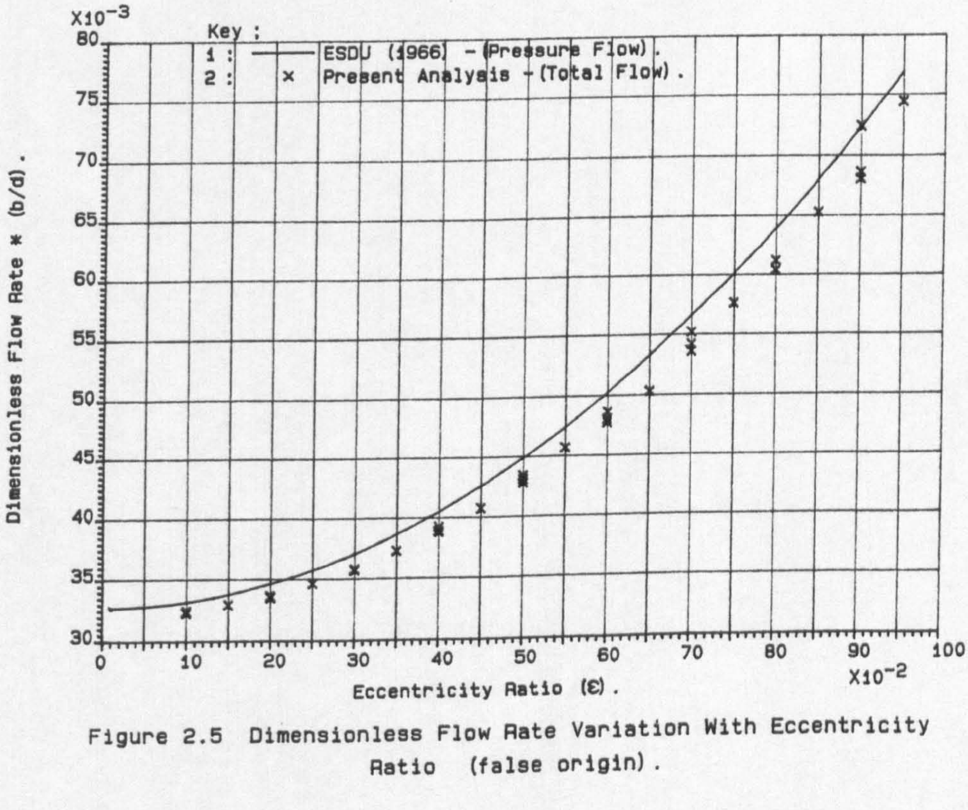

Figure 2.5 Dimensionless Flow Rate Variation With Eccentricity Ratio (false origin).

relationship between the dimensionless groups when calculating the total flow. However, the constant of proportionality (0.0327 in Equation 1.6) was refitted for the range of data generated in the present analysis.

For 200 values of $(\bar{Q})$ the constant which gave the least total squares deviation from the 200 dimensionless flow rates being curve fitted was determined. The value was 0.0315, which represents a difference of less than 4% when compared with the value given by the pressure flow equation of ESDU Item No. 66023 (1966). Hence, it is suggested that an appropriate curve fit to the generated data for total flow is,

$$Q = 0.0315 \frac{P_s \, c_d^{\,3}}{\eta} \left(\frac{d}{b} \right) (1.5\, \varepsilon^2 + 1) \qquad (2.10)$$

or in dimensionless form,

$$\bar{Q} = \frac{Q \, \eta}{P_s \, c_d^{\,3}} = 0.0315 \left(\frac{d}{b} \right) (1.5\, \varepsilon^2 + 1) \qquad (2.11)$$

where the flow is for one side of the bearing, and (b) is the width of one bearing land.

The sound judgement made by those responsible for ESDU Item No. 66023 (1966) in suggesting that the pressure induced flow rate, with no consideration of shaft rotation, be used to estimate the actual flow rate is now revealed. From an engineering design point of view the difference between the author's more precise determination of flow rate (Equation 2.10) and the approximation adopted in ESDU Item No. 66023 (1966) is insignificant.

2.5.2 Cavitation Region Extent Variation with Supply Pressure

Figures 2.6a and 2.6b show the extent of the cavitation

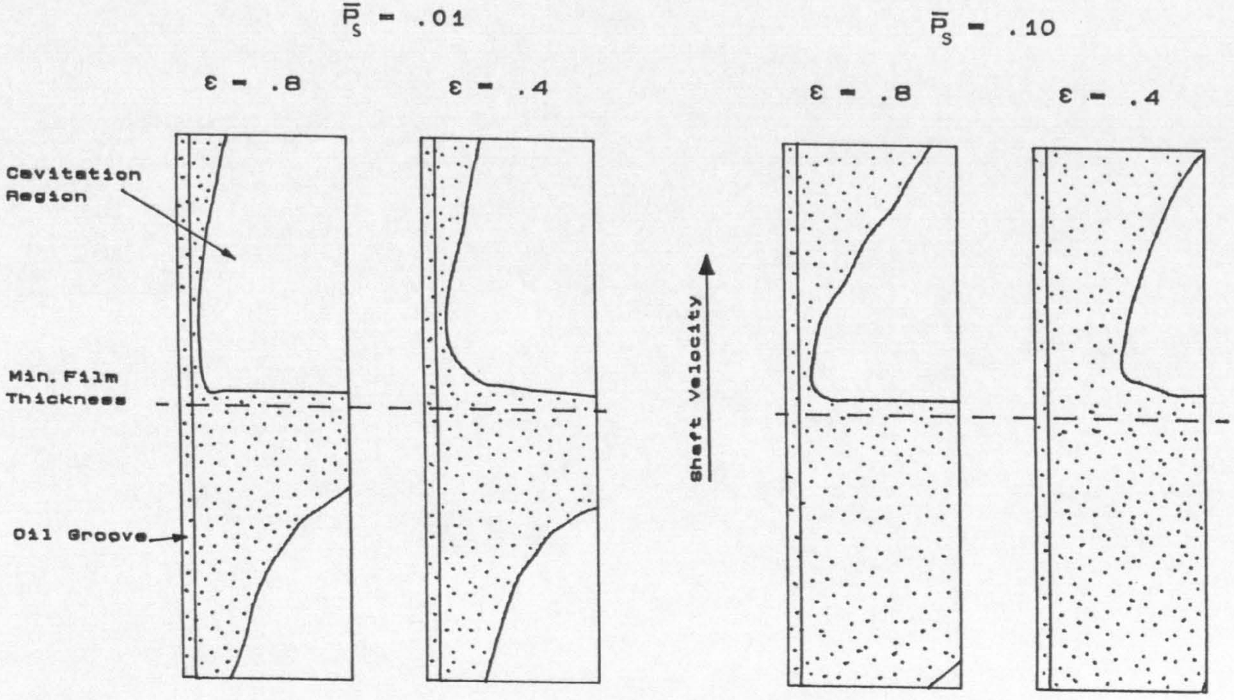

Figure 2.6a Cavitation Region Extent Variation With Eccentricity Ratio And Dimensionless Supply Pressure. (b/d=0.2).

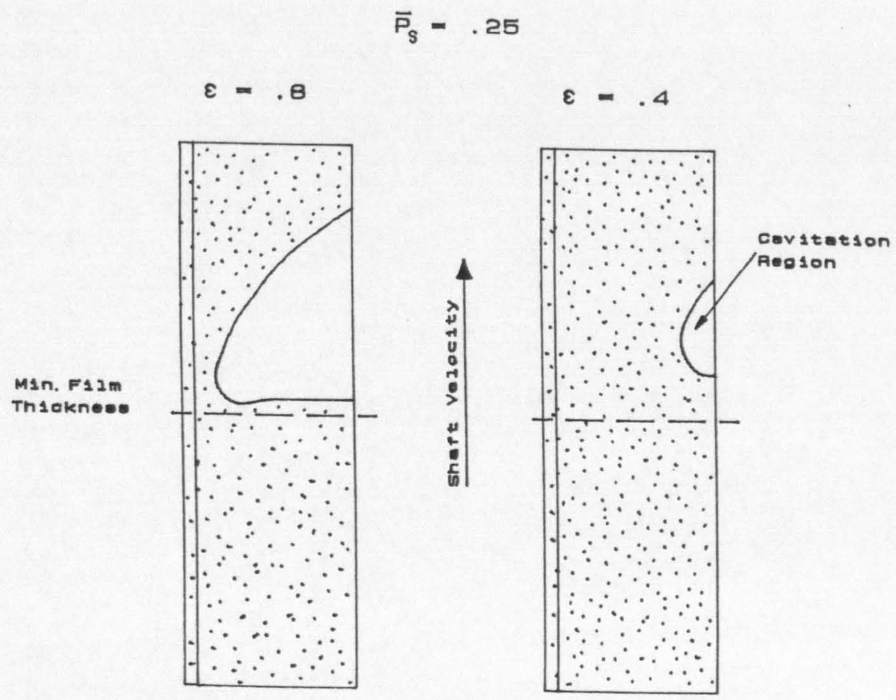

Figure 2.6b Cavitation Region Extent Variation With Eccentricity Ratio And Dimensionless Supply Pressure (b/d=0.2).

region on the developed bearing surface. The film rupture and reformation boundaries are shown for two ecentricity ratios (0.4 and 0.8) and three values of non-dimensional supply pressure (0.01, 0.10 and 0.25). As the dimensionless supply pressure increases for a given eccentricity ratio the size of the cavitation region decreases and at a sufficiently high supply pressure the film will become complete. For such a situation the argument developed previously (Chapter 1) to show why the pressure induced flow rate will represent the total flow rate will apply. What is not clear is why the pressure induced flow rate is such a good approximation to the total flow rate at low supply pressures when the region of cavitation is extensive, for example at a non-dimensional supply pressure case ($\bar{P}_s$ = 0.1) shown in Figure 2.6a.

2.5.3 Load Capacity and Power Loss

Figure 2.7 shows the effect of the (b/d) ratio on the bearing load capacity for a dimensionless supply pressure of 0.5. As would be expected there is a marked increase in load capacity with (b/d) for any eccentricity ratio. Additional data for dimensionless supply pressures of 0.01, 0.05, 0.1 and 1.0 are given in Appendix 1.

The variation of dimensionless load capacity with the ratio of supply pressue (P_s) to specific load (w) is shown in Figure 2.8. This is for a fixed eccentricity ratio of 0.4 and a bearing width to diameter ratio of 0.2. For a fixed geometry, dynamic viscosity and shaft rotational speed, an increase in supply pressure will cause the cavitation region to decrease in size and both the ratio of supply pressure to specific load and dimensionless load to increase.

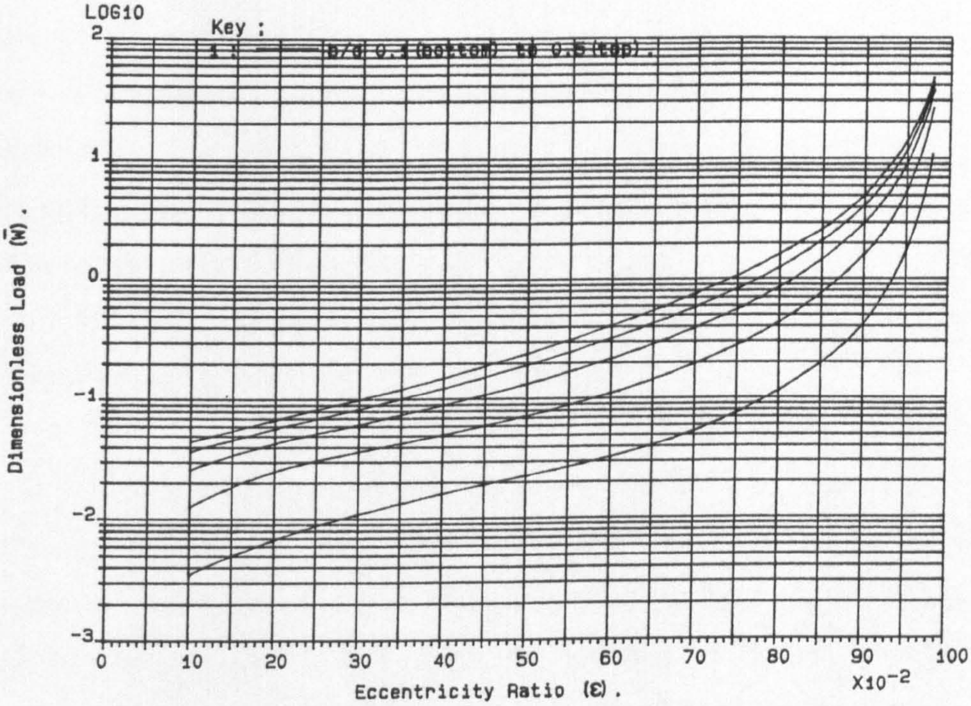

Figure 2.7 Dimensionless Load Variation With Eccentricity Ratio $(\bar{P}_s = 0.05)$.

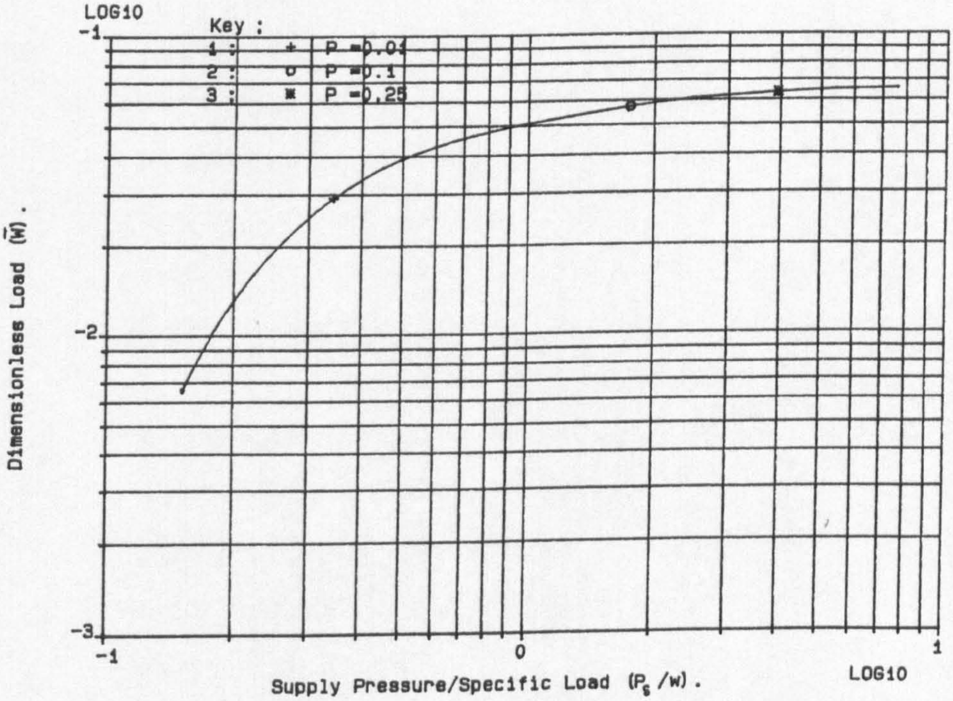

Figure 2.8 Dimensionless Load Versus Supply Pressure/Specific Load. (b/d=0.2 Eccentricity Ratio=0.4).

Eventually, however, the full fluid film case is approached and further increase in supply pressure has little effect on the load capacity as the limiting value is reached. Marked on Figure 2.8 are the dimensionless supply pressure cases considered in Figures 2.6a and 2.6b. For $(\bar{P}_s)$ equal to 0.01 the ratio of supply pressure to specific load is 0.34 and the dimensionless load is 0.029. For a dimensionless supply pressure 25 times greater, (P_s/w) has increased to 3.94 (a factor of 11.59) whilst the dimensionless load has only increased by a factor of 2.17 to 0.063.

A more practical consideration would be the effect of an increase of supply pressure for a given bearing and lubricant dynamic viscosity with a fixed applied load. This may be illustrated by reference to Figure 2.9 where the dimensionless load variation with supply pressure for a range of eccentricity ratio is shown. Broadly speaking two situations are encountered:

(a) At the larger eccentricity ratios the supply pressure has negligible influence upon the dimensionless load capacity. An increase or decrease in supply pressure for a given load will not result in any change in operating eccentricity ratio and shows that the mean hydrodynamic pressure will be large compared with the supply pressure.

(b) At low eccentricity ratios the dimensionless load increases with dimensionless supply pressure. Thus, an increase in supply pressure will cause a reduction in eccentricity ratio for a fixed load capacity (dynamic viscosity being taken as constant). This would be characterized by a movement horizontally to the right for a given dimensionless load $(\bar{W})$ on Figure 2.9.

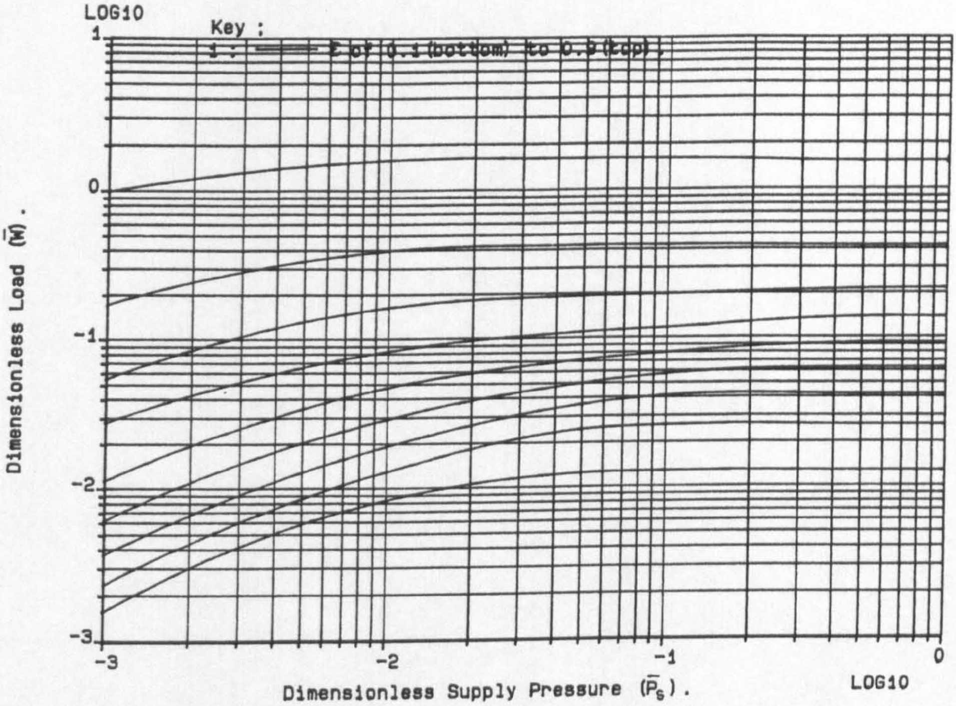

Figure 2.9 Dimensionless Load Variation With Dimensionless Supply Pressure (b/d=0.2).

Eventually, a limiting minimum eccentricity ratio would be reached corresponding to the full film situation. A fall in supply pressure at a low eccentricity ratio will cause an increase in eccentricity ratio.

It is interesting to make a comparison with the design data presented in ESDU Item No. 66023 (1966) for full central circumferential groove journal bearings. This is done in Table 2.3. The dimensionless load and power loss data given in this design document are independent of supply pressure. Load capacity has been taken to be uninfluenced by supply groove arrangement, whilst power loss has been assessed as being the same as for the artificial case of a supply groove at the maximum film thickness position. The data from the design document has been read from graphs and is compared in Table 2.3 with the author's results for dimensionless supply pressure values of 0.001, 0.01, 0.1 and 1.0. Four eccentricity values have been considered, 0.3, 0.5, 0.7 and 0.9 with the width-to-diameter ratio (b/d) of 0.2 as for Figures 2.8 and 2.9. It is evident from Table 2.3 that the author's data encompasses that presented in the ESDU document. At a dimensionless supply pressure of 0.01 the agreement for both dimensionless load and power loss is fairly good. At the extremes of dimensionless supply pressure considerable differences are predicted. This brings clearly into focus the potential inaccuracies inherent in the use of the design item (ESDU Item No. 66023 (1966)).

The minimal effect of supply pressure on load capacity at high eccentricity ratios can also be explained with reference to Figures 2.6a and 2.6b. It can be seen that as the oil supply pressure is reduced the cavitation region first forms in the

Dimensionless Load ($\bar{W}$) and Power Loss ($\bar{H}$) / Eccentricity Ratio (ε)	ESDU 66023 (1966)		Author's $\bar{p}_s = 0.001$		Author's $\bar{p}_s = 0.01$		Author's $\bar{p}_s = 0.1$		Author's $\bar{p}_s = 1.0$	
	$\bar{W}$	$\bar{H}$	$\bar{W}$	$\bar{H}$	$\bar{W}$	$\bar{H}$	$\bar{W}$	$\bar{H}$	$\bar{W}$	$\bar{H}$
0.3	0.023	1.47	0.0037	1.33	0.019	1.42	0.041	1.60	0.042	1.63
0.5	0.059	1.52	0.011	1.30	0.047	1.45	0.079	1.69	0.099	1.80
0.7	0.18	1.77	0.054	1.46	0.16	1.67	0.20	1.98	0.22	2.18
0.9	1.53	2.91	0.99	2.39	1.56	2.79	1.59	3.10	1.59	3.37

Table 2.3 Comparison of the predictions of dimensionless load and power loss from ESDU Item No. 66023 (1964) with the author's results

(Width-to-diameter ratio = 0.2)

divergent part of the bearing clearance space before spreading into the convergent film region through the maximum film thickness position. Therefore, for the cases considered, oil is always present in the region of high hydrodynamic film pressure generation.

The variation of shear power loss with eccentricity ratio is shown in Figures 2.10a and 2.10b for width to diameter ratios of 0.1 to 0.5. The dimensionless supply pressures are 1.0 and 0.01 respectively. Additional tables for dimensionless supply pressures of 0.05, 0.1 and 0.5 are given in Appendix 1.

For a dimensionless supply pressure of 1.0 it was found that the author's data could be represented by a single line to within about ± 2%. For such a high supply pressure a fully flooded situation is approached (if not actually obtained) for all the eccentricity ratios and (b/d) ratios considered. Hence, the dimensionless shear power losses are close to the expression for the 2π film shear case (see Chapter 3) with any differences being due to the circumferential pressure gradients within the oil film and any small cavitation regions still present at higher eccentricity and width to diameter ratios.

Figure 2.10b shows the effect of eccentricity ratio on dimensionless power loss for (b/d) ratios in the range 0.1 to 0.5. It can be seen that for all eccentricity ratios the dimensionless power loss increases with decrease in (b/d) ratio. This is because for any fixed dimensionless supply pressure, as the width to diameter ratio is decreased the proportion of the developed bearing surface area remaining cavitated decreases. It should also be noted that at low eccentricity ratios the shear power loss decreases with increase in eccentricity ratio even though the shear rate across the

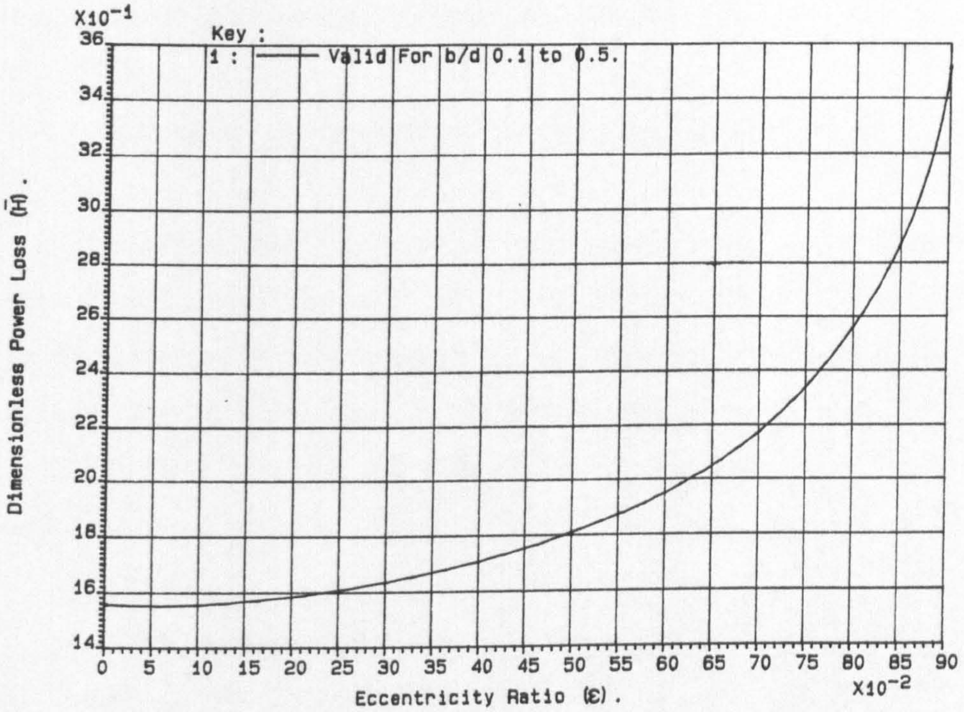

Figure 2.10a Dimensionless Power Loss Variation With Eccentricity Ratio (false origin $\bar{P}_s = 1.0$) .

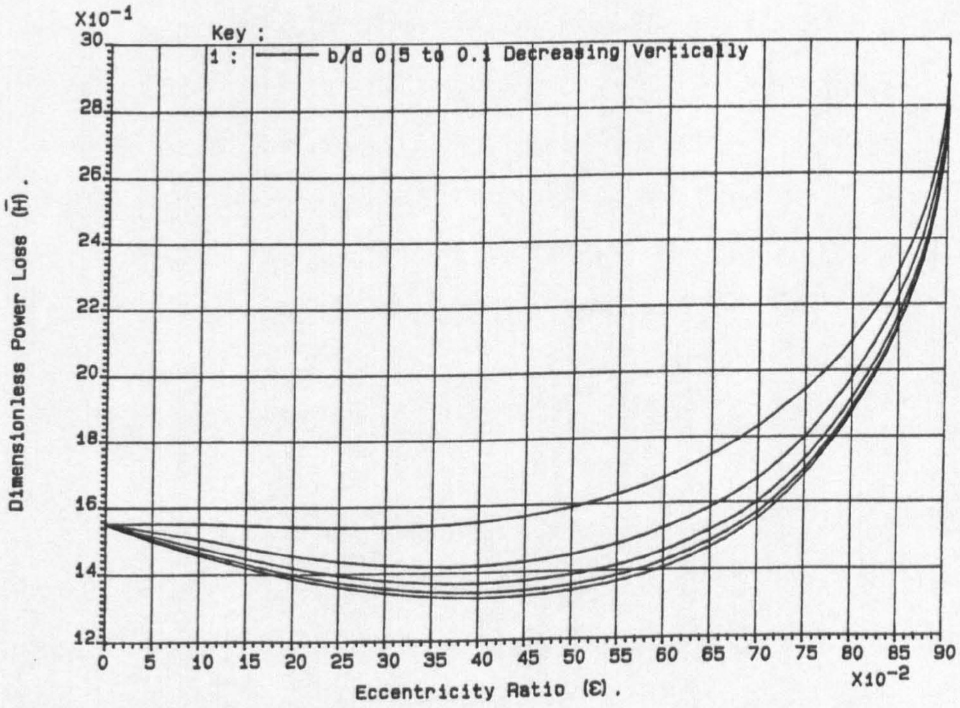

Figure 2.10b Dimensionless Power Loss Variation With Eccentricity Ratio (false origin $\bar{P}_s = 0.01$) .

film is increasing. In this situation the increase in cavitation region size with increase in eccentricity ratio is the dominant factor over the increase in shear rate across the film.

2.5.4 Comparison with Experimental Results of Ayele (1988)

Ayele (1988) collected a significant amount of experimental data relating to the oil flow rate through four different full circumferential groove bearings. The extremes of the bearing (b/d) ratios have been selected for comparison with oil flow predictions from Equation 2.10 and the comparisons can be seen in Figures 2.11 and 2.12.

The agreement for the bearing with width to diameter ratio of 0.406 is better than that of 0.108 for the case of variable eccentricity ratio and supply pressure. From Figure 2.11 the flow prediction is seen to be better at low eccentricities where for zero eccentricity the difference in the experimental and the predicted values is 0.7% for a (b/d) ratio of 0.406, and 4.1% for the (b/d) ratio of 0.108. At higher eccentricity ratios the differences rise to 20%. A similar range of percentage differences can also be seen in Figure 2.12 and a possible reason for these differences is the difficulty Ayele had in setting the eccentricity ratio.

2.6 The Development of an Alternative Solution Technique

The technique described in this section was initially developed for the analysis of dynamically loaded journal bearings. However, the benfits of the method of analysis for steadily loaded cases, particularly in terms of the reduced computer central

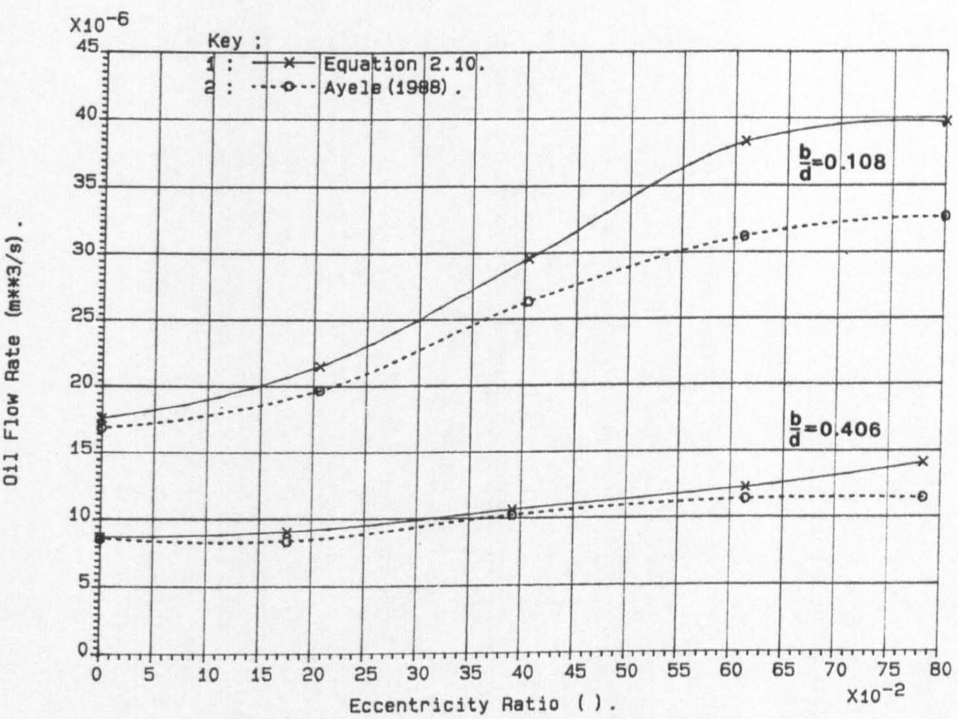

Figure 2.11 Comparison Of Results Of Ayele (1988) With Predictions From Equation 2.10 (P =137.9kN/m**2).

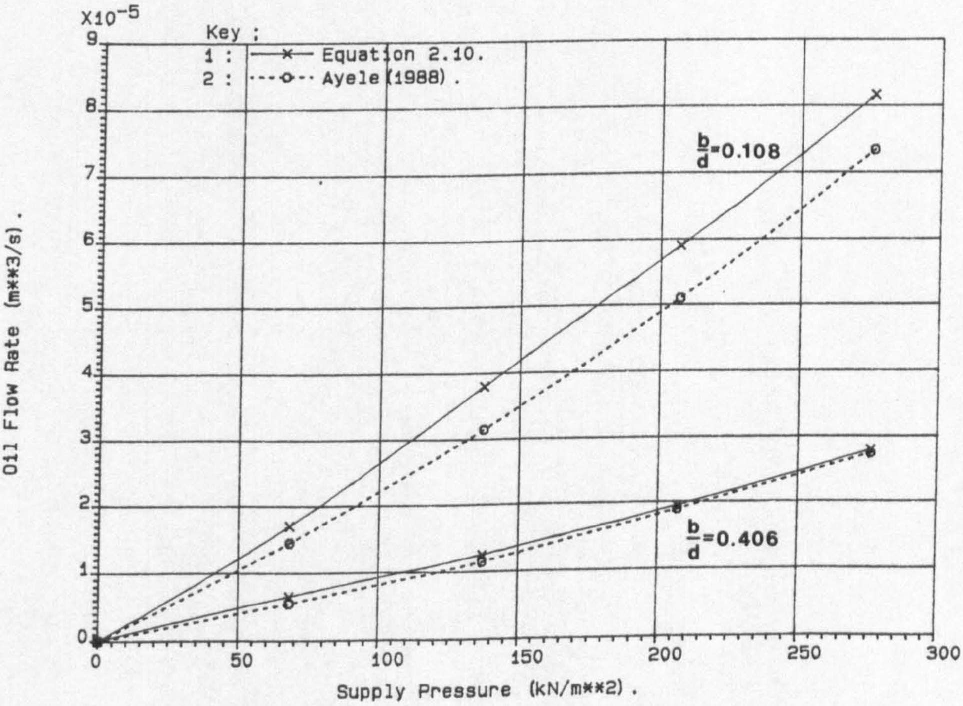

Figure 2.12 Comparison Of Results Of Ayele (1988) With Predictions From Equation 2.10.

processing unit time, meant that a practical real time solution technique was available. The method will be described in relation to the analysis of steadily loaded journal bearings, it's extension to dynamic situations merely requiring the addition of the journal translational velocity term to the equations.

The Jakobsson-Floberg boundary condition was satisfied at film rupture and reformation, but unlike the analysis presented previously (Section 2.3) no problem of nodes oscillating between the cavitation and full film regions at reformation was encountered. The subroutine for the imposition of the boundary condition is presented in Appendix 1. This is for one iterative sweep through the finite difference mesh, and its use in bearing performance prediction procedures will require additional subroutines to be written around the coding given. The important features of the analysis will now be described.

The equation for the continuity of oil flow across the reformation boundary and into the first uncavitated mesh square was written in terms of the component Couette and Poiseuille flow rates. This is the same method used by Jakobsson and Floberg (1959) to derive the continuity reformation boundary condition, and hence, the Couette flow into the mesh square was modified by the variable (θ).

This is essentially the same as the analysis presented in Section 2.3, except the switch functions were set to unity, and the Poiseuille flow components were written in terms of the hydrodynamic film pressure, instead of the lubricant bulk modulus (β) and the dimensionless density (ρ/ρ_c). Hence, the solution of the resulting continuity or film reformation boundary equation was for the hydrodynamic film pressure and (θ) represents the cavitation region streamer width at reformation.

The reformation boundary equation derived was seen to reduce to the Reynolds equation (which is another form of continuity expression for the full film region) at nodes where the upstream mesh square was fully flooded, since for such cases (θ) at the upstream position was unity. Therefore, the determination of the bearing performance characteristics required the solution of the Reynolds equation and the reformation boundary equation for the hydrodynamic film pressures. During the solution finite difference forms of both equations were used to determine the pressure profile within the full film region.

The steps in the solution of the equations were as follows:

1. For each sweep through the finite difference mesh, pressure generation was inhibited at nodes where (θ) was less than 0.995 and negative gauge pressures generated during the solution were set to zero. For mesh squares which had a cavitated upstream node the pressures were determined from the finite difference solution of the reformation boundary equation, hence taking account of the streamer width at the cavitation/full film boundary. For the other full film region nodes the pressures were determined from the Reynolds equation. The bearing was considered to be fully flooded for the first iterative sweep through the finite difference mesh and (θ) was set to unity at every node.

2. New values of (θ) in the cavitation region were determined from oil flow continuity considerations. For the pressure

profile determined in 1. the inlet and outlet Poiseuille and Couette flows were determined for each node in turn, and the value of (θ) at that node was set so that the total gain in the mesh square oil volume was zero. The process was started at the rupture boundary since (θ) at the upstream node was known. Successive downstream nodes were then considered until the reformation boundary was reached.

3. For the new (θ) profile steps 1. and 2. were repeated until the pressure profile at each node converged to within 0.001% on successive iterative sweeps. The bearing load capacity, shear power loss and oil flow rate were then determined.

Jakeman (1984) and Rowe and Chong (1984) have produced solution techniques based on oil flow continuity at the reformation and rupture boundaries, although neither of the previous publications contain any significant amount of generated data. The present solution is similar to that of Rowe and Chong (1984). Table 2.4 gives a comparison of the dimensionless load, power loss and oil flow rate for the author's performance predictions using the cavitation algorithm of Elrod (1981) and the present real time solution, with data from a private communication with Mr. F.A. Martin (1989). It can be seen that the agreement between all the quantities given is good, particularly for the bearing load capacity and shear power losses where the differences are less than 2%. The agreement for the oil flow rate can be seen to be somewhat greater for both of the author's solutions compared with the data of Mr. F.A. Martin. This is particularly true at the higher eccentricity ratios and could be due to the mesh sizes used.

Dimensionless Load ($\bar{W}$) Power Loss ($\bar{H}$) and Oil Flow Rate ($\bar{Q}$) / Eccentricity Ratio (ε)	F A Martin (Private Communication)			Present Real Time Solutions			Present Work Using Elrod's Algorithm		
	$\bar{W}$	$\bar{H}$	$\bar{Q}$	$\bar{W}$	$\bar{H}$	$\bar{Q}$	$\bar{W}$	$\bar{H}$	$\bar{Q}$
0.3	0.041	1.62	0.185	0.041	1.60	0.183	0.041	1.60	0.179
0.5	0.080	1.69	0.215	0.079	1.69	0.230	0.079	1.69	0.224
0.7	0.20	1.94	0.260	0.193	1.97	0.209	0.20	1.98	0.281
0.9	-	-	-	1.59	3.11	0.36	1.59	3.10	3.370

Table 2.4 Comparison of the Predictions of Dimensionless Load, Power Loss and Oil Flow Rate From Several Sources

(Width-to-diameter-ratio = 0.2 Dimensionless supply pressure = 0.1)

In Sections 2.4.1 and 2.4.2 the reasons for the choice of mesh size for the analysis using the algorithm of Elrod (1981) were discussed. However, in the present solution no limitations on the mesh sizes were apparent and for the case considered in Table 2.4 reductions in the dimensionless flow rates of between 1 and 3% were obtained for a mesh size of 25 x 100. It is likely that if finer meshes could have been used for the analysis incorporating Elrod's algorithm, then similar reductions in the flow rate would have been obtained. (It is not known what mesh size was used for the data supplied by Mr. F.A. Martin). In view of the comments made above the agreement between the two solutions of the author is encouraging. In addition, data for other width-to-diameter ratios and dimensionles supply pressures showed close agreement with the oil flow rate curve fit presented in Section 2.5.4. Indeed, the flow data used for the comparison in Table 2.4 showed greater discrepancies than the majority of the other data generated. However, this was used for comparative purposes since only two sets of data were obtained from Mr. F.A. Martin. The other set was for a (b/d) ratio of 0.2 and a dimensionless supply pressure of 1.0. The agreement in flow rate for these parameters was excellent, both in terms of the actual raw data and the curve fit.

The present solution technique reduced the computer run times for bearing performance data considerably when compared with the author's solution using the algorithm of Elrod (1981). Table 2.5 shows typical computer central processing unit times on the Amdahl 570 mainframe computer for several finite difference mesh sizes.

The values for an 11 x 51 mesh size obtained using Elrod's cavitation algorithm were at least an order of magnitude greater than those given below and in some cases this could be as high as a factor of 100.

Mesh Size	Computer Run Time (seconds)
11 x 51	0.5
17 x 70	2
19 x 90	4
25 x 100	7

Table 2.5 Typical Computer Run Times Per Data Point

2.7 Conclusions

The cavitation algorithm suggested by Elrod (1981) has been applied to the case of a journal bearing with a full circumferential groove. Data for a wide range of input variables has been produced and compared with the published results of Lundholm (1969), Ruddy (1979), ESDU Item No. 66023 (1966) and Ayele (1988). Additional tabular output can be found in Appendix 1.

The main conclusions and points to be drawn from the analysis are summarized below.

1. Comparisons of the results from the present analysis with those in the published literature show excellent agreement for load capacity, shear power loss and oil flow rate.
2. Excellent agreement between the pressure flow equation given in ESDU Item No. 66023 (1966) and the data for flow from the present analysis was found. However, based on the generated data, the constant of proportionality of the

pressure flow equation was refitted. The new value was 0.0315 giving a difference of 4% when compared with the value given in the ESDU design document.

3. The oil flow rate was shown to be independent of the shaft rotational speed.

4. Increase in dimensionless supply pressure decreased the cavitation region size. However, the cavitation region size does not significantly affect the dimensionless oil flow rate for a fixed eccentricity ratio.

5. At high eccentricity ratios the supply pressure had little effect on the bearing load capacity for the range of input parameters used.

6. The extensive data for load capacity and shear power loss variation with eccentricity ratio and supply pressure, coupled with the verification of the accuracy of the pressure flow equation, means that more reliable thermal iterations to determine an effective oil temperature for steadily loaded full central circumferential groove bearings are now possible. However, there is a need to verify these by comparison with experimental data.

7. Comparisons of predictions with the experimental results of Ayele (1988) were acceptable, differences could well be due to the experimental difficulty faced in setting the eccentricity ratio.

8. The time required for convergence of a single solution using Elrod's algorithm makes the present analysis unsuitable for application to dynamic load cases. Times of 80 seconds were not uncommon, and for dynamic loaded cases which require many such solutions, the required time will be prohibitive.

CHAPTER 3

CHAPTER 3

THE MOBILITY METHOD

3.1 Introduction

Many of the techniques currently used for performance predictions of dynamically loaded journal bearings make use of the mobility method, the main thrust being the determination of the shaft centre orbit during an operating cycle. With this established the minimum lubricant film thickness during an operating cycle may be determined and the magnitude of this has been an important design criterion. The technique leads to a simple and robust approach to the orbit determination, since the governing Reynolds equation has been solved prior to the analysis. However, it must be recognised that the resulting data can only be used effectively in a comparative sense as opposed to being considered precise. That is, designers would hope that the analytical technique would give correct trends in relation to film thickness variations as input parameters are varied, but would accept that absolute magnitudes can be called into question.

It is appropriate to note some of the assumptions of the mobility method:

(1) Circumferential symmetry with no consideration of oil supply features
(2) No misalignment between journal and bearing
(3) Circular bearing and shaft with no account of elastic or thermal distortions
(4) Isothermal analysis and Newtonian lubricant behaviour

Bearing these assumptions in mind it is clearly evident why the method is applied in a comparative manner to judge the likelihood of problems on new engines.

The most widely used form of mobility analysis has adopted the short bearing approximation in which circumferential pressure gradients are considered negligible with respect to axial pressure gradients. Booker (1965) provided simple curve fits to mobility data for the short bearing case, and these together with the finite bearing mobility curve fits of Goenka (1984) will be used extensively in subsequent chapters. For this reason, and since the mobility method has such a wide spread industrial use, the remainder of this chapter will be set aside to describe the process of mobility data generation and its subsequent use in journal orbit prediction. Equations for the oil flow rate and power loss prediction for an engine cycle will then be introduced and the possibility of a broad thermal analysis will be discussed.

3.2 Mobility Data Generation - Theory

In this section a brief description of the method of mobility data generation for the case of a finite bearing with any oil feed features and geometry is given. The special case of a perfectly circular, unfeatured short bearing (Booker (1965)) is also discussed. The analyses were subsequently used to generate mobility data for short and finite bearing cases, and comparisons with the curve fits of Booker (1965) and Goenka (1984) are given. This is quite possibly the first time Booker's and Goenka's curve fits have been checked.

3.2.1 Mobility Data Generation for General Case

Figure 3.1 shows the coordinate system for the present analysis. The directions of the various mobility vectors are clearly shown.

The Reynolds equation for the case of a journal bearing subjected to a rotating load of variable magnitude is given by,

$$\frac{\partial}{\partial\theta}\left(\frac{h^3}{12\eta}\frac{\partial P}{\partial\theta}\right) + r^2\frac{\partial}{\partial y}\left(\frac{h^3}{12\eta}\frac{\partial P}{\partial y}\right) = cr^2\left(\dot{\varepsilon}\cos\theta + \varepsilon\phi\sin\theta\right) \quad (3.1)$$

or in dimensionless form,

$$\frac{\partial}{\partial\theta}\left(\frac{\bar{h}^3}{12}\frac{\partial\bar{P}}{\partial\theta}\right) + \left(\frac{d}{2b}\right)^2\frac{\partial}{\partial\bar{y}}\left(\frac{\bar{h}^3}{12}\frac{\partial\bar{P}}{\partial\bar{y}}\right) = \varepsilon\left(\frac{\dot{\varepsilon}}{\varepsilon\dot{\phi}}\cos\theta + \sin\theta\right) \quad (3.2)$$

where $\dot{\phi} = \dot{\psi} - \bar{\omega}$, $y = b\bar{y}$, $h = c\bar{h}$, $x = r\theta$ and $P = \dfrac{\eta\dot{\phi}r^2}{c^2}\bar{P}$

Therefore, for any width-to-diameter ratio (b/d), eccentricity ratio (ε) and ratio of mobility vectors (M^{ε}/M^{ϕ}) or ($\dot{\varepsilon}/\varepsilon\dot{\phi}$), Equation 3.2 can be solved to give the dimensionless pressure profile ($\bar{P}$). Numerical integration of the film pressures to give loads along and perpendicular to the bearing/journal line of centres enables the mobilities (M^{ε}), (M^{ϕ}) and (M) to be determined. The dimensionless loads are given by,

$$\bar{W}_A = \frac{W_A\,c^2}{\eta b r^3\phi} = -\int_0^{2\pi}\int_0^1 \bar{P}r\cos\theta\,d\theta\,d\bar{y} \quad (3.3a)$$

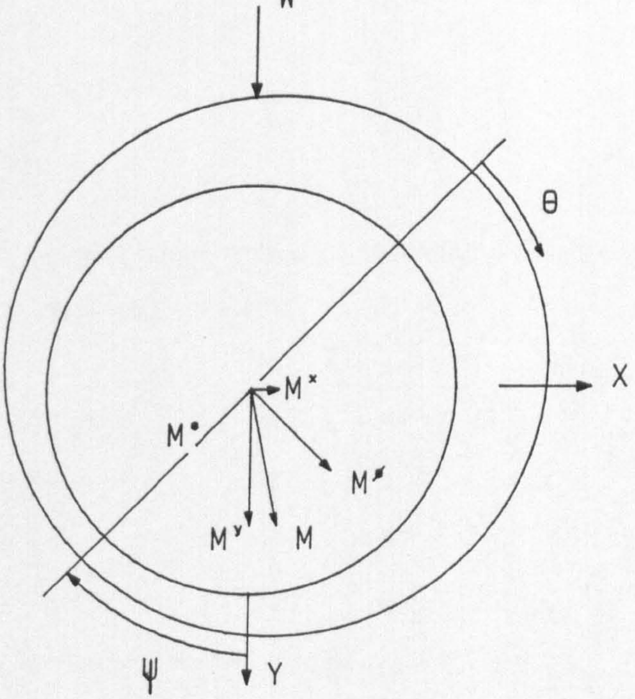

Figure 3.1 Co-ordinate System Showing Relationship Between Mobility Vectors.

$$\bar{W}_N = \frac{W_N\, c^2}{\eta b r^3 \dot{\phi}} = \int_0^{2\pi} \int_0^{1} \bar{P} r \sin\theta \, d\theta \, d\bar{y} \tag{3.3b}$$

with the total load given by vector summation and the attitude angle by:-

$$\tan\psi = \frac{\bar{W}_N}{\bar{W}_A} \tag{3.4}$$

The magnitude of the mobility vector (by definition - dimensionless ratio of velocity to load) is given by,

$$M = \frac{\left[\dot{\varepsilon}^2 + (\varepsilon\dot{\phi})^2\right]^{\frac{1}{2}}}{\dfrac{W \left(\dfrac{c}{r}\right)^2}{\eta\, r\, b}} \tag{3.5}$$

and dividing the numerator and denomenator by $(\varepsilon\dot{\phi})$ gives,

$$M = \frac{\left[\left(\dfrac{\dot{\varepsilon}}{\varepsilon\dot{\phi}}\right)^2 + 1\right]^{\frac{1}{2}} \varepsilon}{\bar{W}} \tag{3.6}$$

The values of (M^{ε}) and (M^{ϕ}) can now be found from

$$M^{\phi} = \frac{-M}{\left[\left(\dfrac{\dot{\varepsilon}}{\varepsilon\dot{\phi}}\right)^2 + 1\right]^{\frac{1}{2}}}$$

$$M^{\varepsilon} = \frac{-M}{\left[\left(\dfrac{\dot{\varepsilon}}{\varepsilon\dot{\phi}}\right)^2 + 1\right]^{\frac{1}{2}}} \left|\frac{\dot{\varepsilon}}{\varepsilon\dot{\phi}}\right| \left(\frac{\varepsilon\dot{\phi}}{\varepsilon}\right) \tag{3.7}$$

This general method is applicable to any oil groove configuration, however, for the case of bearings which lack circumferential symmetry, several sets of mobility data need to be generated to ensure the correct angular displacement between the oil groove or hole, load line and bearing/journal line of centres.

The method used by Goenka (1984) to generate mobility data for finite width journal bearings is believed to be similar to that described above, however, he does not provide any in depth description of his method. Goenka generated data for finite width journal bearings with zero gauge pressure at both bearing edges and provided extensive curve fits to the mobility data.

3.2.2 Mobility Data Generation - Short Bearing Special Case

The Reynolds equation for the case of a journal subjected to a rotating load of variable magnitude is given by Equation 3.1, which for a short journal bearing may be reduced to:-

$$\frac{\partial}{\partial y}\left(\frac{h^3}{12\eta}\frac{\partial P}{\partial y}\right) = c\,(\dot{\varepsilon}\cos\theta + \varepsilon\dot{\phi}\sin\theta) \tag{3.8}$$

Integration to determine the pressure distribution,

$$P = -6\eta\left(\frac{r}{c}\right)^2\left(\frac{b}{d}\right)^2\left(1 - \left(\frac{2y}{b}\right)^2\right)(\dot{\varepsilon}\cos\theta + \varepsilon\dot{\phi}\sin\theta)(1+\varepsilon\cos\theta)^{-3} \tag{3.9}$$

and then for the hydrodynamic forces acting along and perpendicular to the line of centres of the shaft and bearing gives:-

$$W_A = -\int_0^b \int_{\theta_1}^{\theta_2} Pr\cos\theta\, d\theta\, dy \tag{3.10a}$$

$$W_N = \int_0^b \int_{\theta_1}^{\theta_2} Pr \sin\theta \, d\theta \, dy \qquad (3.10b)$$

Solution of the resulting simultaneous equations yields:-

$$\dot{\varepsilon} = \frac{W\left(\frac{c}{r}\right)^2}{\eta bd} \left[\frac{J_3^{20} \cos\psi + J_3^{11} \sin\psi}{2\left(J_3^{02} J_3^{20} - J_3^{11} J_3^{11}\right)\left(b/d\right)^2}\right] = \frac{W\left(\frac{c}{r}\right)^2}{\eta bd} M^{\varepsilon}$$

(3.11)

$$\varepsilon = \frac{W\left(\frac{c}{r}\right)^2}{\eta bd} \left[\frac{J_3^{02} \cos\psi + J_3^{11} \sin\psi}{2\left(J_3^{02} J_3^{20} - J_3^{11} J_3^{11}\right)\left(b/d\right)^2}\right] = \frac{W\left(\frac{c}{r}\right)^2}{\eta bd} M^{\phi}$$

where $$J_n^{lm} = \int_{\theta_1}^{\theta_2} \frac{\sin^l\theta \cos^m\theta}{(1 + \varepsilon\cos\theta)^n} \, d\theta$$

Equations 3.11 may be integrated from (θ_1) to $(\theta_2 = \theta_1 + \pi)$ using the Sommerfeld substitution:-

$$1 + \varepsilon\cos\theta = \frac{1 - \varepsilon^2}{1 - \varepsilon\cos\gamma} \qquad (3.12)$$

This is termed the PI film case, since the region of positive oil film generation is considered to lie over 180° (or π radians) of the journal bearing surface.

The mobilities are given by:-

$$M^{\varepsilon} = \frac{J_3^{20} \cos\psi + J_3^{11} \sin\psi}{2(J_3^{02} J_3^{20} - J_3^{11} J_3^{11}) \, (b/d)^2}$$

(3.13)

$$M^{\phi} = \frac{J_3^{02} \cos\psi + J_3^{11} \sin\psi}{2(J_3^{02} J_3^{20} - J_3^{11} J_3^{11}) \, (b/d)^2}$$

and the integration to determine the mobilities M^ε and M^ϕ require an initial guess as to the value of (θ_1). This is then checked with the value obtained from;

$$\tan\theta = -\left(\frac{M^\varepsilon}{M^\phi}\right) \tag{3.14}$$

and hence a criterion for the positioning of the positive hydrodynamic film pressure region is obtained. Equation 3.14 may be obtained by setting Equation 3.9 to zero. This, in addition to setting $\left(\frac{\partial p}{\partial \theta}\right) \geq 0$ at $(\theta = \theta_1)$ enabled the correct positioning of the full film region.

Booker (1965) curve fitted mobility data generated in the above way for directions (x) and (y) shown in Figure 3.1. The curve fits reported were:-

$$M^x = \frac{-4\varepsilon \sin\psi \, (1-\varepsilon\cos\psi)^{3/2}}{\pi^2 \, (b/d)^2}$$

$$M^y = \frac{(1 - \varepsilon \cos\psi)^{5/2}}{\pi \, (b/d)^2} \tag{3.15}$$

3.3 Comparison of Exact Solutions for Short and Finite Journal Bearing Mobility Data with Curve Fits of Booker (1965) and Goenka (1982)

The methods of mobility data generation described in Section 3.2 has been used to generate mobility data for the short and finite width journal bearing cases. The data was then used to assess the curve fits of Booker and Goenka.

3.3.1 Comparison of Present Data with Curve Fits of Booker (1965)

Table 3.1 gives a comparison of the mobility data generated in the present research work (solution of Equations 3.13) and that from the curve fits given by Equations 3.15. It can be seen that the agreement between both sets of data is good, particularly at low eccentricity ratios where the differences are less than 1%. However, at higher eccentricity ratios the differences may be as high as 6 or 7%.

The agreement in the film reformation angles (θ_1) is generally within about 2°, with a large proportion of the data (89%) where the values agree to within 1°.

3.3.2 Comparison of Present Data with Curve Fits of Goenka (1984)

While most of the design techniques which make use of the mobility method use the short bearing mobility expressions, the mobility data for the finite bearing case is seen as being important. This is principally due to the differences in minimum oil film thicknesses predicted by each set of curve fits, and secondly because of the effect the different orbits will have on the cyclic oil flow and in particular the cyclic shear power loss. This will be discussed in Chapter 5.

Mobility data for the case of an unfeatured finite width bearing with zero pressure at the bearing edges has been generated. This corresponds to the case which was curve fitted by Goenka (1984) and may be thought of as either a full circumferential groove bearing with zero supply pressure, or a oil hole or axial groove with zero supply pressure, positioned at the film reformation

		Solution of Equations 3.13		Curve Fits - Booker (1965)	
Attitude Angle (ψ)	Eccentricity Ratio (ε)	Mobility ($\bar{M}$)	Film Reformation Angle (θ_1)	Mobility ($\bar{M}$)	Film Reformation Angle (θ_1)
10°	0.1	0.244	78.5	0.245	78.6
	0.2	0.182	76.7	0.184	76.8
	0.3	0.131	74.4	0.133	74.6
	0.4	0.090	71.3	0.0920	71.7
	0.5	0.058	67.1	0.0598	67.7
	0.6	0.035	60.9	0.0358	62.0
	0.7	0.0189	51.8	0.0191	53.5
	0.8	0.0087	37.9	0.0086	40.1
	0.9	0.0029	18.0	0.0028	19.7
30°	0.1	0.253	55.9	0.254	56.0
	0.2	0.198	51.1	0.200	51.2
	0.3	0.153	45.2	0.155	45.5
	0.4	0.117	38.1	0.118	38.7
	0.5	0.0885	29.9	0.0884	30.6
	0.6	0.0659	20.6	0.0650	21.5
	0.7	0.0481	10.6	0.0468	11.4
	0.8	0.0338	0.5	0.0322	1.1
	0.9	0.0218	-9.1	0.0202	-8.9
90°	0.1	0.321	-7.3	0.321	-7.2
	0.2	0.330	-14.3	0.329	-14.2
	0.3	0.344	-20.8	0.341	-20.9
	0.4	0.363	-26.8	0.357	-26.9
	0.5	0.386	-32.2	0.377	-32.4
	0.6	0.413	-36.9	0.401	-37.3
	0.7	0.443	-41.1	0.426	-41.7
	0.8	0.477	-44.7	0.454	-45.5
	0.9	0.513	-48.0	0.484	-48.8
160°	0.1	0.400	-72.3	0.399	-72.2
	0.2	0.495	-74.2	0.491	-74.1
	0.3	0.603	-75.7	0.595	-75.8
	0.4	0.725	-77.1	0.712	-77.2
	0.5	0.861	-78.2	0.843	-78.4
	0.6	1.01	-79.2	0.987	-79.4
	0.7	1.18	-80.0	1.15	-80.4
	0.8	1.36	-80.8	1.32	-81.2
	0.9	1.56	-81.4	1.51	-81.9

Table 3.1 Comparison of Mobility Data from Curve Fits of Booker (1965) with Solution of the Mobility Equations (3.13)

position as predicted by Reynolds equation.

Table 3.2 gives a comparison of percentage differences (for attitude angles less than 90°) between Goenka's curve fits and data generated from the present analysis. For all cases Reynolds' boundary condition was achieved by setting all negative gauge pressures generated during the finite difference solution of Reynolds' equation to zero. This gave a rapid solution, a typical c.p.u. time per solution point being about 0.4 second.

The close agreement of the data generated in the present analysis with that of Goenka's curve fits is apparent from Table 3.2 This indicates a good curve fit. All the percentage differences given in Table 3.2 are positive and based on the authors values. Hence, Goenka's data gave in every case a larger mobility than that calculated here. Goenka found that the curve fits in relation to his data were biased to giving slightly smaller values of mobility. He also reported that his curve fits were within 2% of the correct value for over 76% of the data points and within 5% for over 99.5% of the points. In the present analysis Goenka's curve fits gave agreement to within 2% for over 70% of points and to within 5% for over 95% of the cases tested.

The curve fit expressions are valid in the ranges,

$$\begin{aligned} &\psi \leq 90^\circ \\ &0.25 \leq b/d \leq 1.0 \end{aligned} \qquad (3.16)$$

and it was suggested by Goenka that the accuracy may be poor outside

	MOBILITY NUMBER	
Width to diameter ratio	Mean percentage difference	Maximum difference
0.281 (6VEB)		
All eccentricities	2.28	7.34
$\varepsilon = 0.99$	4.03	7.34
$\varepsilon = 0.9$	2.14	5.24
$\varepsilon = 0.5$	1.15	3.87
0.2 (≃ Hydra)		
All eccentricities	4.2	13.0
$\varepsilon = 0.99$	5.67	13.0
$\varepsilon = 0.9$	4.18	7.36
$\varepsilon = 0.5$	1.10	1.82
0.15		
All eccentricities	4.90	12
$\varepsilon = 0.99$	7.06	12
$\varepsilon = 0.9$	4.75	7.55
$\varepsilon = 0.5$	1.08	1.5
All data generated	3.61	13

Table 3.2 Percentage differences between present finite bearing mobility data and that of the curve fits of Goenka (1984)

these ranges. It is important to assess the suitability of Goenka's curve fits to (b/d) ratios outside this range as the performance prediction technique developed in the present work is to be used to analyse the front main bearing of the Ricardo Hydra. This engine was used in the experimental part of the present work (Chapters 6 and 7) and has a main bearing width to diameter ratio of about 0.2.

A comparison is given in Table 3.2 for width to diameter ratios of 0.2 and 0.15. For a (b/d) ratio of 0.2 the mean difference of all the data is 4.2%, which rises to 4.9% for a width to diameter ratio of 0.15.

It can be seen from Table 3.2 that the curve fits represent the generated data better at lower eccentricity ratios than at higher ones. At an eccentricity ratio of 0.5 the mean differences are marginally over 1% for the three (b/d) ratio considered, at higher eccentricities the differences range from 4.03 to 7.06%. For all data points the mean difference was 3.61%.

3.3.3 The Effect of Groove Pressure on Mobility Data and Orbit Prediction

For the Ruston and Hornsby 6VEB-X Mk111 (b/d = 0.281), finite width mobility data for a full central circumferential groove bearing, at a range of dimensionless supply pressures, has been generated and used to assess the effect of the oil supply pressure on the journal centre orbit. This is shown in Figure 3.2.

Since the dimensionless oil supply pressure ($\bar{P}_s$) (given by $\bar{P}_s = P_s \left(\frac{c}{r}\right)^2 / \eta \dot{\phi}$) is dependent on the value of (ϕ), which is

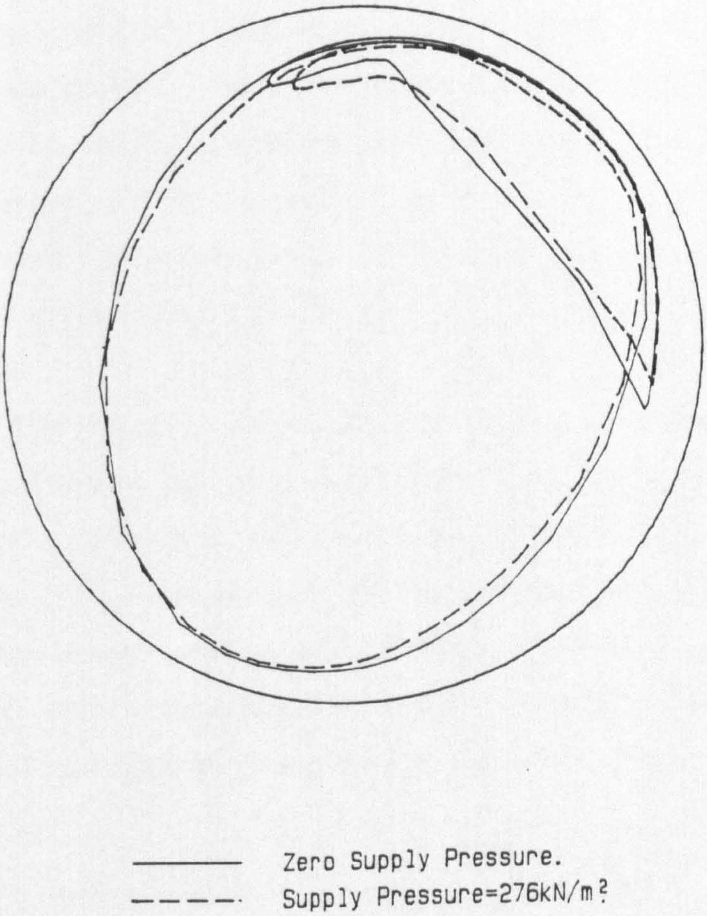

Figure 3.2 The Influence Of Oil Supply Pressure On The Journal Centre Orbit.

determined from the value of the angular mobility (M^{ϕ}), an initial estimate of ($\bar{P}_s$) was made at which to determine the mobilities. These were determined by interpolation from mobility data which had been generated for dimensionless supply pressures of 1.0, 0.5 and 0.0 (Goenka curve fit case). The values of (ϕ) and ($\bar{P}_s$) were then recalculated and a check on the value of ($\bar{P}_s$) used for the interpolation, and that determined using the new value of (ϕ), gave a criterion for the mobility determination at the correct dimensionless oil supply pressure.

The effect of oil supply pressure on power loss, oil flow rate and effective oil temperature due to the effect on the journal centre orbit is shown in Table 3.3. (A thermal balance to determine the effective oil temperature and equilibrium operating conditions of the Ruston and Hornsby 6VEB-X Mk111 big end bearing has been performed. The associated analysis will be discussed in Chapter 5. It will also be applied extensively in subsequent chapters).

	Difference in Computed Value		
Inlet Oil Temperature (T_{in}) (°C)	Effective Oil Temperature (T_e) (°C)	Oil Flow Rate (Q_p) (%)	Power Loss (H) (%)
60	0.7	4.2	7.3
80	0.4	3.4	6.9
100	0.3	1.9	5.7

Table 3.3 The effect of oil supply pressure on the equilibrium operating conditions for the Ruston and Hornsby 6VEB-X Mk111 big-end bearing

The minimal effect on the effective oil temperature is reflected in the small differences associated with the power loss, and in particular the oil flow rate calculated from the pressure flow equation (Equation 2.10). All the differences in Table 3.3 are positive indicating that the effect of oil supply pressure on journal centre orbit reduced all the calculated quantities.

The effect of supply pressure on mobility data is shown graphically in Figure 3.3. Values of ($\bar{P}_s$) for the orbit were generally in the range -1 to 1, with a large number of orbit positions having values close to 0.3. For this reason a comparison of mobility data at a dimensionless oil supply pressure of 0.0 (zero) and 0.3 is given. It can be seen that at low attitude angles and high eccentricity ratios the lines of constant mobility are very close. This is to be expected since the hydrodynamically generated oil film pressures are orders of magnitude higher than the supply pressure. However, at high attitude angles (> 40°) the effect of the supply pressure becomes evident and the lines of constant mobility are seen to diverge as the clearance circle is approached.

In addition, the lines of constant mobility are not drawn through the central squeeze path, since ($\dot{\phi}$) is zero, and the dimensionless supply pressure is infinite for any bearing geometry and oil supply conditions. This is because:-

$$\bar{P}_s = \frac{P_s \left(\frac{c}{r}\right)^2}{\eta \dot{\phi}} \qquad (3.17)$$

Hence, this could lead to difficulties in taking the squeeze step if the journal centre were to lie on the load line. To

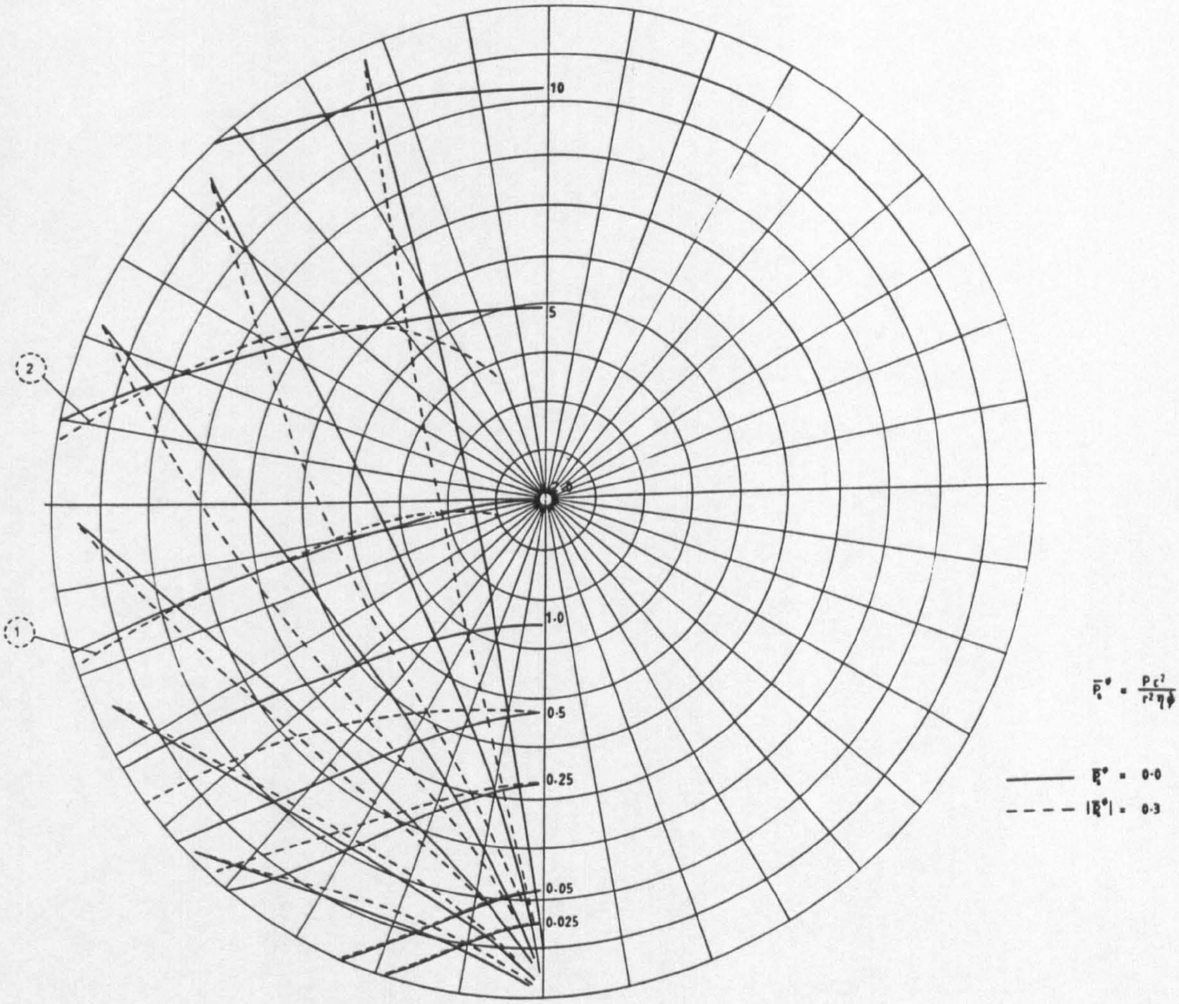

Figure 3.3 Finite Bearing Mobility Map Showing The Influence Of The Oil Supply Pressure

circumnavigate the problem mobility data could be generated at a high dimensionless supply pressure at an attitude angle of 0.1° so approaching the full flooded bearing situation. It is thought that dimensionless pressures higher than this would not affect the mobility since the pressures acting upon the journal due to supply pressure would balance and equal zero. This point was discussed in Chapter 2 in relation to steadily loaded journal bearings. (see Section 2.5.3, Figure 2.8). If on any occasion the attitude angle was less than 0.1° than it would be assumed that the attitude angle was 0.1° and the mobility data for the high dimensionless supply pressure would be used in determining the squeeze step. Alternatively, mobility data could be generated for a different non-dimensionalization of pressure which is based on ($\dot{\varepsilon}$). That is,

$$\bar{P}_s = \frac{P_s \left(\frac{c}{r}\right)^2}{\eta\dot{\varepsilon}} \tag{3.18}$$

Since ($\dot{\varepsilon}$) is defined on the central squeeze path (and is not zero), mobility data can be determined at all angular positions within the clearance circle. Both normalizations of pressure give the same value of mobility at all points within the clearance circle, except on the equilibrium locus where ($\dot{\varepsilon}$) is zero, and the central squeeze path where ($\dot{\phi}$) is zero.

For the case considered in this section, no problem of mobility determination was encountered since the shaft centre never lay close enough to the central squeeze path to cause problems.

3.4 The Determination of the Bearing Instantaneous and Cyclic Oil Flow Rates

It has already been pointed out that a major thrust of the mobility method is the determination of the journal orbit and minimum oil film thickness prediction. However, with these established it is possible to estimate the instantaneous oil flow rate from the bearing and then numerically integrate to estimate the overall cyclic oil flow rate.

The engineering approximation of dividing the oil flow rate into two components (pressure and hydrodynamic flow) and summing these to obtain the total oil flow rate was introduced in Chapter 1. However, it was shown by Jones (1982) that for various groove arrangements the pressure induced flow rate alone gave better agreement with more rigorous solutions, and indeed with experimental data. It was also reported that the sum of the pressure and hydrodynamically induced flows substantially over estimated the more rigorously determined side leakage.

The purpose of this section is to introduce the various simple methods for oil flow rate determination before extending the analysis to address more complex considerations (Chapter 4). This will also provide a bench mark for the more rigorous prediction procedures.

3.4.1 Pressure and Hydrodynamic Flow Rate Determination

The instantaneous pressure and hydrodynamic flow rates from a full circumferential groove bearing may be determined from,

$$Q_P = \frac{0.0327\ P_s\ c_d^{\ 3}}{\eta} \left(\frac{d}{b}\right) (1.5\ \varepsilon^2 + 1) \tag{3.19}$$

and $$Q_H = \frac{W\ M\ (c_d/d)^2\ c_d}{2\eta} \tag{3.20}$$

The author has spent time developing a technique to determine the hydrodynamic flow for a short journal bearing. However, it was later found that the path of analysis had been investigated by other authors and that the resulting equation (Equation 3.20) had been published by Booker (1979). A brief description of the analysis is given here since it is not presented elsewhere (to the best of the author's knowledge), and it is important in relation to the development of two additional flow rate predictive techniques.

The equation for the flow rate from both sides of a bearing is given by:-

$$Q_H = -2 \int_{\theta_1}^{\theta_2} \left. \frac{h^3}{12\eta} \frac{\partial P}{\partial y} \right|_{y\ =\ b/2} r\ d\theta \tag{3.21}$$

Substitution of the pressure gradient at the bearing edge from Equation 3.9 and considering the flow from the bearing sides in the region of positive hydrodynamic pressure generation (π film case) gives,

$$Q_H = - \int_{\theta_1}^{\theta_{1+\pi}} rbc\ (\dot{\varepsilon}\ \cos\theta + \varepsilon\dot{\phi}\ \sin\theta) d\theta \tag{3.22}$$

or in dimensionless form:-

$$\bar{Q}_H = \frac{Q_H}{rbc\ \phi} = -\int_{\theta_1}^{\theta_1+\pi} \varepsilon \left(\frac{\dot{\varepsilon}}{\varepsilon\phi}\cos\theta + \sin\theta\right) d\theta \tag{3.23}$$

Since,

$$\phi = \frac{W\left(\frac{c}{r}\right)^2}{\eta bD}\ \frac{M^\phi}{\varepsilon} \tag{3.24}$$

Equation 3.23 can be shown to reduce to:-

$$Q_H = \frac{W\ M\ (c_d/d)^2\ c_d}{2\eta}$$

This is the equation for the hydrodynamic oil flow rate from both sides of a short journal bearing. During the author's analysis the flow rate predictive technique was based on knowing the inlet film angle (θ_1). Appendix 2 shows lines of contact (θ_1) for journal centre positions in the clearance circle.

3.4.2 Selective Summation - A New Method of Oil Flow Rate Determination

In this method of oil flow rate determination the instantaneous hydrodynamic and pressure induced flow rates at each shaft centre position during the engine cycle are calculated from Equations 3.19 and 3.20. Then the larger of the two instantaneous flows at each journal centre position is used in the numerical integration to give the total cycle flow.

Essentially the pressure flow is taken as a base line and the hydrodynamic flow peaks are superimposed. Hence, a solution for the total flow rate between that of the pressure flow and the sum of the pressure and hydrodynamic flow is given for the cycle average value. Results for this analysis are presented in Chapter 5 where an in depth investigation of the Ruston and Hornsby 6VEB-X Mk 111 is presented.

A concern of the selective summation technique presented is that the hydrodynamic flow rate component (due to shaft and bearing rotational velocities) is essentially taken into account twice. In Chapter 2 it was shown that for a steadily loaded full central circumferential groove bearing the total oil flow rate considering coupled surface rotational velocities and oil supply pressure, with a consideration of oil flow continuity throughout the lubrication region could be given to within a few percent by the equation usually considered to represent the pressure flow rate alone. The selective summation in its present form also considers the rotational velocities of the journal and bearing when determining the hydrodynamic flow. It is therefore proposed that a more realistic and accurate determination of oil flow rate could be obtained by selective summation of the total flow rate in a steadily loaded full central circumferential groove bearing (Equation 2.10) and the oil flow rate due solely to the shaft translational velocity.

The equation for the oil flow rate from a short bearing, due to shaft translational velocities will now be presented. From Equation 3.9 the pressure generated within a short bearing due to shaft translations can be shown to be given by:-

$$P = -6\eta \left(\frac{r}{c}\right)^2 \left(\frac{b}{d}\right)^2 \left(1 - \left(\frac{2z}{b}\right)^2\right) (\dot{\varepsilon} \cos\theta + \varepsilon (\dot{\phi}+\omega_L) \sin\theta) (1+\varepsilon\cos\theta)^{-3} \tag{3.25}$$

Differentiating to determine the pressure gradient in the (y)-coordinate direction at the bearing edge and substituting into Equation 3.21 gives,

$$Q_T = -\int_{\theta_1}^{\theta^2} rbc\ (\varepsilon\ (\dot{\psi} + \omega_L)\ \cos\theta_1\ -\ \dot{\varepsilon}\ \sin\theta_1)d\theta \qquad (3.26)$$

which for a PI film reduces to,

$$Q_T = 2rbc\ (\varepsilon(\dot{\psi}+\omega_L)\ \cos\theta_1\ -\ \dot{\varepsilon}\ \sin\theta_1) \qquad (3.27)$$

This provides an approximation of the oil flow rate for a short bearing due to shaft translations and may easily be incorporated into any orbit prediction technique which uses the mobility method.

To summarize, the selective summation technique takes the greater of two instantaneous oil flow rates and uses this value when numerically integrating to determine the cyclic oil flow rate. Two sets of equations have been adopted for the selective summation method and these are summarized below.

$$\left.\begin{array}{l} Q_P = \dfrac{0.0327\ P_s\ c_d^{\ 3}}{\eta}\ \left(\dfrac{d}{\bar{b}}\right)\ (1.5\ \varepsilon^2+1) \\[2ex] Q_H = \dfrac{W\ M\ (c_d/d)^2\ c_d}{2\eta} \end{array}\right\}$$

Selective summation of pressure and hydrodynamic flow rates

(3.28)

$$\left.\begin{array}{l} Q = \dfrac{0.0315\ P_s\ c_d^{\ 3}}{\eta}\ \left(\dfrac{d}{\bar{b}}\right)\ (1.5\ \varepsilon^2\ +\ 1) \\[2ex] Q_T = 2rbc\ (\varepsilon(\dot{\psi}+\omega_L)\cos\theta_1\ -\ \dot{\varepsilon}\ \sin\theta_1) \end{array}\right\}$$

Selective summation of steadily loaded bearing flow and translational velocity flow rate

(3.29)

3.5 The Determination of the Bearing Instantaneous and Cyclic Power Losses

Martin (1982) detailed expressions for instantaneous power loss due to shear, pressure and squeeze effects. These are shown as Equations 3.30, 3.31 and 3.32 respectively.

$$H_{SH} = \frac{\eta d^3 \, b \, (\Omega_s - \Omega_B)^2}{4 \, C_d} \quad J_1^{\circ\circ} \tag{3.30}$$

$$H_p = \frac{(\Omega_s + \Omega_B) \text{ We } \sin\psi}{2} \tag{3.31}$$

$$H_{SQ} = W \, V \cos \beta \tag{3.32}$$

The shear power loss (H_{SH}) has two possible solutions depending on the limits of integration of the integral ($J_1^{\circ\circ}$). These may be those for a PI film in which only the shear power loss in the positive oil film pressure region is considered (in this case the limits of integration are from (θ_1) to ($\theta_1 + \pi$) and a power loss map is shown in Appendix 2), or for a complete 2PI film in which the bearing is assumed to be fully flooded. In this case the limits of integration become 0 (zero) and 2π, and ($J_1^{\circ\circ}$) may be determined from,

$$J_1^{\circ\circ} = \frac{2\pi}{\sqrt{1 - \varepsilon^2}} \tag{3.33}$$

The instantaneous total power dissipated in the lubricant film arises chiefly from the shear and squeeze components, with the shear power loss being the dominant quantity.

3.6 Conclusion

This chapter has provided an introduction to the mobility method. Mobility data generation has been described in relation to the short and finite journal bearing cases and the curve fits of Booker (1965) and Goenka (1984) have been checked. The author has introduced equations for the power loss and oil flow rate for dynamically loaded bearings, and this is intended to provide a bench mark against which to compare the more rigorous solution techniques described and developed in Chapter 4, and the experimental data collected in the present work. This is done in Chapter 5 and 7. The conclusions which can be drawn from the work presented in this chapter are:-

(1) The curve fits of Booker (1965) to short bearing mobility data provide an accurate prediction of the actual mobility data, particularly at lower eccentricity ratios where a significant proportion of the generated data is represented by the curve fit to within 1%. However, at higher eccentricity ratios the differences may be as high as 6 or 7%.

(2) The curve fits of Goenka (1984) also provide a good approximation to finite width bearing mobility data. For all the data analysed (including two (b/d) ratios outside the region Goenka curve fitted) the mean percentage difference between the curve fits and actual data was 3.61%. As with the curve fits of Booker (1965) the

percentage differences increased with eccentricity ratio.

(3) The effect of the supply pressure on oil flow rate, power loss and effective oil temperature through the supply pressures effect on journal centre orbit are shown to be minimal for the Ruston & Hornsby 6VEB-X MK111 (full central circumferential groove bearing). This is particularly true of the effective temperature and oil flow rate. The effect on power loss is however larger, but it can be seen to decrease as the inlet oil temperature is increased.

(4) An additional oil flow rate determination technique has been introduced and is referred to as selective summation. The larger of two component instantaneous flow rate (pressure or hydrodynamic) is taken and used when numerically integrating to determine the total cyclic oil flow rate.

CHAPTER 4

CHAPTER 4

THE FILM HISTORY SOLUTION

4.1 Introduction

A simple analytically based solution for the prediction of the journal centre orbit, minimum oil film thickness, oil flow rate and power loss determination was discussed in Chapter 3. However, while the mobility method leads to a rapid prediction of the bearing operating condition, it was noted that due to many simplifications adopted in the solution technique several of the performance characteristics could be in considerable error. It was observed that one of the main reasons for this was the assumptions involved in determining the position of the film rupture and reformation boundaries.

The advent of more powerful digital computers has meant that 'real time' solutions for performance predictions of journal bearings are now becoming possible. Computer coding for solution techniques involving the imposition of the boundary conditions suggested by Jakobsson-Floberg (JF) and Jakobsson-Floberg-Ollson (JFO) (see Chapter 1) have in recent years been developed, although these more rigorous solutions still require large computer run times in most cases. Hence, such solutions are only used for a few special test cases, with the mobility solution being used as the basis of the everyday design method.

In order to restrict the computer run times (a major concern of the present study), the work described in this chapter was undertaken. The more rigorous solution techniques, such as the film history solution, (where the availability and transport of oil in the clearance circle are considered), will be reviewed and the author will present his new approximate film history solution method.

Jones (1982) developed such a technique for dynamically loaded journal bearings but did not give any detailed description of his method, nor did he report any values for the experimental or computer output data discussed in his paper. It is believed that the author's film history solution is similar to that of Jones (1982), except for some important simplifications which were primarily introduced to reduce the computer run time.

The remainder of this chapter deals with a study of a film history based analysis for dynamically loaded journal bearings which is more rigorous than the mobility method of solution described in the previous chapter.

4.2 Rigorous Analysis Techniques for Dynamically Loaded Journal Bearings

Rigorous design techniques rely on real time solutions of the governing Reynolds equation at each time step in the journal orbit. Several methods of determining the position of the rupture and reformation boundaries are reported in the literature and a number of these will be described here, in addition to the simplifications made to the methods to reduce the computer central processing unit time.

4.2.1 The Film History Solution

The Reynolds equation predicts positive hydrodynamic gauge pressures wherever they can be generated in the clearance space of a journal bearing, since no consideration of the actual film extent is taken into account in the formulation of the equation. Since for a dynamically loaded bearing the journal centre position is changing due to changes in the load vector and possibly the surface speeds, two situations which must be addressed by the numerical solution of Reynolds equation are apparent. These are;

(i) Nodes where Reynolds' equation predicts a positive hydrodynamic film pressure but pressure generation is inhibited as there is insufficient oil to provide a full flooded situation.

(ii) Nodes which are fully flooded but Reynolds' equation does not predict a positive oil film gauge pressure at the position.

The actual film extent, at any journal centre position is dependent upon the film extent at the previous journal centre position and the flow of oil over the subsequent period. In order to accommodate this situation, the film history solution has been developed. This keeps a track of the oil availability within the clearance circle of the bearing, and modifies the boundaries of the full film region accordingly.

It was pointed out in Chapter 2 that a film history technique based on the algorithm of Elrod and Adams (1974) and later refined by Elrod (1981) would be very time consuming and may provide convergence problems based on the experience gained in that work. Therefore, a solution technique based on determining the internodal flows and the full film region extent at each time step was considered the most appropriate solution technique.

Jones (1982) and Paydas (1988) have both developed solution techniques based on this method, but Jones does not provide any detailed description of his method, nor any values for the oil flow rates, power losses or the computer run times required by his solution. It is believed that the author's solution approach is similar to those already developed, however, major engineering approximations and simplifications introduced by the author have reduced the solution time and complexity considerably. Figure 4.1 shows a flow chart for the solution technique and the more complex aspects of the method will now be discussed.

(1) It was shown by Jones (1982) that, while film history considerations can have a significant effect on the instantaneous and cyclic oil flow rates, for a full circumferential groove bearing the journal centre orbit was only marginally affected by such considerations. Therefore, in the author's simplified oil film history solution the journal centre velocities and orbit were determined from the mobility curve fits of Booker (1965) or Goenka (1984).

(2) The journal centre velocity components, ($\dot{\varepsilon}$) and ($\varepsilon\dot{\phi}$), at each time step in the orbit were then used in the solution of the Reynolds equation. For the initial journal centre position (at a crank angle of zero degrees) the bearing was

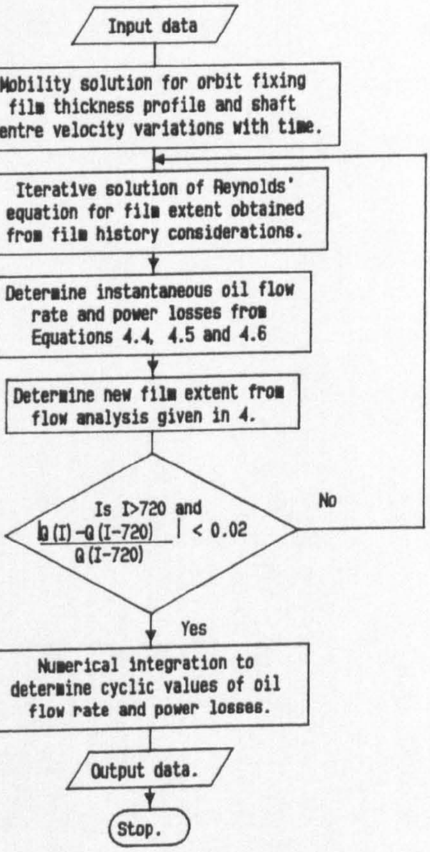

Figure 4.1 Flow Chart For Oil Film History Solution.

considered to be fully flooded since no oil film extent data was available. At subsequent shaft centre positions the boundary between the full film and cavitation region was determined from oil availability considerations within the bearing (step (4)). Two solution techniques were developed during the research.

(i) The Reynolds equation for the full film region was given by:-

$$\frac{\partial}{\partial \theta}\left(\frac{h^3}{12\eta}\frac{\partial P}{\partial \theta}\right) + r^2 \frac{\partial}{\partial y}\left(\frac{h^3}{12\eta}\frac{\partial P}{\partial y}\right) = cr^2 \left(\dot{\varepsilon} \cos\theta + \varepsilon\dot{\phi} \sin\theta\right) \qquad (4.1)$$

For mesh squares which lay in the full film region yet bounded the cavitation region (at reformation), no account of the reduction in the Couette flow from the upstream cavitated mesh square was made. This may lead to an overestimate of the oil flow rate from the bearing due to the prediction of larger pressures in this region of the full film. In addition, a mathematical discontinuity is introduces when the flow analysis given in (4) is carried out.

(ii) For the second solution approach, at reformation, the Couette flow was modified to account for the striation width at the upstream boundary of the mesh square. For mesh squares in the full film region which were adjacent to the reformation boundary the Reynolds equation may be effectively adjusted to compensate for flow continuity considerations by writing:-

$$\frac{\partial}{\partial\theta}\left(\frac{h^3}{12\eta}\frac{\partial P}{\partial\theta}\right) + r^2\frac{\partial}{\partial y}\left(\frac{h^3}{12\eta}\frac{\partial P}{\partial y}\right) = cr^2\left(\dot{\varepsilon}\cos\theta + \varepsilon\dot{\phi}\sin\theta + \left(\frac{\Omega_s+\Omega_B}{2}\right)h\frac{\partial\theta_T}{\partial\theta}\right) \tag{4.2}$$

The extra term essentially imposes the Jakobsson-Floberg (JF) condition at the reformation boundary. In this equation (θ_T) represents the proportion of the mesh square full of oil and (θ) is the angular displacement. For mesh points which are bounded by a fully flooded upstream node, Equation 4.2 reduces to the Reynolds equation.

In each case negative gauge pressures generated during the solution of Reynolds equation were set to zero. This effected the zero pressure gradient condition at the rupture boundary.

(3) The instantaneous side leakage, shear power loss and squeeze power loss were then calculated from Equations 4.3. 4.4 and 4.5.

$$Q = \frac{h^3}{12\eta}\frac{\partial P}{\partial y}\bigg|_{y=b} r d\theta \tag{4.3}$$

$$H_{SH} = \Omega_s \eta r^3\left(\frac{\Omega_s - \Omega_B}{h}\right) d\theta dy + \frac{\Omega_s r h}{2}\frac{\partial P}{\partial\theta}\, d\theta\, dy \tag{4.4}$$

$$H_{SQ} = W\,V\cos\beta \tag{4.5}$$

Equations 4.3 and 4.4 represent the lubricant flow rate from one mesh square at the bearing side and the shear power loss for one mesh square (due to the shaft rotation) respectively. A similar expression for the shear power loss at the bearing surface may also be produced. These equations were then numerically integrated to determine the total oil flow rate and shear power loss at any instant.

It is important at this point to describe the most significant difference between the author's and previous film history techniques. Before calculating the instantaneous oil flow rate and power loss, Jones (1982) and Paydas (1988) determined the hydrodynamic film load acting on the bearing and compared this with the externally applied load. If the agreement was within a predefined tolerance then the assumed velocities used in step 1) were correct. If this was not the case then three 'partial' solutions of Reynolds' equation for the known film extent were carried out. These were for a bearing with shaft rotation and supply pressure, but no squeeze motion, and for unit squeeze velocities in two orthogonal axes, with no shaft rotation or oil supply pressure. This resulted in two simultaneous equations relating the translational velocity components, damping coefficients and hydrodynamic load acting on the bearing to the externally applied load. Solution of the equations gave a new estimate of the journal centre component velocities. Step (2) was then repeated for the new velocity components until the hydrodynamic film and externally applied loads balanced.

In the present analysis the small errors introduced by determining the shaft centre velocity components from mobility curve fit and not balancing the externally applied loads have been neglected. These are, however, only a few percent for the case of a full central circumferential groove bearing, and at high eccentricity ratios they will not affect the journal orbit significantly. This is due to the high film stiffness at high eccentricity ratios, and the inherently good oil supply features of such bearings.

(4) For the pressure profile determined in (2) the inter-nodal flows over the next time step were calculated and used to determine the new film extent after the step. In determining the new film extent it is worth noting the mechanism by which the movement of a node from the full film region, or visa verse, was modelled.

(i) For mesh squares which were in the cavitation region at the beginning of the time step, these could become fully flooded by the control volume reducing in size so that the flows into the control volume over the time step provided a completely flooded mesh square at the end of the step.

(ii) Any node which was in the full film region and was bounded by a fully flooded node at its upstream edge could not become cavitated over the time step. The Reynolds equation had already been used at the beginning of the step to determine hydrodynamic film pressures which ensured continuity of flow, (step 2). These were then considered to be constant over the subsequent step. Hence, a node must remain in the full film region over the time step if it was in the full film region at the beginning of that step. Such nodes can only become cavitated at the beginning of the next time step when the Reynolds equation is re-solved for the new journal centre position and velocity components.

(iii) Mesh squares which lay in the full film region and were bounded by a cavitated upstream node required special consideration. If Equation 4.1 was used to determine the pressure profile in the full film region then these nodes could become cavitated, since the flow from the upstream node was smaller than that considered in the solution of the Reynolds equation. If, however, Equation 4.2 was used to determine the pressure profile then the striation width and modified Couette flow had already been considered and such nodes need only be considered if a zero pressure was predicted at step 2).

Figure 4.2 shows a control volume and the component flows into and out of a typical mesh square. The component (x) co-ordinate direction Couette and Poiseuille control volume inlet oil flow rates are given by Equations 4.6 and 4.7. Similar expressions were applied to determine the other flow rates.

$$(Q_x^{\,c})_{in} = \frac{U}{2}\left(\frac{h_{-1} + h_o}{2}\right) \theta_{-1}\, dy \qquad (4.6)$$

$$(Q_x^{\,P})_{in} = \frac{1}{12\eta}\left(\frac{h_{-1} + h_o}{8}\right) \frac{\partial P}{\partial x}\, dy \qquad (4.7)$$

Nodes which were checked to determine whether they were flood or not at the end of the time step were discussed previously. For these mesh squares the six component flows were calculated and the volume of oil available after the journal centre movement was compared to the new physical size of the control volume. If the volume of oil

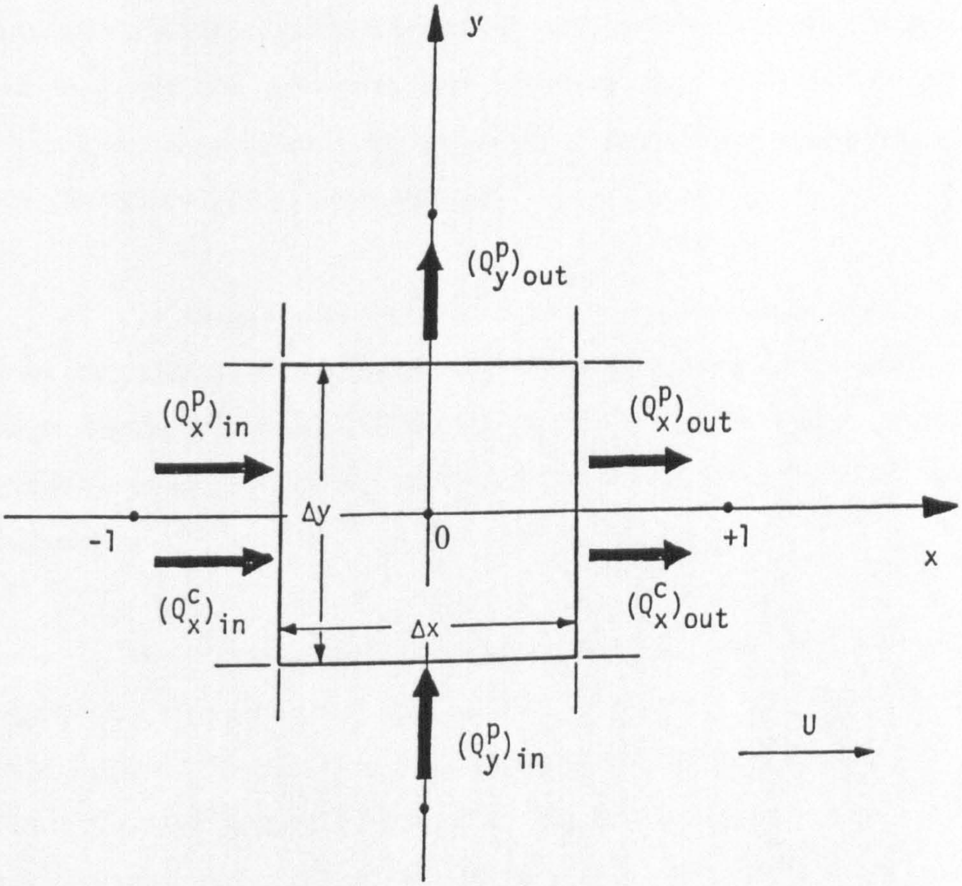

Figure 4.2 Computational Cell Adopted For Oil Flow Continuity Analysis

was greater than 99% of the mesh square volume then the mesh square was considered to be in the full film region and able to generate positive hydrodynamic pressures as predicted by Reynolds' equation. If this was not the case then the proportion of the mesh square filled was determined from the ratio of the volume of available oil to the volume of the mesh square.

In determining the flow into and out of the mesh square over the time step the pressure field and pressure gradients at the mesh square boundaries were considered to remain constant. The pressure gradients were then determined at each of the mesh square boundaries.

The Poiseuille flow components were then determined from equations of the form of (4.7). However, the Couette flow determination is more complex, since to ensure that no mesh square had a negative content of oil after the time step, the mean value of the proportion of the mesh square full of oil over the step was used in the calculation. This was given by,

$$\theta_m = \frac{\theta_{T+1} + \theta_T}{2} \tag{4.8}$$

and may be determined iteratively. However, problems of determining a relaxation factor applicable to all cases led to the development of a direct method. The final value of (θ_{T+1}) was given by,

$$\theta_{T+1} = \frac{\text{Oil volume available at the end of the time step}}{\text{Final volume of mesh square}} \tag{4.9}$$

and since all the component flows, except the outlet Couette flow, were independent of the value of (θ_T) at the mesh point being considered, Equation 4.9 can be rewritten as,

$$Q_{T+1} = \frac{Q_{START} + Q_{STORE}}{Vol_f} - \frac{Q_c}{\theta_T \; Vol_f} \times \theta \qquad (4.10)$$

where Q_{START} - initial volume of oil in the control volume

Q_{STORE} - storage of oil over the time step (excluding the (x) co-ordinate direction outlet Couette flow)

Vol_f - final mesh square volume

θ_c - (x) co-ordinate direction outlet Couette flow based on (θ_T)

θ - independent variable

θ_{T+1} - dependent variable

Equation 4.10 is of the form,

$$\theta_{T+1} = C + m\theta \qquad (4.11)$$

and represents a straight line. The solution of Equation 4.8 was then straightforward.

(5) For the new film region extent obtained in (4), steps (2), (3) and (4) were repeated until a full orbit had been completed. Then, on each subsequent step the oil flow rate from the bearing side was compared with the value calculated at the same crank angle in the previous cycle. If the agreement was within ± 2% then the film extent was assumed to have converged from the initial assumption of a full lubricant film at a crank angle of zero degrees

(top dead centre firing). In this case the instantaneous oil flow rate and power losses for the previous 720° of crankshaft rotation were numerically integrated to give the cyclic values.

It was found that the instantaneous flows usually converged after about 760 time steps when the step length corresponded to one degree of crank rotation.

Detailed output for the film history analysis is given in Chapter 5 where a comparison is presented with the oil flow rate prediction techniques developed in Chapter 3.

4.2.2 Solution Techniques Using the Reynolds and Jakobsson-Floberg Boundary Conditions

As with the film history solution the journal centre orbits were determined using the mobility curve fits of Goenka (1984). This explicit determination of the journal centre velocities reduced the computer run time for the solution. No consideration of the film history was made and the Reynolds or Jakobsson-Floberg boundary conditions were used to determine the cavitation region extent.

The Reynolds boundary condition at film rupture and reformation was achieved by setting all negative gauge pressures generated during the finite difference solution of Reynolds' equation to zero. This is the same boundary condition used by Goenka (1984) and any errors in the orbit determination were therefore due to inaccuracies of the curve fits.

The Jakobsson-Floberg boundary condition was imposed in the same way as described in Chapter 2. The only difference was the inclusion of the journal centre translational velocity terms in the continuity equations.

4.3 Application Of The Film History Solution To Two Test Cases

While it is not intended to present a substantial range of data in this chapter, two test cases have been chosen to demonstrate several important features of the author's film history technique. These are the Ruston and Hornsby 6VEB-X Mk111 operating at the standard conditions given by Campbell et al (1967) and the Ricardo Hydra with a crank rotational frequency of 1500 r.p.m., on effective oil viscosity of 0.0096 Pa.s and an oil supply pressure of 172.4 kN/m^2 (25 p.s.i.).

4.3.1 The Effect Of The Time Step and Orbit Prediction Method On The Solution Parameters

The time step in the orbit is given in terms of degrees of crank rotation and represents the time between successive impositions of the film history considerations of Section 4.2.1 step (4). The time steps used were 1,2,3,4,5 and 10 degrees of crank rotation and the oil flow rate, total power loss and time for a converged solution are shown in Tables 4.1a and 4.1b for the two bearings analysed. The solution times using journal centre velocities from the mobility curve fits of Booker (1965) and Goenka (1984) were so close that mean values are given in the tables. The film history solution based on the solution of Reynolds equation in the form given by Equation 4.2 has been used for the present comparison. The results for the alternative method vary only slightly for the cases considered.

Time Step (degrees)	Booker (1965)		Goenka (1984)		Solution Time(s)
	$Q(m^3/s)x10^{-6}$	H (Watts)	$Q(m^3/s)x10^{-6}$	H (Watts)	
1	47.0	1036	47.9	1194	239
2	48.5	1038	48.7	1186	128
3	47.4	1037	48.1	1187	87
4	48.5	1034	47.6	1186	68
5	45.2*	1036	48.1	1178	56
10	48.1	1051	50.4*	1172	30

Table 4.1(a) The Effect Of Time Step And Orbit Prediction On Oil Flow Rate And Total Power Loss (Ruston and Hornsby 6VEB-X Mk111)

Time Step (degrees)	Booker (1965)		Goenka (1984)		Solution Time(s)
	$Q(m^3/s)x10^{-6}$	H (Watts)	$Q(m^3/s)x10^{-6}$	H (Watts)	
1	8.37	29.5	8.73	30.9	206
2	8.62	29.3	8.89	29.8	111
3	8.63	29.3	8.88	29.8	78
4	8.70	29.2	8.87	29.5	59
5	8.68	29.1	8.84	29.7	49
10	7.95	29.1	8.75	29.6	26

Table 4.1(b) The Effect Of Time Step And Orbit Prediction On Oil Flow Rate Total Power Loss (Ricardo Hydra)

It can be seen from the table that the range of power losses and oil flow rate variations with time step are generally within about 2 or 3% for the two orbit prediction methods given. However, for the flow rate predictions for the Ruston and Hornsby 6VEB-X MK111 (6VEB) and the flow rate predictions based on the Booker mobility orbit for the Ricardo Hydra, predictions which are out of step with the values at time steps on either side are obtained. This causes the range of flow rate variations with time step to increase to as much as 9.4%. These values are marked by (*) and occur at the coarser time steps of 5 and 10°. It can also be seen that as the time step is increased from 1 to 10° the mean solution time decreases from 239 to 80 seconds for the 6VEB and from 206 to 26 seconds for the Ricardo Hydra. This represents a decrease by a factor of about 8.

The most noticeable effect of the different mobility equations used in the journal orbit determination is on the total power loss. The values determined using both sets of mobility curves differ by as much as 15.0% with all of the time steps giving differences greater than 10% for the 6VEB. For the Ricardo Hydra the differences are 4 or 5%. These differences are due to the velocities predicted using Goenka's finite bearing mobility curve fits giving a greater proportion of the journal orbit at higher eccentricity ratios, and hence increasing the shear rate across the oil film. It should, however, be noted that the agreement in the oil flow rate was less influenced by the journal orbit. For time steps of 4° and less, the oil flow rates agreed to within 2% between orbits for the 6VEB and 5% for the Ricardo Hydra.

While the present analysis for time steps smaller than 4 degrees of crank rotation shows negligible effect on the output values of oil flow rate and power loss, the results of Paydas (1988) showed significant differences. Differences of as great as 20% for power losses and oil flow rates for time steps of 0.5 and 10 degrees were observed. The reason for the significant differences is uncertain but the author believes that they could be due to the mesh size-time step combination. This will be discussed in Section 4.3.3.

All the values given in Tables 4.1(a) and 4.1(b) are broadly in line with the limited available data. Martin (1985) gives the total power loss as 1.29 kW for the oil film history solution of Jones (1982) and the oil flow rate as 46 x 10^{-6} m^3/s for the same analysis of the Ruston and Hornsby 6VEB-X Mk111. Paydas (1988) gives slightly lower values for the side leakage and power loss within the bearing. He gives the oil flow rate as 44 x 10^{-6} m^3/s and the power loss as 1.16 kW. The experimentally determined oil flow rate for the Hydra was 7.96 x 10^{-6} m^3/s.

4.3.2 Comparison of the Solution Time With Previous History Techniques

The main difference in the computer run times for the present film history solution and that of Jones (1982) and Paydas (1986) is due to the requirement of additional solutions of Reynolds' equation at each time step so as to determine the correct journal centre velocity. This enabled the oil film load to be balanced against the externally applied load. The minimum number of times that the Reynolds equation was solved per step was once and this corresponded to the case where the shaft centre velocity was fortuitously chosen to give a force balance. If subsequent iterations on the journal centre velocity were required, (Paydas (1988) reported using as many as 7 without satisfactory convergence) each subsequent iteration required the Reynolds equation to be solved 4 times (3 partial solutions and an additional solution of Reynolds equation for the new journal centre velocity). Hence, it can be seen that the present film history solution could be expected to reduce the computer run time by at least a factor of 4 and for some shaft centre positions by a factor of 28.

Paydas (1988) suggested that the optimum time step and mesh sizes for his solution technique were 1° of crank rotation and 10 axial by 80 circumferential nodes. For the Ruston and Hornsby 6VEB-X Mk111 the author has estimated the computer run time that the solution method of Paydas would take on the Amdahl 570 on the basis of the solution time given by Paydas. The estimate is 3800 seconds, compared to run times of between 240 seconds for a 1° time step and 60 seconds for a 4° time step for the present analysis. This is a reduction in computing time of a factor of between 15.8 for a 1° time step and 63 for a 4° time step, although it should be recognised that these are for optimum conditions suggested by each author.

4.3.3. Mesh Size-Time Step Combination

Paydas (1988) showed that in his solution the values of the oil flow rate and the power loss were significantly affected by the time step used in the solution. Paydas used a 10 axial by 80 circumferential mesh and showed differences in oil flow rates and power losses as high as 23% for time steps of 0.5 and 10 degrees of crank rotation.

He found that at coarser mesh sizes the number of iterations on the shaft centre velocity reached a maximum of 7 without satisfactory convergence. Problems of determining the correct cavitation boundary positions were also reported.

The differences in the oil flow rates and power losses in Paydas' analysis and at coarser time steps in the present analysis could be due to the time step-mesh size combination. Since the reformation boundary could be limited to 1 mesh square movement into the full film region per time step, it is apparent that for a fine mesh, small time steps are required. If a coarse time step is used the boundary may be required to move more than one mesh square which is not catered for.

This is particularly true when the journal centre is operating at a high eccentricity ratio and low attitude angle.

4.4 Discussion and Conclusions

An in-depth description of the author's film history solution has been given, and the benefit of determining the shaft centre velocities from the mobility curve fits of Booker (1965) or Goenka (1984), in terms of the reduced computer solution time, has been shown. However, it should be noted that the supply pressure effect on journal orbit (Chapter 3, Section 3.3.3), and the minimal effect of film history considerations on journal orbit have been neglected. From the author's analysis it can be concluded that:-

(1) For full central circumferentially grooved bearings the film history effects on the journal orbit is negligible and

the journal centre velocities can be determined from the mobility curve fits of Booker (1965) and Goenka (1984).

(2) Irrespective of which mobility curve fits were used in the orbit determination, the cyclic oil flow rate was only affected by about 2 or 3% at smaller time steps.

(3) The oil flow rate and shear power loss were only marginally affected by the time step for steps of 4 degrees of crank rotation or less.

(4) The orbit method determination (Booker (1965) or Goenka (1984)) had a much greater effect on the power loss than it had on the oil flow rate. The increased proportion of the orbit at higher eccentricities predicted by the mobility curve fits of Goenka (1984) caused an increase in power loss of over 10% when compared with the value for the orbit determined using the curve fits of Booker (1965).

(5) Since the oil flow rate and power loss were only marginally affected by time steps smaller than 4° of crank rotation, it would seem that these time steps were small enough to provide a converged solution and predict the correct cavitation boundary motion.

(6) The present analysis significantly reduced the computer run times by factors of between 15.8 and 63 for the optimum mesh sizes and time steps chosen by Paydas (1988) and the author.

(7) The values of the oil flow rates and power losses for the two bearings agreed well with the limited published data.

CHAPTER 5

CHAPTER 5

EVALUATION OF THE AUTHOR'S PREDICTIVE TECHNIQUES

5.1 Introduction

In this chapter the results from the author's analysis techniques (developed in Chapters 3 and 4) for the performance prediction of dynamically loaded journal bearings are compared with the data presented by Jones (1982), Cooke (1983) and Paydas (1988). The three predictive techniques are:-

(1) Oil flow rate and power loss predictions based on simple expressions for the component terms. These include the pressure and hydrodynamic flows and the shear, squeeze and pressure power loss terms (see Chapter 3).

(2) Performance predictions based on more rigorous analyses involving the 'real time' solution of the Reynolds equation, with either the Reynolds or Jakobsson-Floberg boundary condition (see Chapter 4).

(3) The film history solution. This was the most complex technique developed and involved keeping a track of the oil availability within the bearing. (see Chapter 4).

The standard case of the Ruston and Hornsby 6VEB-X Mk111 was analysed, with particular attention being given to the influence of the oil supply pressure and journal rotational speed on the bearing side leakage and power loss. The analysis was subsequently extended to give a 'thermal solution', in which the effective oil temperature was not given as input data to the computer programs, but was calculated from a thermal balance within the bearing. This involved equating the total power loss to the product of the oil specific heat, mass flow rate and temperature rise through the bearing.

Some important specifications adopted for the determination of the performance of the Ruston and Hornsby 6VEB-X Mk111 are given below:

Overall bearing width	127.0 mm
Width of one land	57.15 mm
Bearing diameter	203.2 mm
Diametral clearance	0.165 mm
Engine speed	600 r.p.m. (10 Hz)
Lubricant dynamic viscosity	0.0095 Pa.s at 100 °C
	0.097 Pa.s at 40 °C
Oil supply pressure	276 kN/m^2 (40 psi)
Oil density x specific heat	1.78×10^3 kJ/m^3 °C

Very full details of all the data required to calculate the orbit of the crank pin within the big-end housing are presented by Campbell et al (1967), including the loading to be carried resulting from cylinder pressures and inertial effects. For the computations carried out in this reference a fixed operating viscosity of 0.015 Pa.s was used, however, for the thermal solutions presented in the present work, the effective oil viscosity was calculated from the temperature-viscosity relation used in the ASTM (American Society for Testing Materials) chart. This is given by,

$$\log\log(\nu + 0.6) = C1 - C2 \log T \tag{5.1}$$

where (C1) and (C2) are constants, (ν) is the kinematic viscosity in centistokes and (T) is the absolute oil temperature. Equation 5.1 is based on the Walther equation and is discussed by Cameron (1981).

It was shown in Chapter 4 that the method of orbit determination (short or finite bearing mobility data curve fits), for the author's film history solution, had little effect on the oil flow rate from the Ruston and Hornsby 6VEB-X Mk111, while a difference of about 10% could be seen in the shear power loss for this bearing. Hence, in this chapter the author's solution techniques, based on film history considerations and the imposition of the Jakobsson-Floberg or Reynolds boundary condition, will be applied to a journal centre orbit determined from the finite bearing mobility curve fits of Goenka (1984). In addition, where the simple expressions for the power loss and oil flow rate components are used the journal centre orbit will be determined from the short bearing mobility curve fits of Booker (1965). The reasons for this will become apparent in Sections 5.2, 5.3 and 5.5.

5.2 Power Loss Prediction In Full Central Circumferential Groove Bearings

Figure 5.1 shows the power loss variation with crank angle for the Ruston and Hornsby 6VEB-X Mk111 big-end bearing. This has been predicted using the equations given in Chapter 3 for a journal centre orbit determined from the short bearing mobility curve fits of Booker (1965).

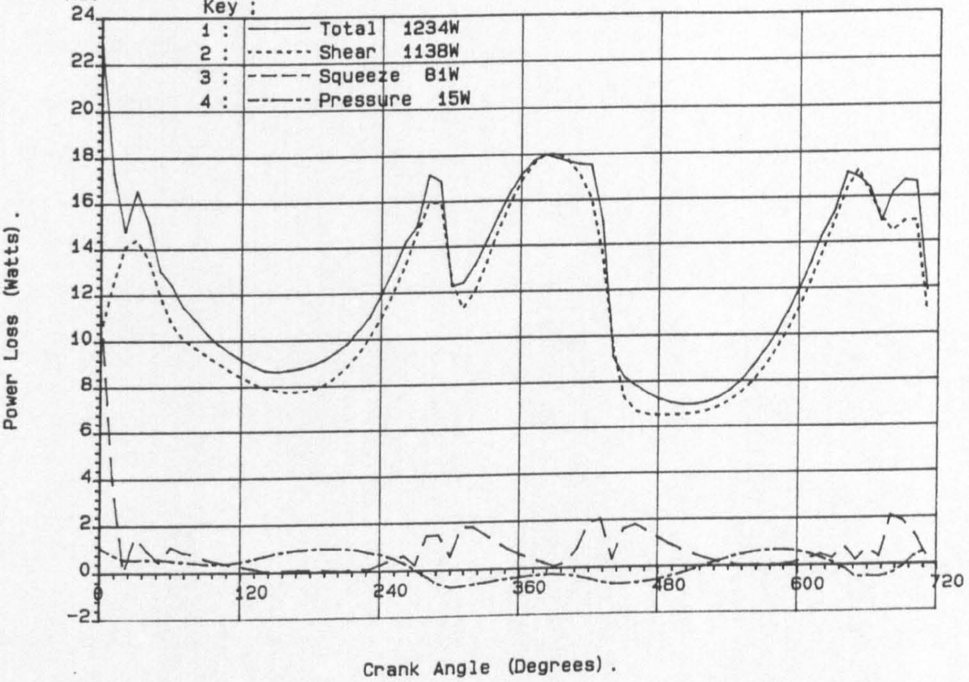

Figure 5.1 Component Power Loss Variations With Crank Angle. (Simple Analysis)

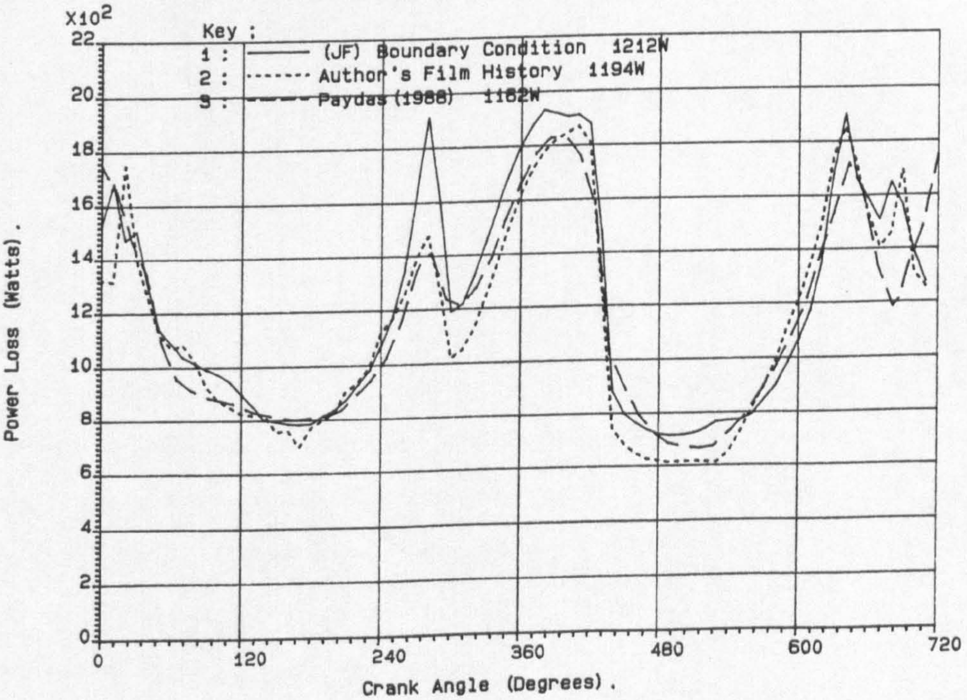

Figure 5.2 Total Power Loss Variation With Crank Angle. (Rigorous Analyses)

Power Loss Component	Power Loss (Watts)	Percentage of Total (%)
Shear (2π)	1138	92.2
Squeeze	81	6.6
Pressure	15	1.2
Total	1234	100

Table 5.1 Breakdown of the Power Loss in the Ruston and Hornsby 6VEB-X Mk111 Big-End Bearing (Short Bearing Mobility Orbit - Booker (1965))

It can be seen from Figure 5.1 and Table 5.1 that the shear power loss component accounts for the majority of the total loss in the bearing under consideration. A similar breakdown was given for all the predictive techniques given in the present work, although slight variations were obtained in the actual values.

Figure 5.2 gives a comparison of the cyclic variation of the total power loss with crank angle for the author's solution techniques using the Jakobsson-Floberg boundary condition and considering film history effects, with the film history solution of Paydas (1988). Only three predictions are given in this figure, since addition of other curves would only obscure some of the results presented. However, numerical values for the total power loss are given in Table 5.2 for the curves shown in Figure 5.2, and those of other researchers. In addition, the percentage differences of each solution, relative to the author's film history solution, are given in the right hand column.

Analysis Approach			Total Power Loss (Watts)	Percentage difference from (i) (%)
Author's Predictions	(i)	Oil film history (Finite Bearing Orbit)	1194	0.0
	(ii)	Reynolds'Boundary Condition	1229	+ 2.9
	(iii)	Jakobsson-Floberg Boundary Condition	1212	+ 1.5
	Simple Expression*			
	(iv)	Short bearing orbit prediction	1234	+ 3.4
	(v)	Finite bearing orbit prediction	1337	+ 12.0
Martin (1985)	(vi)	Glacier (Oil film history)	1290	+ 8.0
	(vii)	Glacier* (Short bearing)	1260	+ 5.5
	(viii)	Paydas (1988) (Oil film history)	1162	- 2.7

* Equations 3.30, 3.31 and 3.32. A full flooded bearing is considered (see Chapter 3). Glacier refers to 'The Glacier Metal Company Limited'.

Table 5.2 Summary of the Power Loss Predictions of Several Authors. (Ruston and Hornsby 6VEB-X Mk111)

Several important points should be noted from Figure 5.2 and Table 5.2. These are given below:

(1) The boundary condition used to determine the cavitation region extent has little effect on the instantaneous and cycle average power loss. Indeed, the agreement of the cycle average power losses for the curves shown in Figure 5.2 is within about 4.2%. This indicates the validity of the author's 'film history solution technique' where the journal centre orbit and instantaneous velocities were determined from finite bearing moblity curve fits, without a consideration of film history effects. The difference in the power loss predicted by the film history solution of Paydas (1988) and the author is only -2.7%.

(2) All the author's power loss predictions, except (v), lie within the film history predictions of Paydas (1988) and Martin (1985). These show a percentage difference of about 11%.

(3) The power losses predicted by the author vary by about 12%. Comparison of solutions (i) and (v) show that this difference is mainly due to film history considerations, and hence the presence of the cavitation region in the former solution.

(4) It can be seen from a comparison of the values predicted by the author's film history solution (i), and simple expressions for the component power loss terms based on the short bearing orbit prediction (iv), that a difference of only 3.4% is observed. These solutions are, however, based on different orbits and a fully flooded bearing is assumed in the latter case. Hence, the increase in power loss due to considering a full flooded bearing in (iv), is almost balanced by the presence of a cavitation region in (i) and the increased shear power loss due to higher eccentricity ratios predicted in this solution (Note solution (i) was based on the orbit predicted from the finite bearing mobility curve fits of Goenka (1984) and solution (iv) was based on the short bearing mobility curve fits of Booker (1965)).

In view of the points raised above, it can be seen that the rigorous solution techniques involving the real time solution of the Reynolds equation have no benefit in predicting the power loss for this particular bearing. This will also be pointed out in Section 5.5.

5.3 Oil Flow Rate Prediction In Full Circumferential Groove Bearings

Figures 5.3*, 5.4, 5.5 and 5.6 show the instantaneous oil flow rate variations with crank angle for several predictive techniques and the cycle average values are shown in Table 5.3. Close examination of the table and figures shows several important and interesting features which will now be discussed.

It can be seen from Figure 5.3 that the pressure flow rate gives an almost constant value for the whole of the engine cycle, the cycle average value being 42.2×10^{-6} m^3/s. However, three small dips in the curve can be seen at crank angles of about 0°, 300° and 450°. These correspond to positions in the journal orbit where the journal centre lies at smaller eccentricity ratios than for the remainder of the orbit. It should also be noted that these are the positions of the hydrodynamic flow peaks where the maximum journal centre velocities occur.

The close agreement of the author's film history and selective summation technique is shown in Figure 5.4 where the cycle average oil flow rates agree to within 1.5%. For the selective summation technique the instantaneous oil flow rates have been predicted from the steady state flow rate (Q_s) and the translational flow rate (Q_T) equations. These equations are given below and the

---

* This has been published previously by Clayton and Taylor (1988). However, the flow rates given in the previous publications differ slightly from those given here due to a computer coding error.

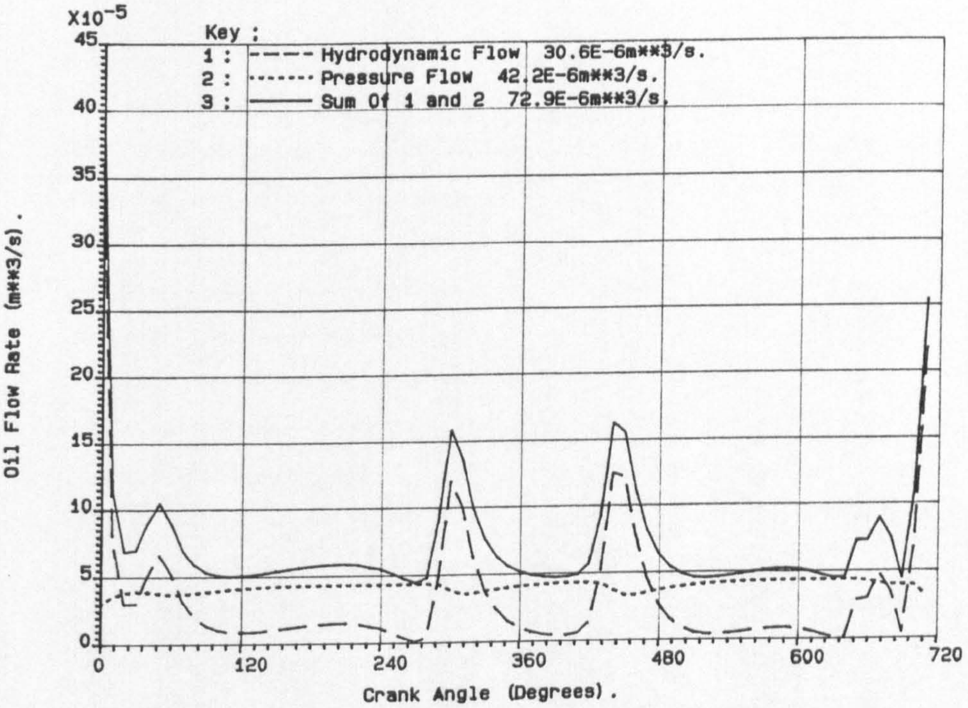

Figure 5.3 Oil Flow Rate Variation With Crank Angle.
(Simple Analysis)

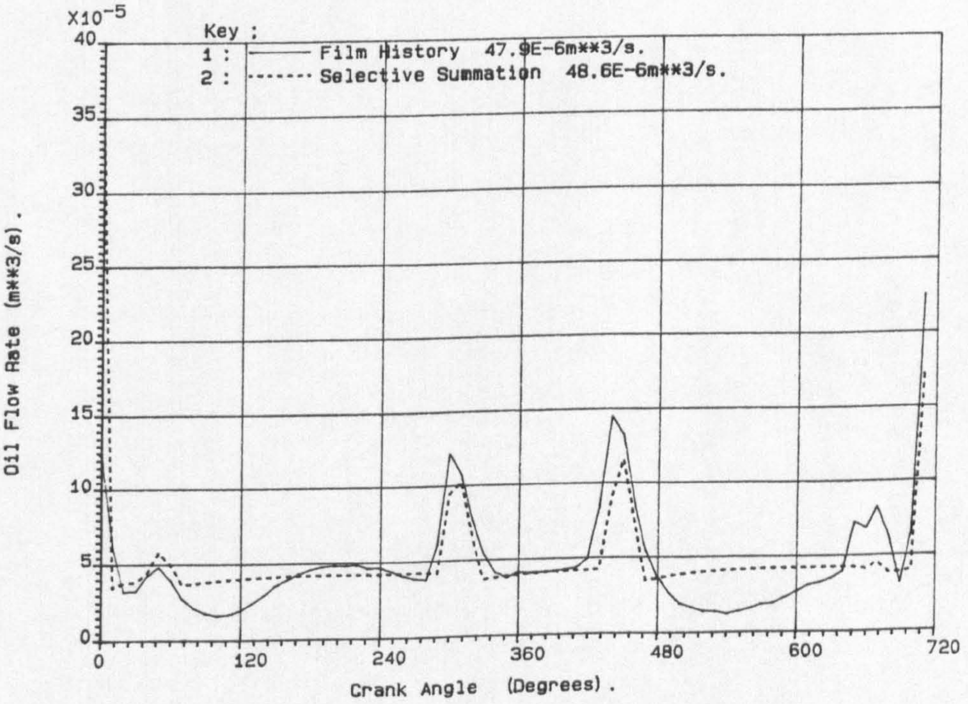

Figure 5.4 Oil Flow Rate Variation With Crank Angle.
(Author's Film History And Selective Summation Techniques)

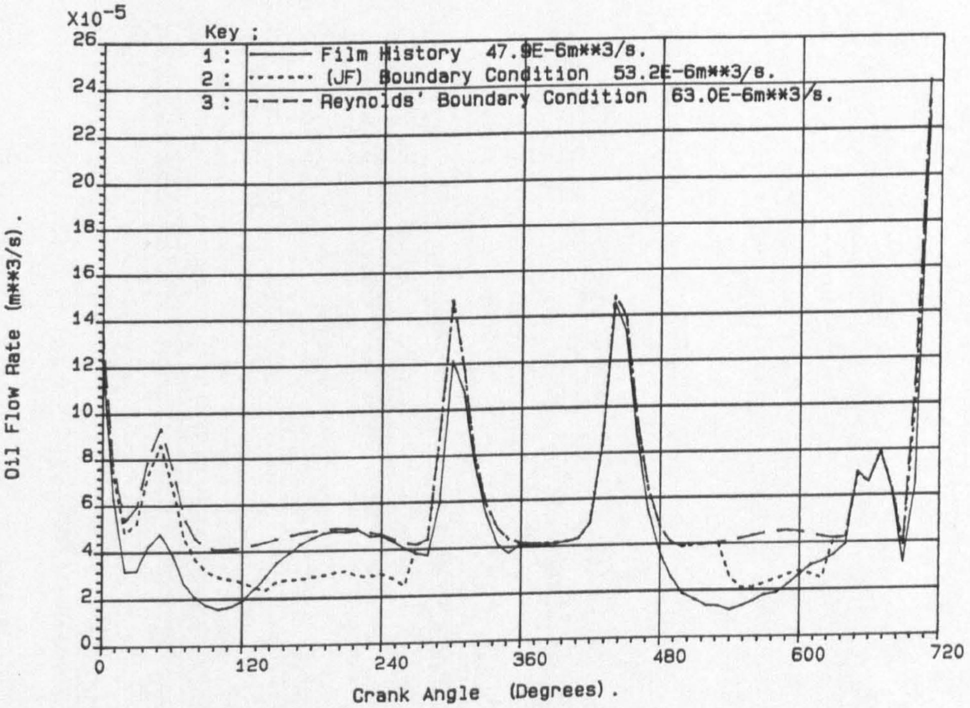

Figure 5.5 Oil Flow Rate Variation With Crank Angle.
(Author's Rigorous Analyses)

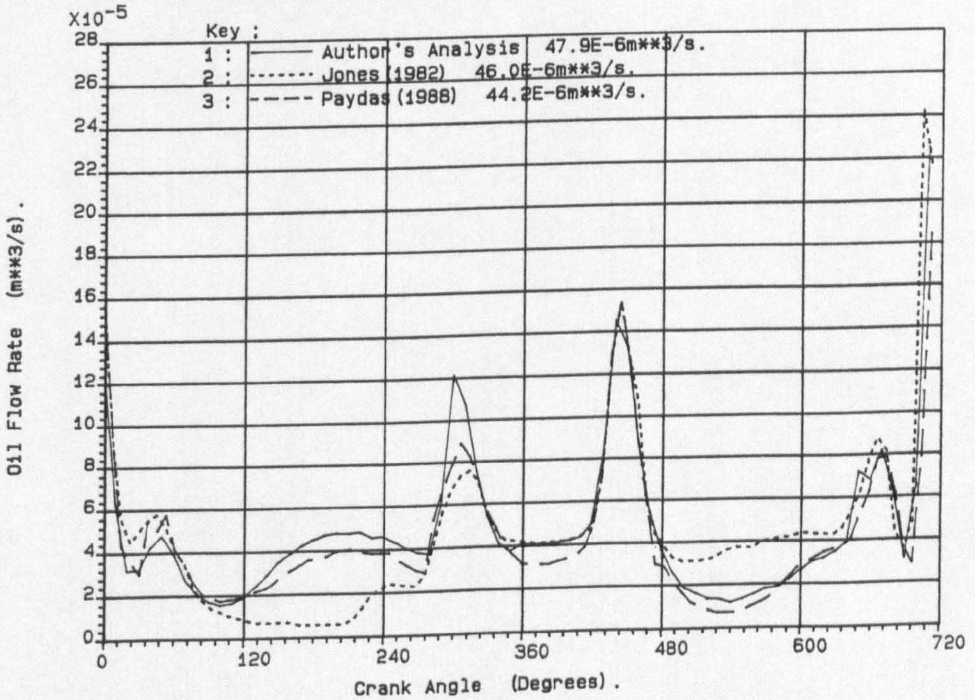

Figure 5.6 Oil Flow Rate Variation With Crank Angle.
(Comparison With Previous Film History Solutions)

	Analysis Approach	Predicted Oil Flow Rate $(m^3/s) \times 10^6$	Percentage difference from (i(b)) (%)
Author's Predictions	(i) Oil Film History Solution		
	(a) Booker Mobility Orbit	47.01	1.9
	(b) Goenka Mobility Orbit	47.9	0.0
	(ii) Reynolds Boundary Condition	63.0	31.5
	(iii) Jakobsson-Floberg Boundary Condition	53.2	11.1
	(iv) Selective Summation of Q_s and Q_T (Booker (1965) Mobility Orbit)	48.6	1.5
	(v) Pressure Flow (Booker (1965) Mobility Orbit)	42.2	-11.9
(vi) Jones* (1982) Oil Film History		46.0	4.0
(vii) Paydas (1988) Oil Film History		44.1	7.9

* Private communication with Mr F A Martin (1989)

Table 5.3 Summary of the Oil Flow Rates Predictions by the Author and Other Researchers reason for the author's preference in using these in his selective summation technique, instead of the pressure and hydrodynamic flow rate equations, was discussed in Section 3.4.2 of Chapter 3.

$$Q_s = 0.0315 \frac{P_s \, c_d^{\,3}}{\eta} \left(\frac{d}{b}\right) (1.5 \, \varepsilon^2 + 1) \tag{5.2}$$

$$Q_T = 2rbc \left(\varepsilon \, (\dot{\psi}+\omega_L) \cos\theta_1 - \dot{\varepsilon}\sin\theta_1\right) \tag{5.3}$$

It is important at this point to remind the reader that the selective summation technique calculates the instantaneous oil flow rates from Equations 5.2 and 5.3 for the whole of the engine cycle. However, when numerically integrating to determine the cycle average value, the larger of the two instantaneous flow rates is used in the calculation.

Figure 5.5 shows the oil flow rate variation with crank angle for the rigorous analysis techniques developed by the author. These include the film history solution and the imposition of the Jakobsson-Floberg and Reynolds boundary conditions to determine the cavitation region extent. It can be seen that unlike the case discussed in Section 5.2 where the boundary conditions frequently had little effect on the bearing power loss, for oil flow rate predictions they are of particular important. It can be seen from Table 5.3 that the Reynolds boundary condition gives a cycle average oil flow rate over 31% greater than that predicted by the author's film history solution, whereas the Jakobsson-Floberg boundary condition gives a value only 11% higher than with the latter solution technique.

It should also be noted from Figure 5.5 that even though the film history solution gives a lower cycle average oil flow rate than that where the Jakobsson-Floberg boundary condition is used, the film history solution gives higher instantaneous oil flow rates at some crank angle positions. This is particularly noticeable between a crank angle of about 140° and 260°. The reason for this is that for a journal centre motion which causes the reformation boundary to move into the full film region, the boundary may not be able to move fast enough with the analysis approach developed. Hence, oil becomes available at high film thickness positions where positive hydrodynamic film pressures can be generated, and as a result the high flow rates are obtained. For cases where the reformation boundary is only required to move a small angular distance per time step, the flow rate given by the Jakobsson-Floberg boundary condition will be approached.

Figure 5.5 also shows positions in the engine cycle where the oil flow rate approaches that predicted by the solution where the Reynolds boundary condition was used to determine the cavitation region extent. This is the maximum possible oil flow rate since oil is considered to be present at all positions within the bearing clearance where positive hydrodynamic pressures can be generated. Hence, at crank angles of about 200° the reformation boundary position predicted by the film history solution is close to that predicted by the Reynolds boundary condition of setting all negative gauge pressures to zero.

A comparison of the author's film history solution and those of Jones (1982) and Paydas (1988) is given in Figure 5.6 where the oil flow rate variation with crankshaft angle is plotted. The cycle average flow rates show excellent agreement, which from Table 5.3 can be seen to give cycle average values which agree to within 8%. It can be seen from Figure 5.6 that the author's film history solution gives a cyclic variation which agrees more closely with that predicted by Paydas (1988), although the cycle average value agrees better with that given by Jones (1982). The difference in the oil flow rate predicted by Jones (1982) and the author's solution is only 4%.

The close agreement of the author's film history solution with the previous published results is a clear indication of the minimal effect film history considerations have on the journal centre orbit for the Ruston and Hornsby 6VEB-X Mk111. Hopefully, this will be true of all full central circumferentially grooved bearings. Indeed, even though Jones (1982) and Paydas (1988) take account of the film history effects on the journal centre orbit, it can be seen (from Figure 5.6) that large differences in the instantaneous oil flow are obtained at crank angles around 200° and 550° for the two solutions. The instantaneous oil flow rates differ by as much as a factor of 7.

Comparison of Figures 5.5 and 5.6 show that the film history solution of Paydas (1988) gives instantaneous oil flow rates greater than those predicted by the author's solution using the Jakobsson-Floberg boundary condition. The reasons for this were discussed previously, although it is interesting to notice that the film history solution of Jones (1982) does not give oil flow rates larger than the author's solution using the Jakobsson-Floberg boundary condition.

5.4 The Experimental Investigation of Cooke (1983)

Using the NEL (National Engineering Laboratories) engine bearing simulator, Cooke (1983) carried out an extensive experimental investigation into the effect of the groove arrangement, oil supply pressure and journal rotational speed on the oil film pressure and side leakage from several engine bearings. Three of the bearings simulated on his apparatus had full circumferential grooves, these were the Ruston and Hornsby 6VEB-X Mk111, the Perkins T6.354 and the MOD ASR1. In the present work the author has used the results relating to the Ruston and Hornsby 6VEB-X Mk111 for comparative purposes, since Cooke gave experimental readings at several different journal rotational speeds for this engine. In addition, the dimensionless oil supply pressure for this bearing was generally lower than those of the other two engines, hence providing a more realistic test for the author's film history solution technique.

Some important specifications adopted for the experimental investigation of Cooke are given below;

Width of one land	12.7 mm
Bearing diameter	63.5 mm
Diametral clearance	0.066 mm

Cooke scaled the actual bearing loads to suitable values for the engine bearing simulator rig by ensuring that the actual bearing and the test bearing were subjected to the same dimensionless load.

The effective viscosity of the lubricating oil at the three oil supply pressures are given in Table 5.4. This is for a shaft rotational speed of 700 r.p.m. These viscosities were considered to apply to other rotational speeds used by Cooke, although this is not clear from his paper.

Oil Supply Pressure (kN/m^2)	Effective Oil Viscosity (Ns/m^2)
200	0.01022
410	0.01107
620	0.01166

Table 5.4 The Effective Oil Viscosities Used by Cooke (1983)

Figure 5.7 shows the oil flow rate variation with oil supply pressure for a journal rotational speed of 490 r.p.m. It can be seen that at low oil supply pressures all the author's predictive techniques over-estimate the experimental data, whereas at an oil supply pressure of 620 kN/m^2 all the techniques under-estimate the experimentally measured oil flow rate. This characteristic was observed for all the shaft speeds used by Cooke. In addition, an almost linear variation of oil flow rate was obtained. For the pressure flow equation the variation would be linear if a constant oil viscosity has been used.

Figure 5.8 shows the oil flow rate variation with shaft rotational speed for the three oil supply pressures. It can be seen that there is a slight decrease in the oil flow rate with speed for most of the author's predicted solutions. Cooke (1983) suggested that a physical explanation of this was that the predominant axial flow in the bearing was inhibited by the increasing circumferential

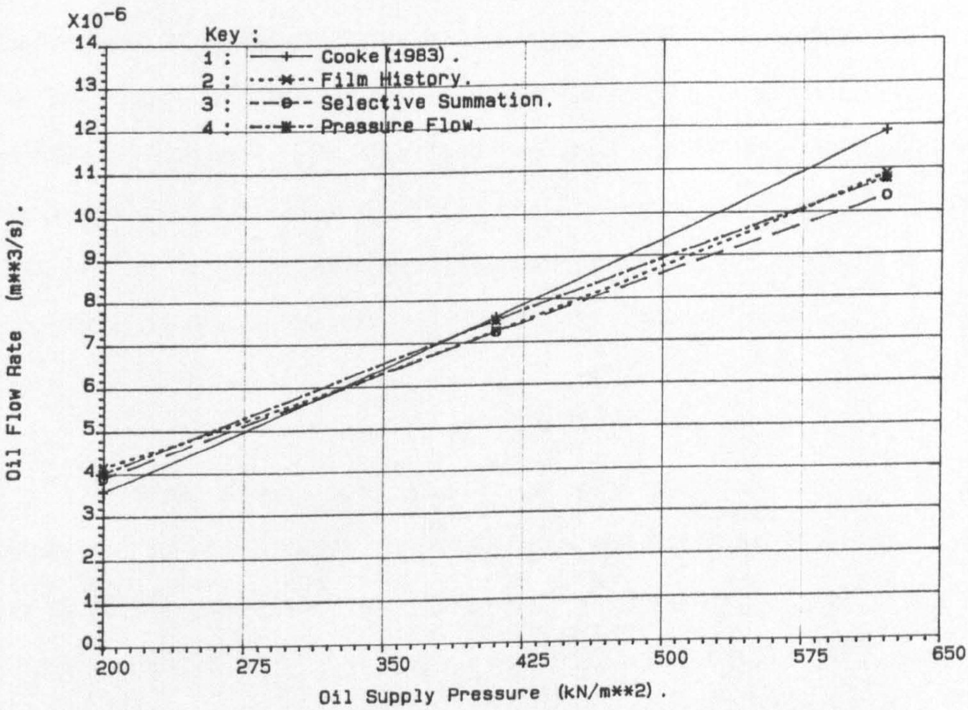

Figure 5.7 Oil Flow Rate Variation With Oil Supply Pressure. (Comparison With Cooke (1983), Note false origin).

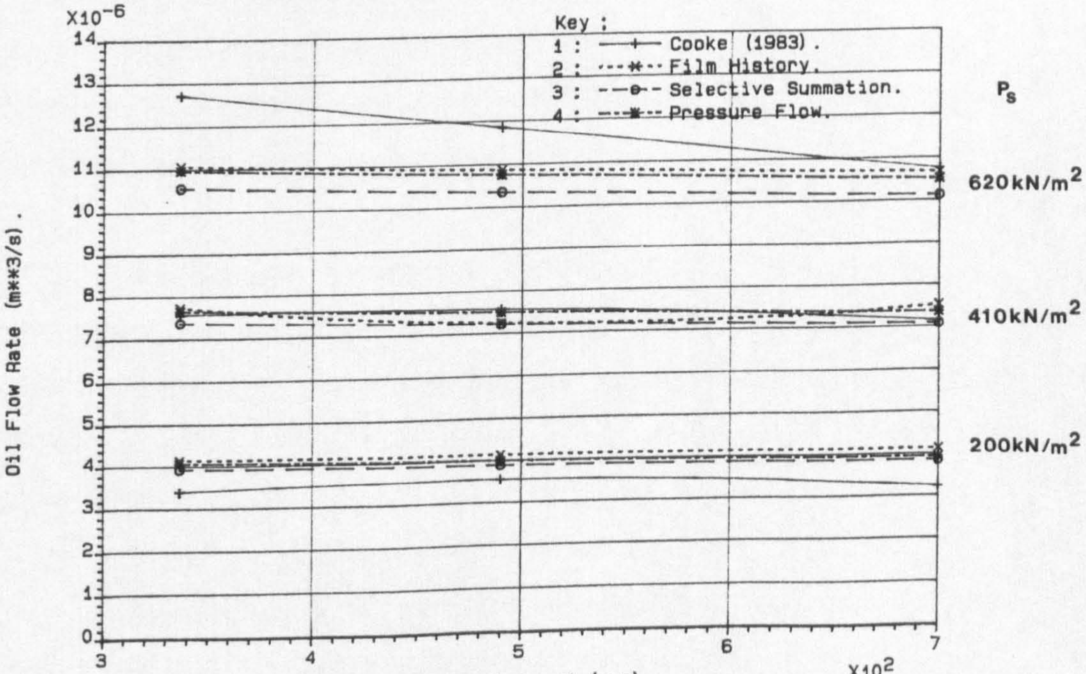

Figure 5.8 Oil Flow Rate Variation With Shaft Speed. (Comparison With Cooke (1983), Note false origin).

velocity. However, comparison of the orbit plots at the three shaft speeds showed that the minimum film thickness generally increase throughout the engine cycle as the shaft speed increases. Hence, it is more appropriate to say that as the shaft rotational speed is increased the oil flow rate from the full circumferentially grooved bearings decreases due to the journal centre orbiting the bearing centre at reduced eccentricity ratios. The effect of the eccentricity ratio on the oil flow rate can be seen from Equation 5.2.

From Figure 5.8 it can be seen that at an oil supply pressure of 200 kN/m^2 the author's predictive techniques over estimate the oil flow rate from the bearing, whereas at a supply pressure of 620 kN/m^2 the opposite applies. It should also be noted that the film history solution tends to give the highest oil flow rates, while the selective summation technique gives the lowest. Hence, it can be seen that the selective summation technique gives the best agreement with the experimental data at an oil supply pressure of 200 kN/m^2 and the film history solution gives the best correlation at a supply pressure of 620 kN/m^2.

The average discrepancy between the author's oil flow rate predictions and the experimental data is about 18%. However, for a supply pressure of 410 kN/m^2 all the predictive techniques give close agreement with the experimental data, with a maximum discrepancy of 5.1%.

It can be seen from the figure, that for the bearing considered, there is no benefit in using the rigorous film history solution technique as opposed to the simpler expression for the pressure flow rate. This is because of the high dimensionless supply pressures of the bearing and the resulting small cavitation region size.

5.5 The Development of a Thermal Analysis

For the results presented previously the oil effective viscosity was given as input to the performance calculations. However, in this section the analysis is extended and the effective temperature is calculated from a thermal balance between the bearing power loss and the product of the oil mass flow rate, specific heat and the oil temperature rise through the bearing.

Figure 5.9 shows the total power loss variation with effective oil temperature for the author's film history solution and the simple expressions for the power loss components given in Chapter 3. In the latter case two predictions of the power loss are given for orbits predicted using the short and finite bearing mobility curve fits of Booker (1965) and Goenka (1984) respectively. In both cases the shear component was calculated by considering a fully flooded bearing. The agreement for all three solutions is excellent, particularly between the film history solution and the power loss calculated from the simple expressions and the short bearing mobility curve fits of Booker (1965). A maximum percentage difference of about 7.5% is obtained at an effective oil temperature of 60°C for this solution, compared to 13.5% for the prediction based on the finite bearing mobility curve fits of Goenka (1984). At higher effective oil temperatures the difference between the short bearing solution and the film history technique are even smaller.

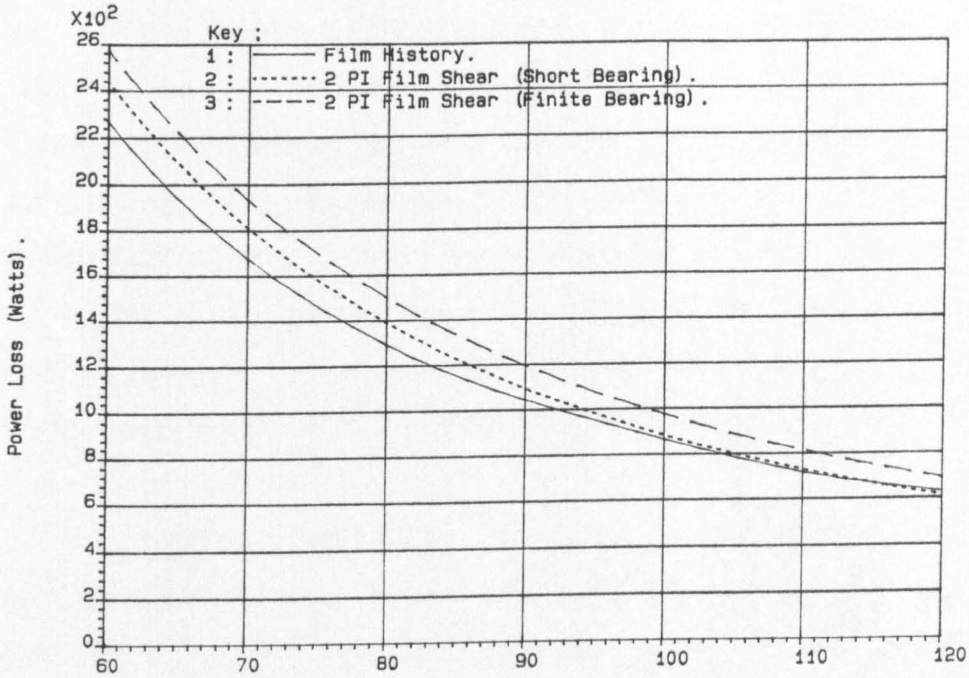

Figure 5.9 Power Loss Variation With Effective Oil Temperature. (Note false origin).

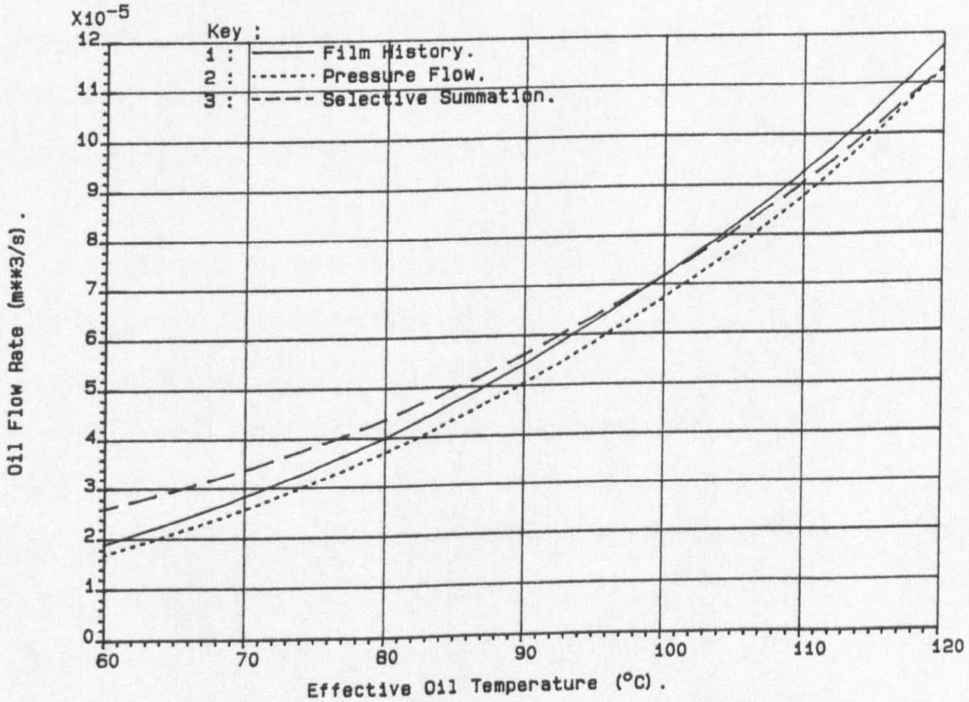

Figure 5.10 Oil Flow Rate Variation With Effective Oil Temperature. (Note false origin).

The close agreement between the film history solution and the simple expressions for the component power loss terms when applied to a journal centre orbit determined from the mobility curve fits of Booker (1965) was also noted in Section 5.2. In this section it was pointed out that the shear power loss reduction in the film history solution due to the cavitation region was almost balanced by the higher film shear rates for this solution (the orbit is based on the finite bearing mobility curve fits of Goenka (1984)). Hence, the two solutions are seen to agree well over the whole range of effective oil temperatures considered.

Close agreement of the oil flow rates predicted by several techniques is shown in Figure 5.10. This is particularly true of the film history and selective summation techniques which agree to within 5% at effective oil temperatures of 80°C and above. It should also be noted that at high effective oil temperatures the selective summation and pressure flow curves converge, since the steady flow (Q_s) is dominant over the translational flow (Q_T) in the selective summation technique and (Q_s) is only 4% smaller than the pressure flow (Q_p). This can be seen from Equations 3.28 and 3.29.

Hence, it can be seen that for the range of effective oil temperatures the power loss and oil flow rate can be determined quite accurately from simple expressions for the component parts. However, in a thermal solution the effective temperature is not known and for any two solution techniques to give the same power loss or oil flow rate, the effective temperature predicted by each solution must be close. Therefore, not only should the power loss and flow rate be predicted accurately, but the differences in the predictions should be such that the ratio of the power loss to oil flow rate for both techniques is close. This will give good agreement between the temperature rises through the bearing for each solution.

The effective oil temperature variation with inlet oil temperature is shown in Figure 5.11. The close agreement of the film history and selective summation is apparent and although the power loss and oil flow rates are generally greater for the simpler predictive techniques the resulting temperature rise is similar to that predicted by the film history solution. For curves 2 and 3 a fully flooded bearing was considered for the shear power loss calculations.

5.6 The Effect of Heat Transfer From The Bearing

In the previous section an adiabatic situation was considered in which all the heat generated within the bearing was considered to be carried away by the lubricant. However, in practical situations this may not be the case and some proportion (1-K) of the heat generated in the bearing will be transferred from the lubricating oil to the journal and bearing surfaces. Figure 5.12 shows the influence of the value of (K) on the effective oil temperature variation with the inlet oil temperature for the Ruston and Hornsby 6VEB-X Mk111 operating at an oil supply pressure of 276 kN/m^2 and a shaft rotational speed of 600 r.p.m. The flow rate determined by selective summation of (Q_s) and (Q_T) has been used for the equilibrium calculations.

It can be seen from Figure 5.12 that at an inlet temperature of 40°C the effective oil temperature can differ by

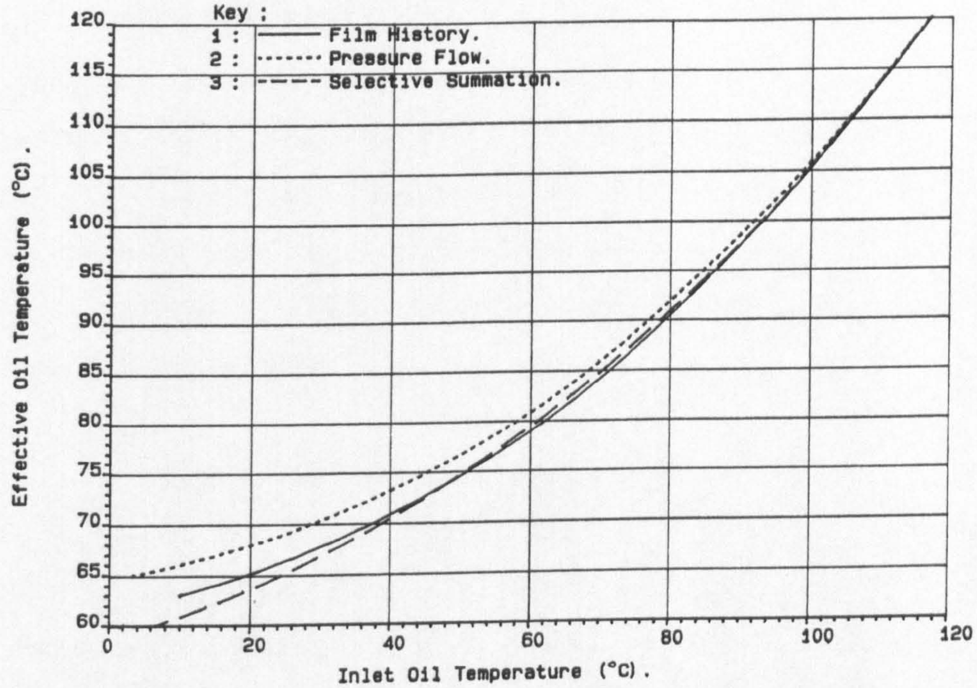

Figure 5.11 Effective Oil Temperature Variation With Inlet Oil Temperature. (Note false origin).

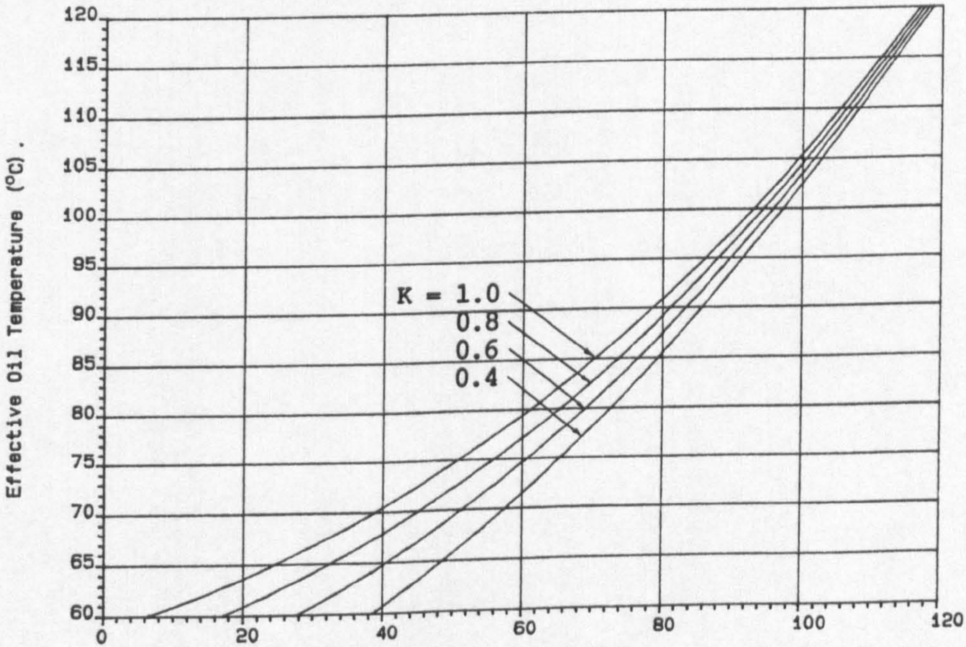

Figure 5.12 The Influence Of K On The Effective Oil Temperature Variation With Inlet Oil Temperature. (Note false origin).

10°C, for values of (K) in the range 0.4 to 1.0. For effective oil temperatures of 61°C and 71°C, the power losses and oil flow rates can be determined from Figures 5.9 and 5.10. It can be seen that the power losses at these two temperatures are about 2.4 kW and 1.8 kW which corresponds to a 27% decrease with increase in the effective temperature. Similarly, the oil flow rates are 26 x 10^{-6} m^3/s and 34 x 10^{-6} m^3/s at effective oil temperatures of 61°C and 71°C respectively. This represents a 31% increase in the oil flow rate with temperature.

However, the effective temperature differences are less influenced by the value of (K) at higher inlet oil temperatures, and at an inlet temperature of 120°C the predicted effective temperatures varies by only 2°C. This corresponds to differences in the power loss and oil flow rate predictions of only a few percent.

5.6 Conclusions

The oil flow rate and power loss prediction techniques, which were developed in Chapters 3 and 4, have been applied to the Ruston and Hornsby 6VEB-X Mk111. The influence of the oil supply pressure and shaft rotational speed on the bearing side leakage and power loss have been addressed, in addition to the analysis being extended to give a thermal solution. The main conclusion of the work are given below:

(1) All the author's preditive techniques gave good agreement with the previous published data. This was particularly true of the theoretical predictions of Jones (1982) and Paydas (1988). This indicates the valid assumption made by

the author that for full circumferential groove bearings the journal centre orbit is of secondary importance in the film history solution.

(2) The agreement of the author's preditive techniques gave reasonable agreement with the experimental data of Cooke (1983). The average discrepancy between the experimental data for the oil flow rate and the author's predictions being about 18%.

(3) For the Ruston and Hornsby 6VEB-X Mk111 big-end bearing it was found that the pressure flow equation and selective summation of the steady state flow (Q_s) and the translational flow (Q_T) gave good agreement with the author's film history solutions. This was particularly true of the selective summation technique where the cycle average oil flow rate differed by only 1.5% from the value predicted by the film history solution.

(4) It was found that the power loss predicted by the film history solution could be estimated to within about 7.5% by determining the journal centre orbit from short bearing theory and calculating the power loss from the equations for the component terms. (Equations 3.30, 3.31 and 3.32). A fully flooded bearing was assumed for the shear power loss calculation.

(5) The oil flow rate was seen to decrease with increase in the shaft rotational frequency. This was due to the journal centre orbiting the bearing centre at lower eccentricity ratios as the shaft rotational frequency was increased.

(6) There is no benefit in using the film history solution for the analysis of dynamically loaded full circumferentially grooved journal bearings based on the cases studied in this chapter. The trends in the oil flow rate and power loss as the input variables are changed can be predicted from simple expressions for the power loss and oil flow rate components. In addition, for typical engine bearings where the tolerances on the journal and bearing diameter can cause the diametral clearance to vary by a factor of 2, (between different bearings) the differences in the prediction techniques presented are negligible. The conclusions given above are based on a limited investigations and it should be noted that for other full circumferentially grooved bearings some of the points raised may not be true.

CHAPTER 6

CHAPTER 6

THE TEST ENGINE AND EXPERIMENTAL INVESTIGATION

6.1 Introduction

This chapter deals with the test engine, the instrumentation and the test procedure followed in the experimental part of this research work. No experimental data will be analysed in this chapter: this will be presented in Chapter 7.

The test engine for this part of the work was as single cylinder gasoline engine, the Ricardo Hydra. The engine has been developed, manufactured and marketed by Ricardo Consulting Engineers plc in recent years, with the specific intention that the engine would be used for research purposes. Several points which make the engine particularly suitable for the present experimental investigation will now be highlighted.

1. Since the engine has only one cylinder the problem of the load sharing between the two crankshaft (or main) bearings is greatly simplified. Each bearing is considered to take half the total externally applied gas and inertial loadings.

2. The Ricardo Hydra has a rigid bearing housing and crankcase since the engine was initially designed to work on a compression-ignition cycle.

3. Each main bearing is fixed in a rigid bearing housing which in turn fits into the crankcase. They may be easily removed and this facilitates their instrumentation.

Figure 6.1 shows a section through the Ricardo Hydra. The bearing which was instrumented was the front main bearing (cam shaft pulley side of the engine), since it was thought that problems of vibration and whirl associated with the flywheel could significantly influence the bearing loading. In the original design the front main bearing was used to supply oil to the crankshaft big-end bearing, and therefore the crankshaft was modified and oil was supplied from the rear main bearing. Experimental measurements of the following parameters were made:-

1. Inlet oil temperature and pressure
2. Crankshaft rotational frequency and engine torque
3. Outlet oil temperature and thirty-two bearing temperatures
4. Oil flow rate through the bearing
5. Cylinder gas pressure variation with crank angle
6. Journal centre orbit

Much of the instrumentation was of a standard nature and will only be described briefly. However, features of the instrumentation specific to the present work will be described in detail. In particular, this refers to the instrumentation of the bearing for temperature measurements and the journal centre orbit determination. Figures 6.2 and 6.3 show the bearing housing instrumentation. The position of the proximity transducers is shown relative to the bearing and the outlet from the thermocouples is clearly visible. Figure 6.2 also shows the engine crankshaft. The remainder of this chapter will be set aside to describe the important modifications and instrumentation of the engine to allow the measurement of the above variables.

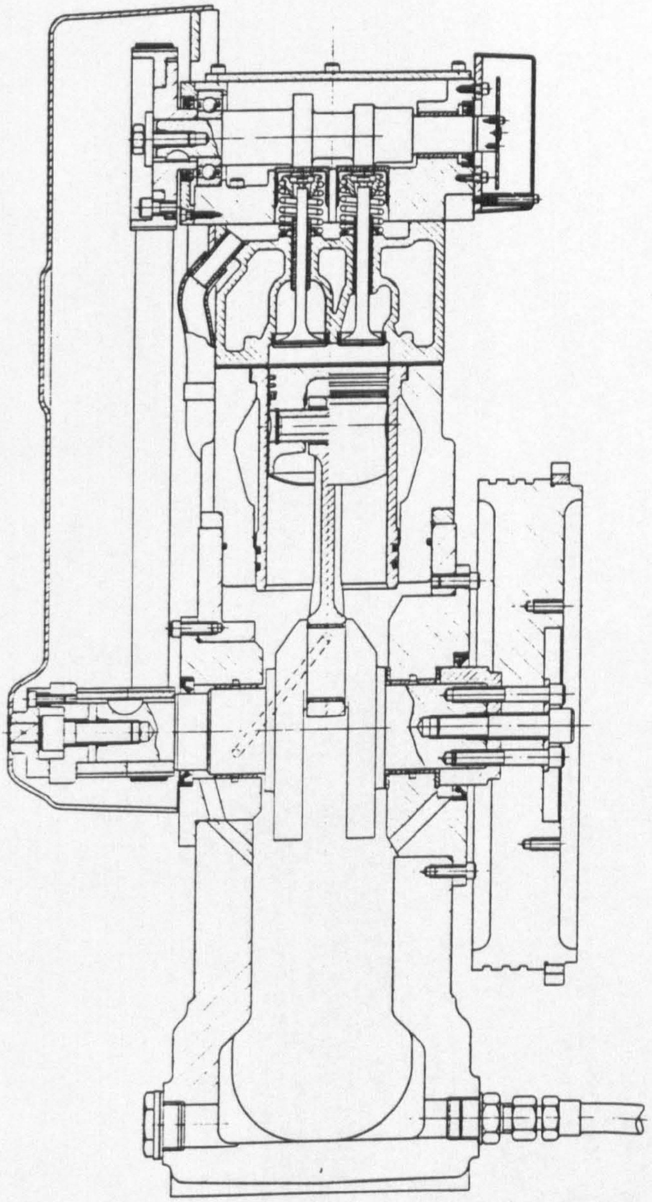

Figure 6.1 Section Of The Ricardo Hydra

VOLUME CONTAINS CLEAR OVERLAYS

OVERLAYS HAVE
BEEN SCANNED
SEPERATELY
AND
THEN AGAIN OVER
THE RELEVANT PAGE

Proximity Transducers

Thermocouple Outputs

(a) Crankshaft

Journal Bearing

Crankshaft Oil Feed Hole

(b) Bearing Housing

Figure 6.2 Test Engine Crankshaft and Bearing Housing

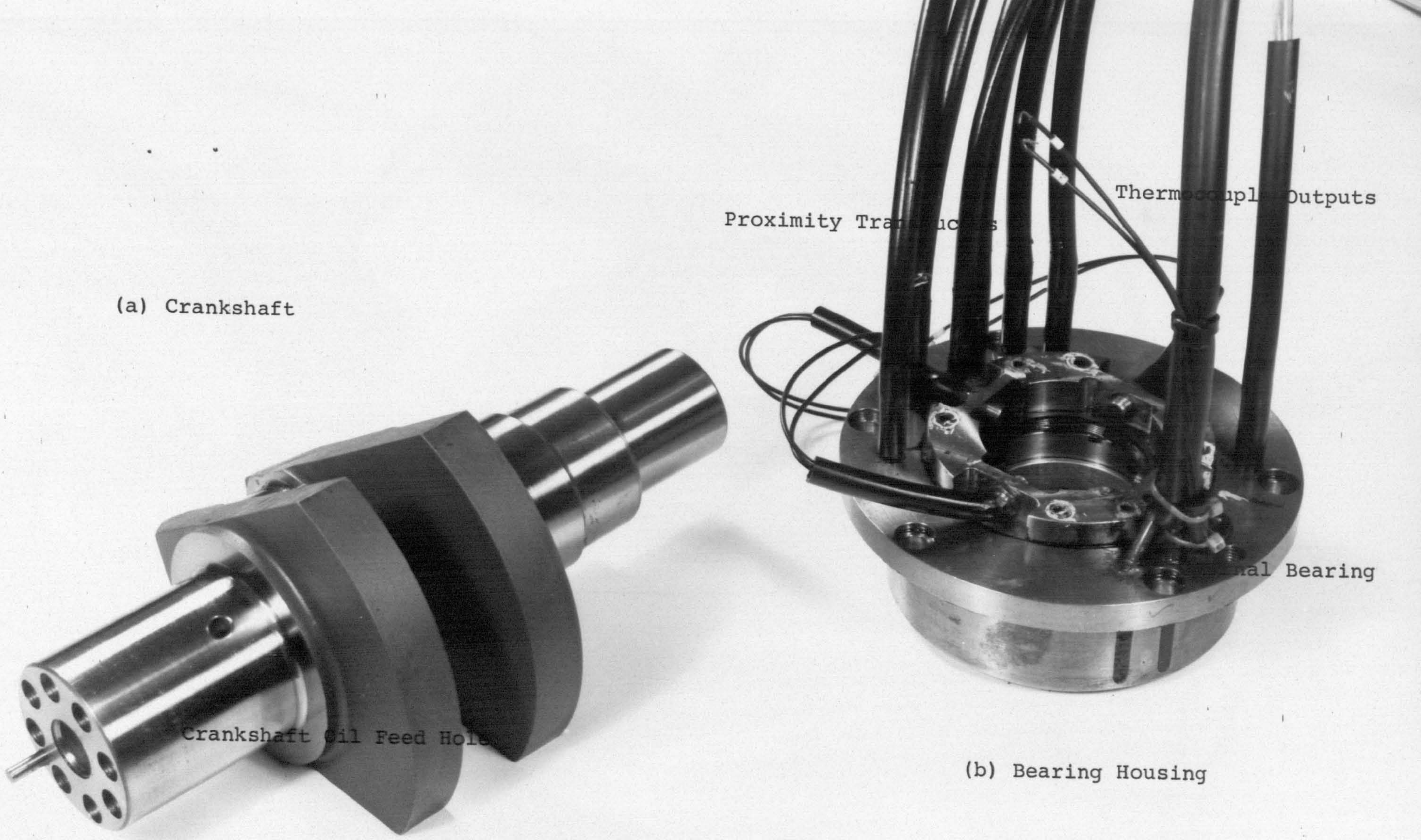

(a) Crankshaft

(b) Bearing Housing

Figure 6.2 Test Engine Crankshaft and Bearing Housing

Journal Bearing

Thermocouple Output

Proximity Transducers

Figure 6.3 Journal Bearing Housing and Instrumentation

Figure 6.3 Journal Bearing Housing and Instrumentation

6.2 Temperature Measurement

All the temperature measurements were made using K-type (Nickel-Chromium/Nickel-Aluminium) thermocouples. Figures 6.4 and 6.5 show the axial and angular positions of the thermocouples. In addition to a thermocouple fixed in the oil drain hole to measure the outlet/drain oil temperatures, eight rows of four thermocouples were positioned so that the weld beads lay 0.5 mm below the bearing surface. The thermocouples were glued firmly in place in radial holes machined into the bearing and then passed out of the bearing housing along axially milled grooves. The angular position of these grooves is shown in Figure 6.5.

The thermocouples were designated by two numbers. The first was the angular position (1-8) and the second was the axial position (1-4). It can be seen from Figure 6.4 that the axial positions (2) and (4) were equally spaced either side of the central groove. The reasons for this were as follows:-

1. A qualitative assessment as to the degree of misalignment in the bearing (being reflected as a difference in the temperature of the two bearing lands) was possible. In addition, thermocouple (01) gave the outlet oil temperature from the right hand bearing land, and a qualitative assessment of the bearing misalignment when compared with the temperature at (0).

2. It was not known whether temperature differences between the two bearing lands would be observed due to heat transfer from the cylinder.

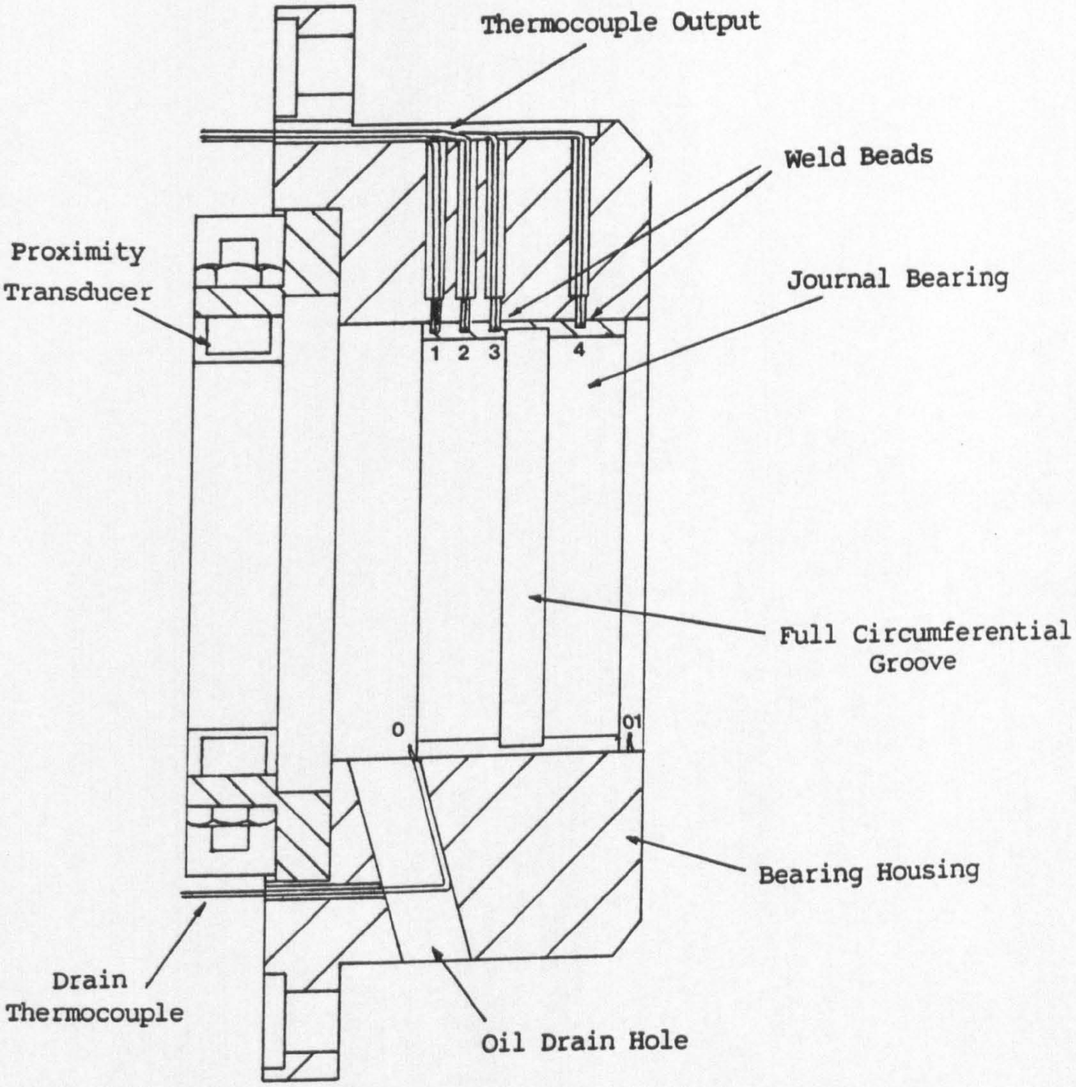

Figure 6.4 Position Of Thermocouples And Proximity Transducers Relative To The Bearing.

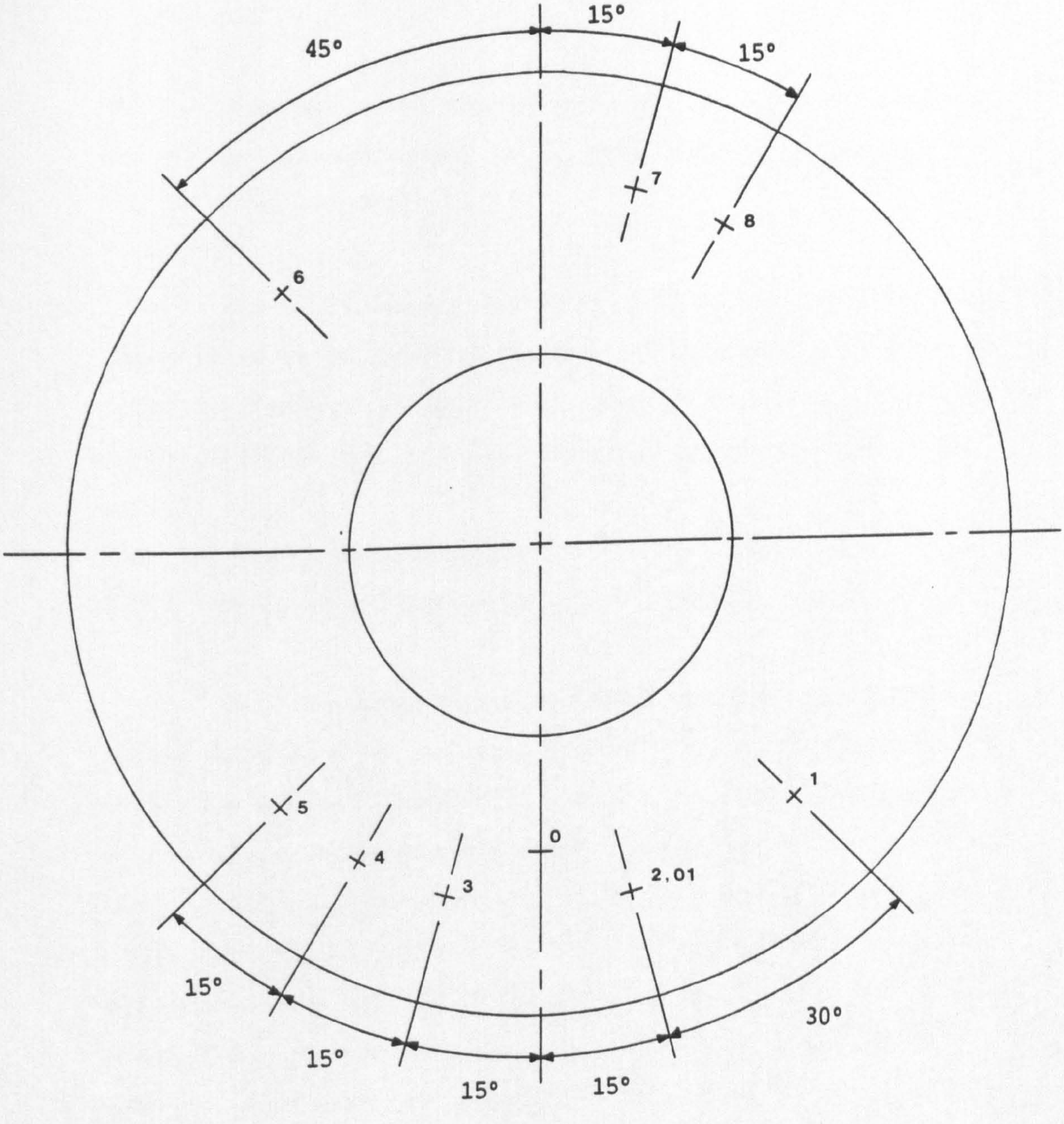

Figure 6.5 Angular Positions Of The Thermocouples In The Bearing Housing

3. Duplication of thermocouples was provided in case any significant number in the left hand bearing land (Figure 6.4) were faulty.

The thermocouples were connected via an electronic cold junction to an IBM personal computer and printer and were logged using the computer function keys. The inlet oil temperature was connected to the test cell instrumentation and recorded manually.

6.3 The Journal Orbit Measurement

6.3.1 The Choice and Positioning of the Proximity Transducers

Four Vibrometer inductive proximity transducers (Catalogue Number TW8-2/A) were used to determine the journal centre orbit within the bearing. These were mounted in two half bridge push-pull arrangements, axially relative to the bearing as shown in Figure 6.4 and angularly as shown in Figure 6.6. (The transducer arrangement is also shown in Figures 6.2 and 6.3). A specially designed holder was made and the bearing housing had a recess machined into it to take the holder, the two parts were secured using cap head socket screws. In addition, the crankshaft was modified at this position so that the transducers would not be facing a change in the crankshaft diameter. The step was machined back and a collar was fitted onto the crankshaft and machined to the correct diameter.

The transducers selected for the journal centre orbit determination worked on an 8kHz carrier frequency and had a dynamic response time of 1.5 kHz. As with capacitive transducers they are sensitive to temperature changes and were therefore used in a push pull arrangement. In such arrangements the sensitivity and

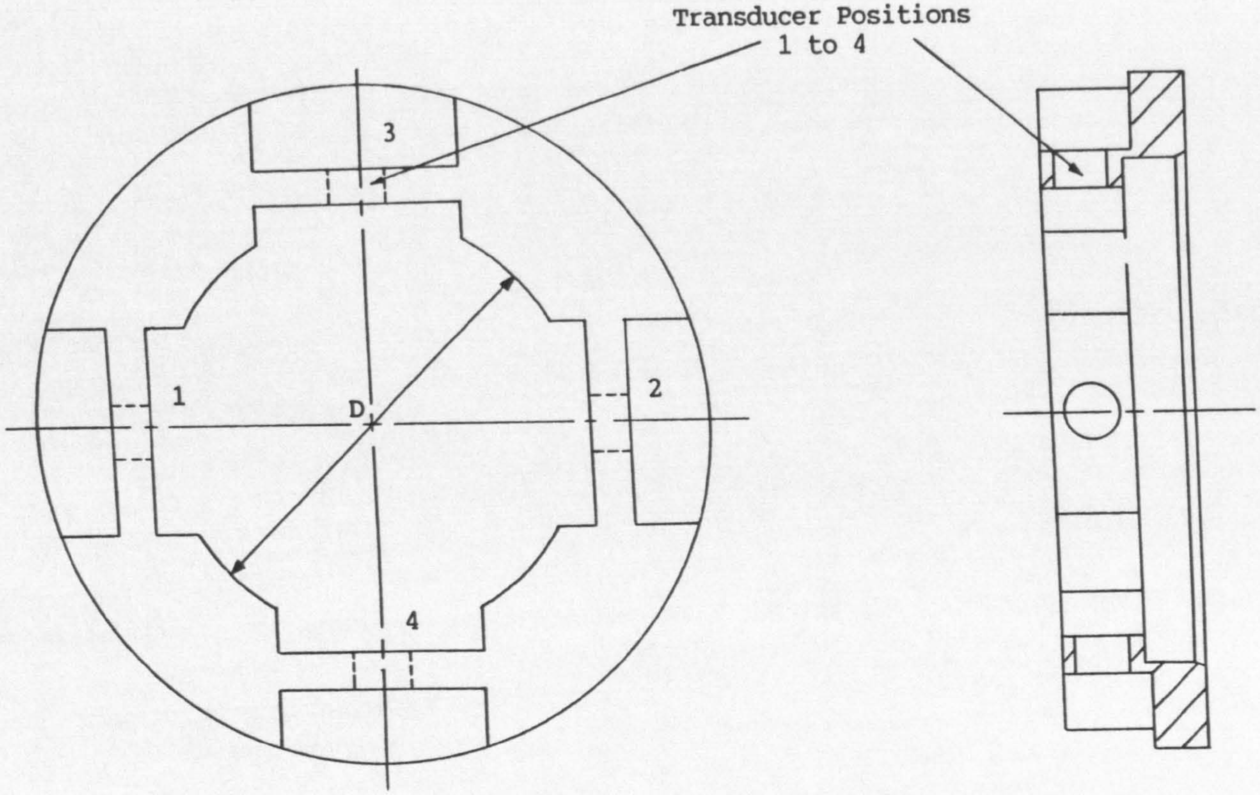

Figure 6.6 Proximity Transducer Holder

linearity is approximately doubled and the readings influenced by differences in the transducer temperatures.

Since two matched pairs of Vibrometer inductance proximity transducers and their amplifiers were available, and since no significant temperature differences between the transducers was expected, these transducers were considered suitable for the present work.

6.3.2 The Calibration of the Proximity Transducer

The proximity transducers were calibrated using a numerically controlled milling machine. This was comprised of a Hayes milling machine and a Vickers UMAC7 controller. The three axis slides were actuated by hydraulic rams controlled by electro-hydraulic servo valves and the position and velocity feed-back was achieved via inductosyns fitted to the three machining table axes. This allowed the table positions to be measured to 1μm although such fine movements of the table could not be achieved.

The transducers and holder (Figure 6.6) were clamped to the machine table and a circular stepped metal calibration bar secured in the machine head. The table was then raised and positioned so that the bar and transducer holder mated. This was achieved using the internal radius of Figure 6.6 (denoted by D) and the corresponding maximum diameter of the calibration bar. This ensured that the transducer holder and bar were co-axial allowing for the machining tolerances of the mating parts. The machine table was then lowered so that the transducers were facing the portion of the bar of nominally the same diameter as the engine crankshaft and the transducers were then set at a distance of 1mm from the bar surface. This was achieved using slip gauges. The calibration of each pair of transducers was the same and was achieved by moving the milling machine table and recording the transducer output. This was done for a range of table movement from about - 80 to 80 μm and the calibration curves are shown in Appendix 3.

Since the distances being measured by the transducers are so small the calibration curves are seen to give a linear variation of output with displacement. This was advantageous in case the amplifier had to be zeroed during the tests, and in this case the gradient of the calibration curves would be important. This was found to be 0.4300 mV/μm for transducers 1 and 2 and 0.4146 mV/μm for transducers 3 and 4. Correlation coefficients higher than 0.999 were obtained for the two calibration curves, indicating the linearity of the proximity transducers when measuring such small displacements.

The calibration bar was made from the same material as the crankshaft. This was to minimize errors in the experimental readings due to differences in the permeability of the materials. However, even if this had not been done the readings would only have been minimally influenced due to the fairly large air gaps between the transducers and shaft surface.

During the tests the output from the transducers were attached to the (x) and (y) plates of a cathode ray oscilloscope so that the journal orbit could be monitored as the tests were proceeding. The journal orbit was photographically recorded in addition to the data being logged by a Ricardo High Speed Data Acquistion (HSDA) system.

6.4 The Oil Supply Circuit

Figure 6.7 shows a schematic representation of the oil supply from the engine sump to the bearing. The instrumentation which was added for the purpose of the experimental investigation has been enclosed by a dotted line.

The oil supply pressure to the bearing was set by the position of the manually operated valve and was measured using a dial gauge. To safeguard against closing the valve too much and hence starving the bearing of oil, a low pressure cut out was positioned in the supply line to the bearing. This was set at 0.1013 MN/m^2 (15 psi). The valve could, therefore, be positioned to give a pressure drop across the bearing of between 0.1013 MN/m^2 (15 psi) and about 0.405MN/m^2 (60 psi) (fully open valve). However, while the pressure gauge gave a constant, and presumably average reading throughout the time required for each test point, the bearing supply pressure could have been changing by several percent.

Since the journal eccentricity was changing through the engine cycle, so will the bearing resistance to oil flow and pressure drop across this part of the oil system. From the pressure flow equation the resistance of the bearing can be defined as,

$$\frac{P_s}{Q_p} = 30.58 \frac{b}{d} \frac{\eta}{{c_d}^3} \frac{1}{(1.5\varepsilon^2 + 1)} \qquad (6.1)$$

and the influence of the eccentricity ratio (ε) is apparent. (This is analogous to the voltage drop, current flow and resistance of an electric circuit). Using typical extremes of eccentricity ratio, obtained from a theoretical journal orbit prediction using the mobility equations of Booker (1965) (Chapter 3), the resistance of

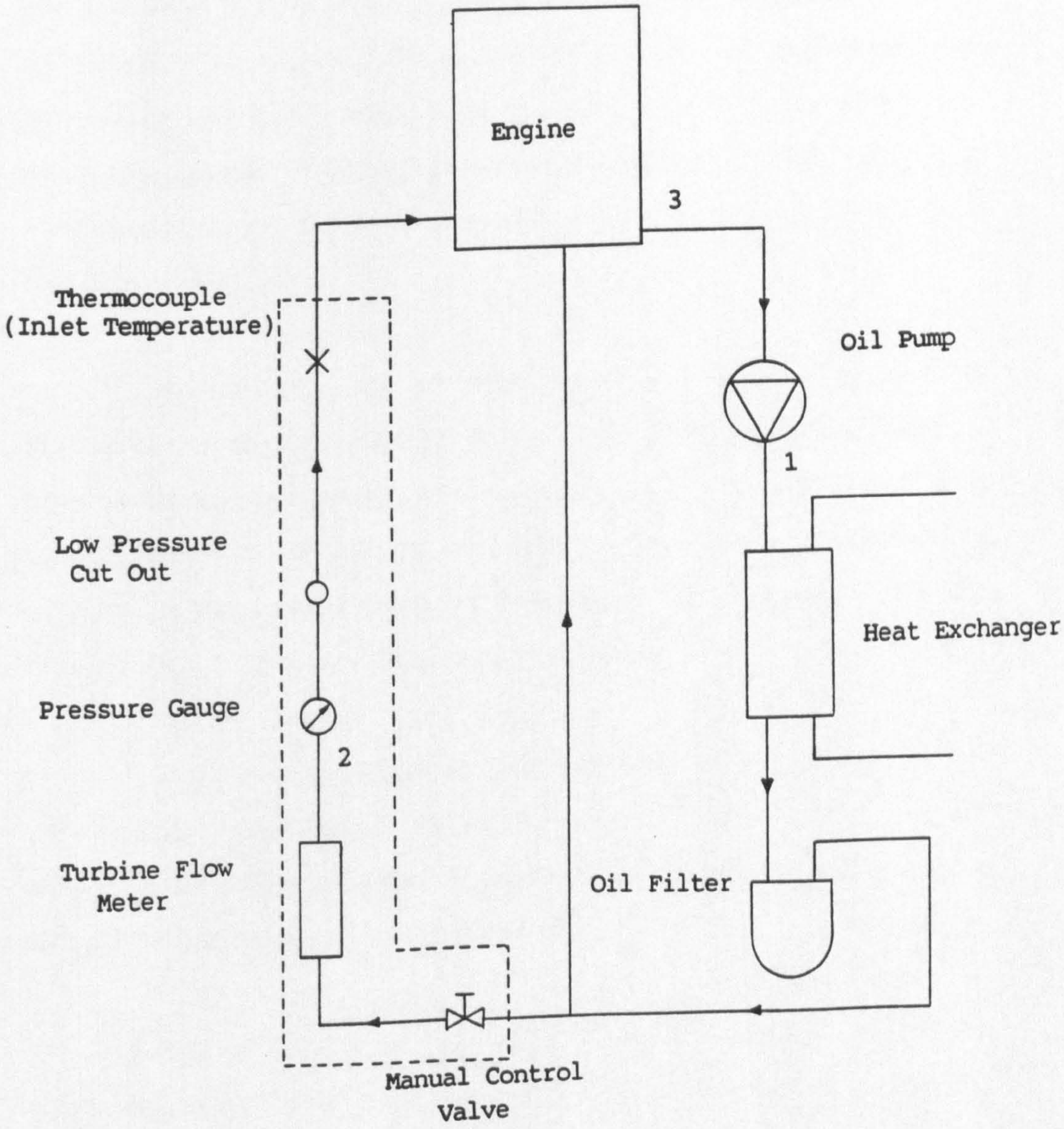

Figure 6.7 Schematic Representation Of The Oil Supply Circuit

the bearing could vary by as much as 30% through the engine cycle. For the case in which the pressure drops across positions 1 and 2, and 2 and 3 in Figure 6.7 are nominally equal (as determined from the steady pressure reading from the dial gauge), this corresponded to a fluctuation in supply pressure of about 6%. This value will vary depending on the effective resistances between 1 and 2, and 2 and 3 in Figure 6.7.

No variations in the bearing supply pressure was observed during the tests, presumably due to the relatively slow response time of the pressure gauge. In any subsequent tests, this variation would provide an interesting investigation and could be achieved by using a piezo-electric pressure transducer. The average effective bearing supply pressure would still be measured using a dial gauge.

The inlet oil temperature to the bearing was monitored by a thermocouple, the output from which was displayed on the engine control console and recorded manually. This was set to the desired value using the oil and water heaters.

The oil flow rate was measured using a turbine flow meter which was calibrated for a range of oil temperatures. During calibration the oil supply to the bearing was disconnected and the flow meter reading and time taken for a measured volume of oil to flow was noted. Between 5 and 15 readings were taken during the calibration of each point, since small oscillations in the digital output were observed. In such cases the mean values was taken as the actual meter reading.

However, the flow meter reading was generally steady during calibration, with oscillations in the digital meter output corresponding to inaccuracies in the subsequent calibration curves of about 1%. In addition, several points gave oscillations corresponding to errors of about 2% and a very small number of points gave possible localized inaccuracies in the calibration curves of 4%.

6.5 Cylinder Gas Pressure Measurement

The cylinder gas pressure were an important parameter to measure since they were used, in part, to determine the bearing loading. A pressure probe was screwed firmly into a tapped hole drilled through the cylinder head, and the cylinder pressure was recorded every 1° of crankshaft rotation, and averaged over 250 cycles using a Ricardo HSDA system. An encoder was attached to the crankshaft to trigger the HSDA unit. The output, together with the masses of the piston assembly, connecting rod, crankshaft and balancing weights were then input to Ricardo Consulting Engineers plc software to determine the cylinder pressure/volume (PV) and bearing polar load diagrams. Tables of bearing load variations with crankshaft rotation are given in Apendix 4.

Figure 6.8 shows a (PV) diagram for the Ricardo Hydra. This is for a crankshaft rotational frequency, engine torque, spark advance and percentage of carbon monoxide in the exhaust gases of 3500 rpm (58.3 Hz), 15 Nm, 22.5° and 1.42% respectively.

It can be seen from Figure 6.8 that an acoustic shock occurs at the start of the compression stroke and that the compression stroke was not adiabatic. This was indicated by the curved compression line. During the test program the pressure probe was cleaned and checked for any loose electrical connections which

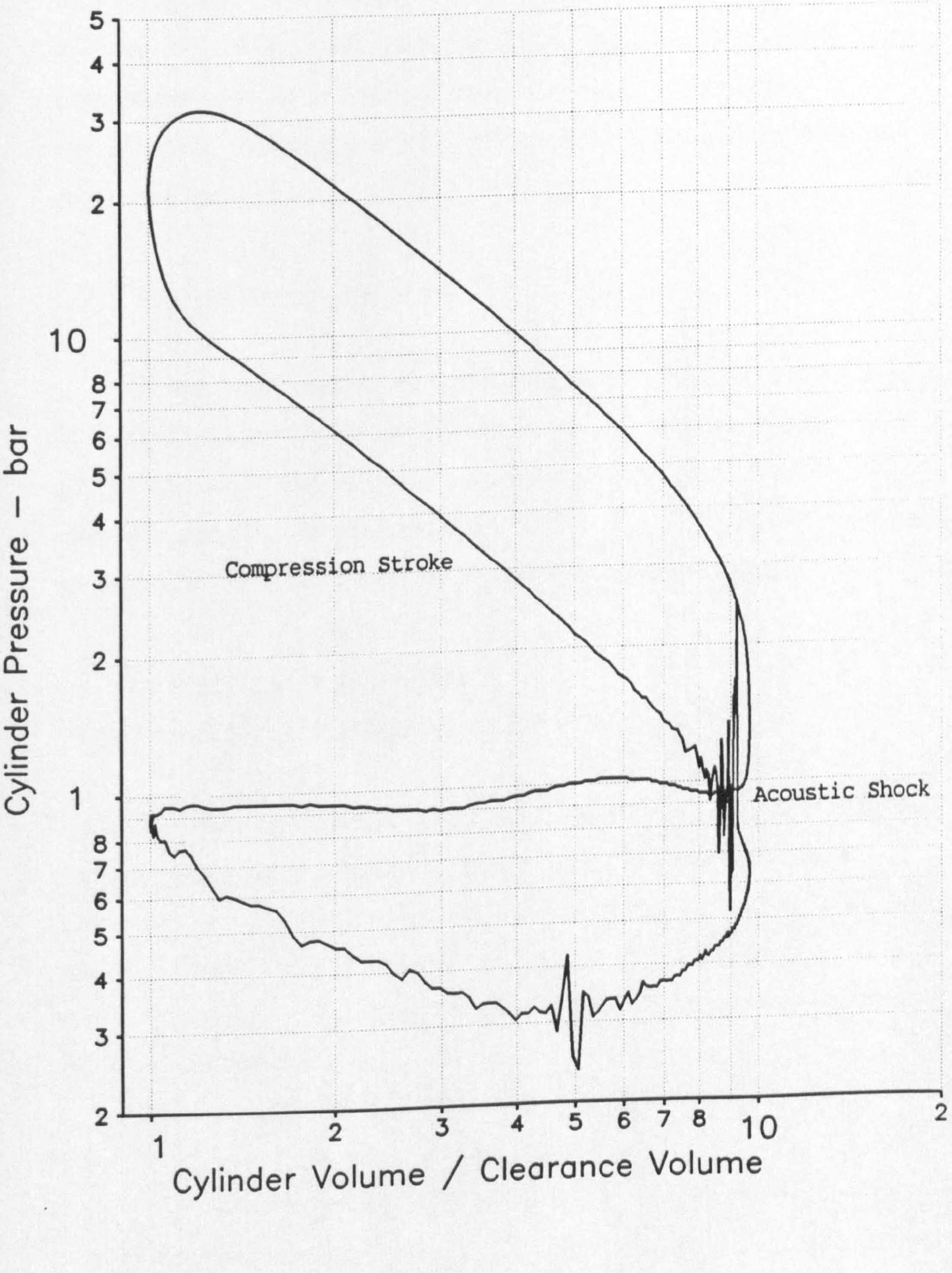

Figure 6.8 Typical P-V Diagram For the Ricardo Hydra
(3500 rpm, 15 Nm, Spark Advance 22.5°)

may have caused these conditions. However, no faulty connections were found and the cleaning of the probe did not affect the (PV) diagram. It was therefore concluded that the non-adiabatic compression was due to several factors, including heat transfer from the cylinder, turbulence within the combustion gases and gas leakage past the piston rings.

6.6 Additional Instrumentation

The test engine was also instrumented to take readings of several important engine management parameters. These included the spark advance, engine torque, crankshaft rotational frequency, exhaust pressure and percentage of carbon monoxide in the exhaust gases. These were monitored on the engine control console.

6.7 The Experimental Investigation

6.7.1 Scope of the Experimental Investigation

During the engine tests the influence of the oil supply pressure, shaft rotational frequency and the effective oil temperature/viscosity on the oil flow rate were investigated. During the tests the effective oil temperature was taken as being equal to the outlet oil temperature and specific tests were carried out to investigate:-

(i) The influence of the supply pressure an oil flow rate for constant crankshaft rotational frequency and outlet oil temperature.

(ii) The effect of crankshaft rotational frequency on the oil flow rate for a constant oil supply pressure and outlet oil temperature.

(iii) Variation of outlet temperature with crankshaft rotational frequency for a constant oil supply pressure and inlet oil temperature. This enabled a comparison of the overall thermal balance of the bearing and the temperature rise of the oil to be compared with theoretical predictions.

The experimental data will be analysed and compared with theoretical predictions in Chapter 7.

Two oils were used during the tests, these were Shell Rotella X 30 and Shell Rotella X 15W/40. Some important physical characteristics are given in Table 6.1.

Oil Type	Density at 15°C (Kg/m^3)	Kinematic Viscosity (cSt)	
		40°C	100°C
Rotella X 30	891	90.1	10.8
Rotella X 15W/40	886	99.6	13.8

Table 6.1 Important physical characteristics of the lubricating oils

6.7.2 Thermal Equilibrium of the Test Engine

The engine took between one and two hours to reach thermal equilibrium from a cold start. This time was dependent on the temperature the oil had to be raised to before experimental readings were taken. In addition, the time required for each set of readings depended on the time required for the bearing and oil temperatures to reach equilibrium after altering one of the test variables. This time could range from 10 to 35 minutes and was dependent on the particular test variable altered.

Generally speaking, if the oil outlet temperature and the oil supply pressure were kept constant and the shaft rotational speed was varied, the time required to reach equilibrium would be long. This was because the oil inlet temperature would have to be changed to give the required overall thermal balance for the bearing. This in turn required the total oil temperatuare in the sump and the associated engine temperatures to be altered. Hence, a large heat source or sink had to be influenced giving a high time constant for the system. If, however, the inlet oil temperature and supply pressure were kept constant and the influence of the shaft rotational speed on the outlet oil temperature was important, then the time to reach equilibrium would be small. This is because the change in power loss due to the change in shaft rotational speed had an instantaneous effect on the outlet oil temperature, but only a slight effect on the total energy of the system.

These two cases represent two possible extremes. The time required to reach equilibrium was also dependent on the temperature of the engine test cell. Low oil temperatures were difficult to obtain when the engine had been running for several hours and the test cell temperature was high. Similarly, high temperatures were difficult to obtain when the engine had just been started. Therefore, it was often difficult to obtain a significant number of points from one test run. This was particularly true of high oil temperatures with low shaft rotational speeds and low oil temperatures with high shaft rotational speeds. Hence, in determining trends over the whole engine working conditions it was necessary to compare data from different tests. For this reason, the spark advance, engine torque and percentage carbon monoxide in the exhaust gas was kept constant at each specific crankshaft frequency, ensuring that any subsequent cross plotting or comparison of data from different tests had the same load cycle variations with crankshaft frequency.

6.7.3 Test Data Repeatability

The repeatability of the test data was also important, both from a point of view of obtaining high quality data showing the correct trends of dependent variables with independent variables, and also if data from different tests was used to determine trends in properties over the whole engine working regime. If this was not the case, discontinuities in the trends could be obtained when the test data was concatenated. However, the experimental data showed a good repeatability which was evidenced by the smoothness of the data and the close agreement of any overlapping data points. This was true of the oil flow rate and the inlet and outlet oil temperatures.

The repeatability of the data gave an indication of the quality of the experimental data obtained. This will be re-emphasized when the data is analysed in Chapter 7.

6.8 Conclusions

The instrumentation of the test engine and the scope of the investigation has been described. It has been pointed out that difficulties were encountered in obtaining high oil temperatures at low shaft speeds and low oil temperatures at high shaft speeds. This significantly reduced the range of test conditons which could be achieved. In addition, the test cell temperature could also influence the range and ease with which test conditions could be obtained. In any subsequent tests it would be advisable to use a more powerful oil heater and cooler to give a larger operating oil temperature range.

Several inaccuracies involving the experimental readings have been pointed out. These include:-

1. The bearing supply pressure could vary by as much as 6% due to the journal centre eccentricity effect on the bearing resistance to flow. This point was not investigated during the tests, but is an inherent feature of such oil supply systems.

2. Small oscillations in the flow meter reading could introduce localized inaccuracies in the calibration curves of up to 4% (± 2%). In addition, such inaccuracies could also be introduced into the actual test data due to oscillations during the tests. This could lead to ± 4% error in the flow rate measurement.

3. The repeatability of the readings was good. The oscillations in the oil supply pressure measurement (1) were not random and would therefore not affect the repeatability of the flow rate measurements. However, the flow rate measurement given in (2) are random and will influence the repeatability.

In view of the points raised above, it must be emphasized that the test apparatus was adequate for the purpose of the experimental research carried out in the present work. Readings of the oil flow rate could be considered accurate to within about ±2% and a significant amount of reliable data has been collected. The oscillations in the oil supply pressure which were discussed in Section 6.4 were relatively small and the supply pressure given by the pressure dial gauge was considered to give an effective oil supply pressure for the whole engine cycle.

CHAPTER 7

CHAPTER SEVEN

ANALYSIS AND DISCUSSION OF THE EXPERIMENTAL DATA

7.1 Introduction

An extensive amount of experimental data has been collected for the Ricardo Hydra engine which was described in Chapter 6. The effect of the oil supply pressure and journal rotational frequency on the bearing side leakage has been investigated and in this chapter the experimental data will be presented and compared with the author's theoretical predictions. However, only a limited analysis of the experimental data will be carried out and it should be noted that it may take additional study to draw out all the important features of the experimental results.

Some important specifications for the Ricardo Hydra front main bearing are given below:

Width of one bearing land	11.28 mm
Shaft diameter	57.139 mm
Diametral clearance	88 μm
Engine speed	1500 rpm (25Hz)-6000rpm (100Hz)
Lubricant supply pressure	137.9 kN/m^2 (20 psi) - 344.7 kN/m^2 (50 psi)

The variation of the oil specific heat with temperature is given in Table 7.1. These values were obtained from a private communciation with Bell (1988).

Oil Temperature (T) (°C)	Oil Specific Heat (c_p) kJ/kg°C
10.0	1.841
37.8	1.925
93.3	2.134
121.1	2.218

Table 7.1 Oil Specific Heat Variation with Temperature

It was found that the data given in Table 7.1 could be approximated by the straight line;

$$c_p = 1804 + 3.42\ T \qquad (7.1)$$

where (T) is the oil temperature in (°C). This relationship was applicable to both oils used.

Very full details of the bearing load variation with crankshaft angle, for several engine speeds, are given in Appendix 4.

In this chapter results for the tests where the lubrication was Shell Rotella X30 will be presented. Additional data for tests using Shell Rotella X15W40 are presented in Appendix 5.

7.2 The Temperature Variation Within the Test Bearing

Table 7.2 shows a set of bearing temperatures. These were obtained for an inlet oil temperature of 54°C, an outlet oil temperature of 80°C, a journal rotational frequency of 3500 rpm (58.3 Hz) and an oil supply pressure of 241.3kN/m^2 (35 psi).

Angular Thermocouple	Axial Thermocouple			
	1	2	3	4
1	79.5	79.9	78.7	78.5
2	77.6	76.6	76.6	78.1
3	75.3	75.6	74.6	76.4
4	74.9	75.0	73.9	75.1
5	73.3	73.7	72.5	73.9
6	76.4	76.0	74.7	75.0
7	82.5	83.3	81.0	79.1
8	81.5	79.3	80.3	77.8
01	76.7			

Table 7.2 Temperature Variation Through the Bearing

The thermocouple numbering system is detailed in Chapter 6 (Figures. 6.4 and 6.5).

Several important points, which were applicable to most of the experimental data collected, will be discussed in relation to the temperature distribution given in this table.

1. The temperature range within the bearing was 10.8°C, compared to a temperature rise in the oil of 26°C. Hence, it can be seen that the mixing of the recirculating and inlet flows is important in determining the outlet oil temperature.

2. During the tests the bearing temperatures were seen to respond almost instantaneously to a change in the oil outlet temperature.

3. The temperatures at thermocouple angular positions (7) and (8) were always the highest, and were the only positions at which the bearing was hotter than the outlet oil temperature. The cooler bearing temperatures were usually diametrically opposite, at thermcouple angular positions (3), (4) or (5). Of these, the thermocouples at angular position (5) were the coolest.

4. The thermocouples at axial position (4) were usually within about 1-1.5°C of those at axial position (2) which were at the same angular positions. However, the difference was greater at angular position (7) where it can be seen from Table 7.2 that a difference of 4.2°C was observed.

While the trends described above were applicable to the majority of the data collected, it must be pointed out that for such small differences in the bearing temperature, the radial positional tolerance of the thermocouple weld bead could have had a significant effect on the measured temperature.

7.3 The Determination of an Effective Oil Temperature

An effective oil temperature may be defined as:- a fixed temperature, throughout the oil film, which facilitates satisfactory predictions of one or more of the performance characteristics.

However, in order that the value chosen has any credibility, it must bear some physical relationship to the actual measured oil and bearing temperatures. In view of the conclusions given in Section 7.2, it would seem reasonable to assume that this temperature was close to the outlet oil temperature. However, as much of the bearing was cooler than this (up to 7.5°C at some positions), three suggested effective oil temperatures were defined. These were:-

1. The outlet oil temperature. This was essentially an average of the actual oil temperatures and was denoted by (T_o).

2. An average of the thermocouple temperatures of angular positions (1), (5), (6) and (8). These were positioned almost orthogonally to each other, and this temperature provided an average of the highest (8) and lowest (5) bearing temperatures, with an additional weighting towards the middle of the range of bearing temperatures. This was denoted by (T_{av}).

3. An average of the temperatures of the thermocouples at angular position (5). This gave an effective temperature which was biased towards the lower temperatures within the bearing. This was denoted by (T_5)

The influence of the choice of the effective temperature will be discussed in the next section.

7.4 The Influence of the Effective Oil Temperature on the Author's Theoretical Oil Flow Predictions

Several sets of data have been chosen to assess the suitability of the effective oil temperatures given above. For reasons of simplicity, and without any prior knowledge of the expected bearing and oil temperatures, the effective temperature during tests was considered to be equal to the outlet oil temperature. Hence, for the data presented below, the outlet oil temperature was kept constant for each test.

7.4.1 The Oil Flow Rate Variation with Supply Pressure

Figures 7.1, 7.2, 7.3 and 7.4 give a comparison of the oil flow rates predicted using the author's analysis techniques with the experimentally determined oil flow rates. In Figures 7.1 and 7.2 the influence of the three possible effective oil temperatures (defined in Section 7.3 and given in Appendix 5) on the author's film history predictions is also shown.

For an outlet oil temperature of 100°C and a shaft frequency of 1500 rpm (25 Hz) the oil temperature rise through the bearing was only about 2°C. Hence, in this case the author's predictions are based on an effective oil temperature which is equal to the outlet oil temperature.

From Figures 7.1 and 7.2, it can be seen that:

1. For the low journal speed case (1500 rpm) the agreement between the experimentally determined oil flow rate and that predicted by the author's film history solution is excellent. Since the oil temperature rise through the bearing is only about 2°C, the outlet oil temperature gives a good estimate of the effective oil temperature.

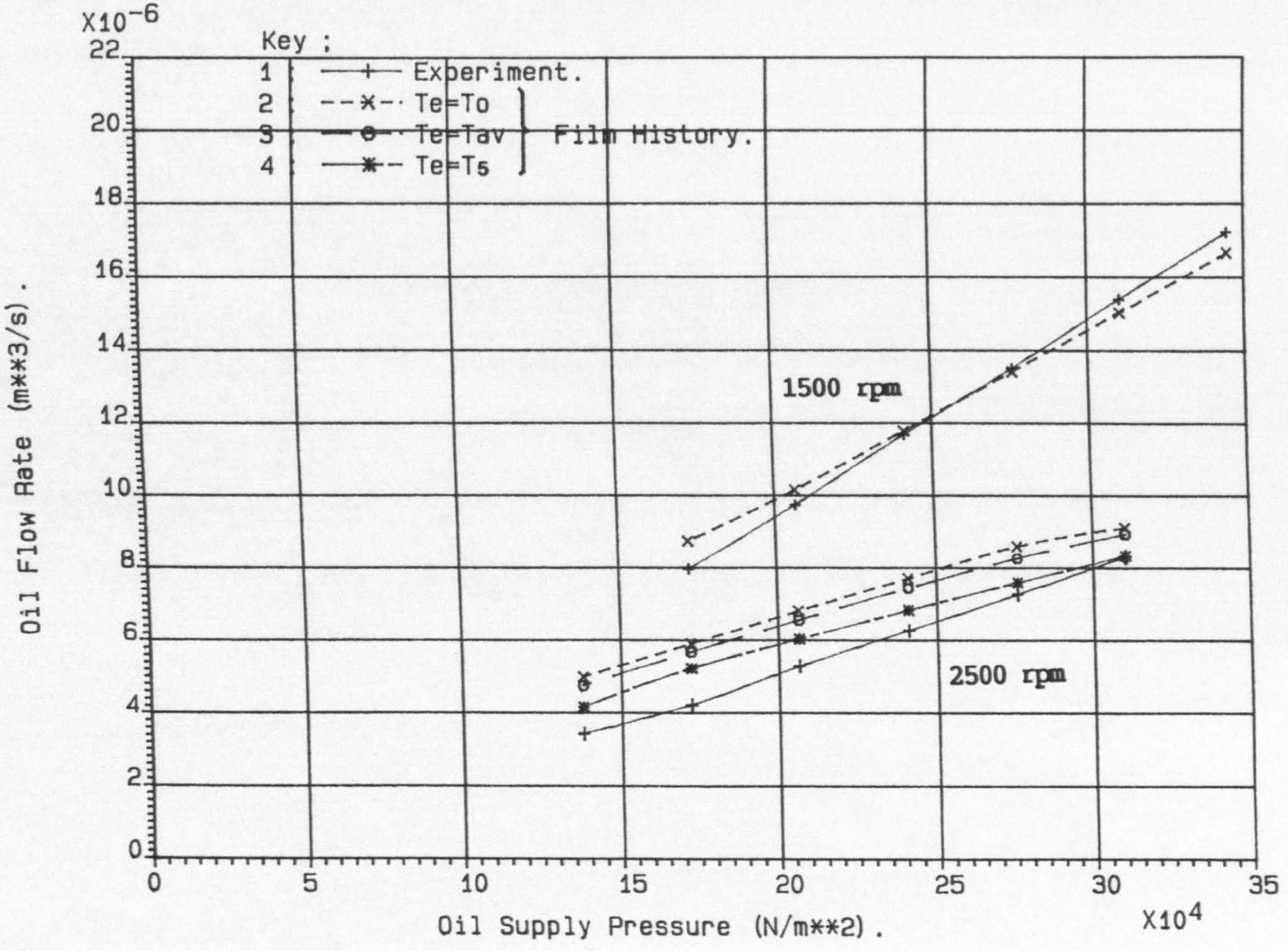

Figure 7.1 Oil Flow Rate Variation With Supply Pressure For Three Effective Oil Temperatures.

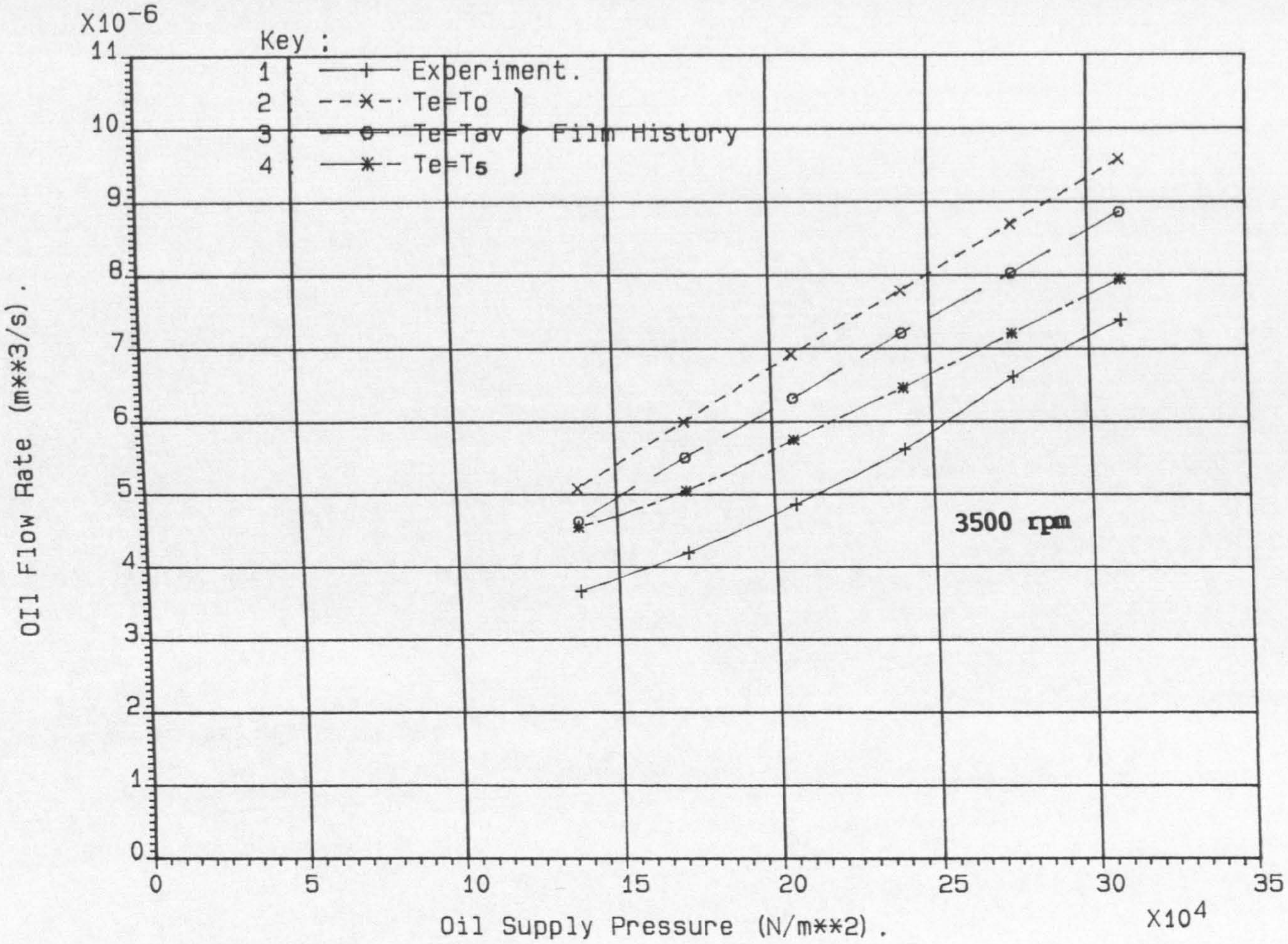

Figure 7.2 Oil Flow Rate Variation With Supply Pressure For Three Effective Oil Temperatures.

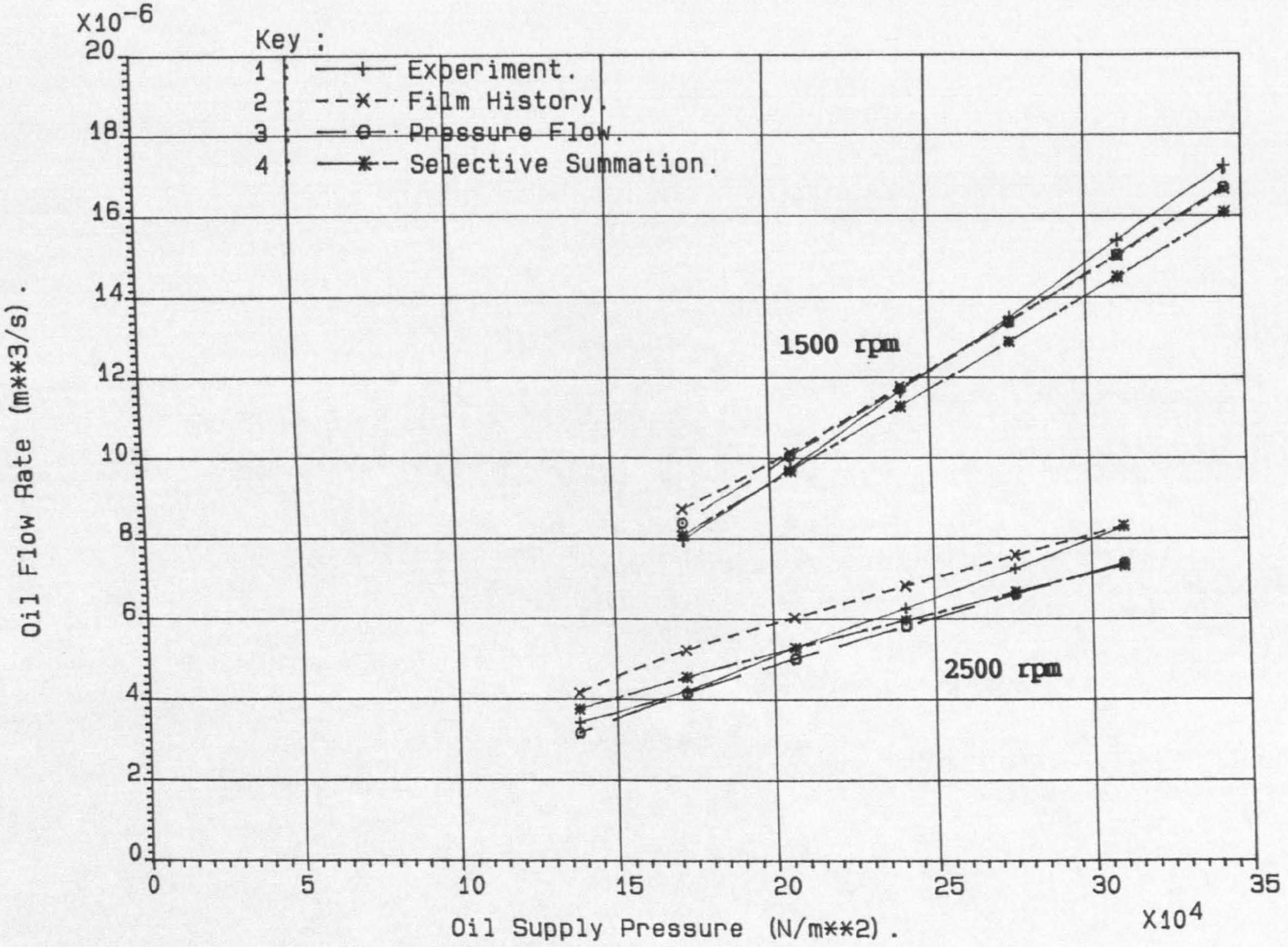

Figure 7.3 Oil Flow Rate Variation With Supply Pressure.
(Comparison Of Author's Predictions With Experimental Data).

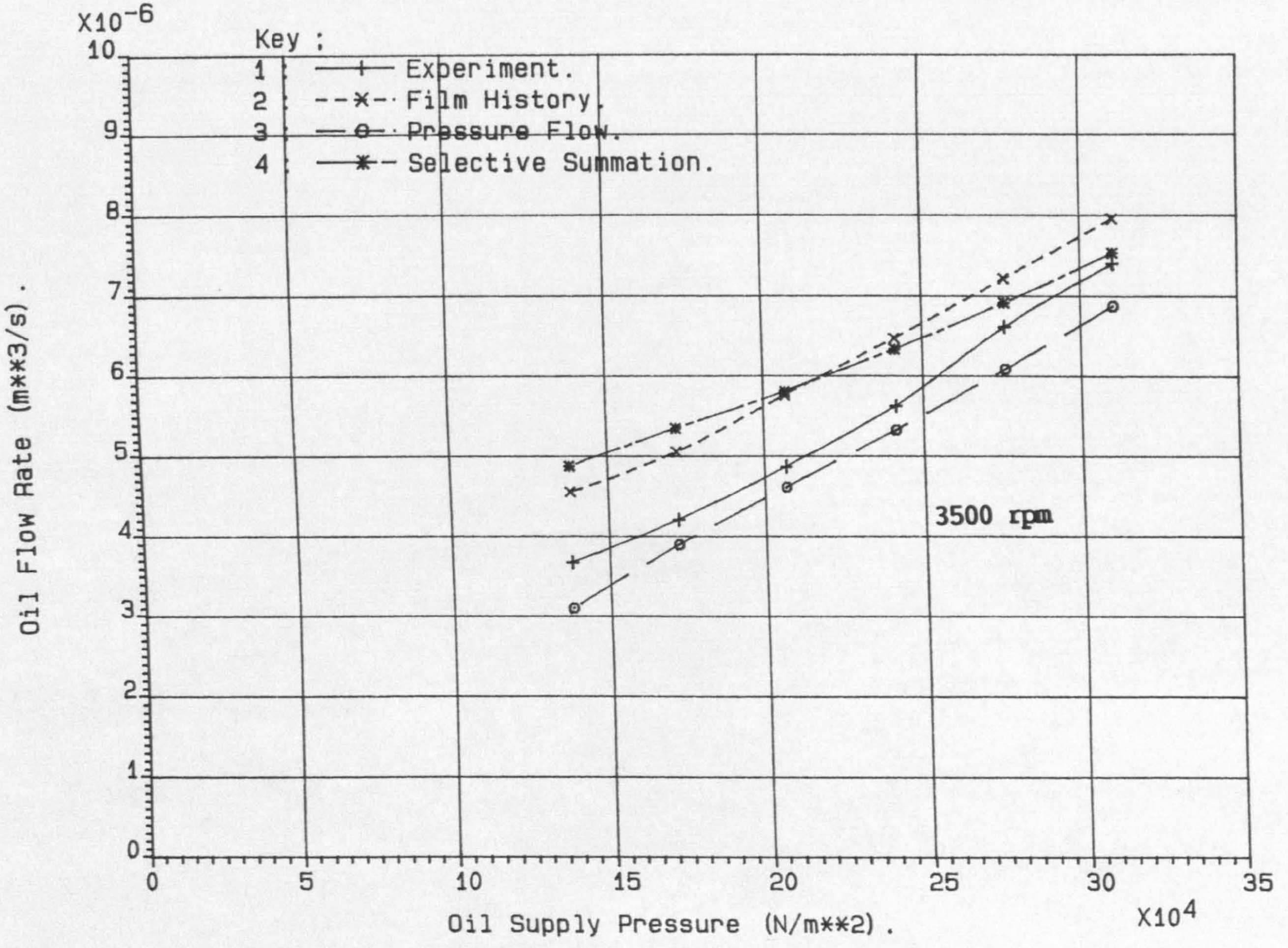

Figure 7.4 Oil Flow Rate Variation With Supply Pressure.
(Comparison Of Author's Predictions With Experimental Data).

2. At shaft rotational speeds of 2500 rpm (41.7 Hz) and 3500 rpm (58.3 Hz) it can be seen that all the author's flow rate predictions overestimate the experimentally determined oil flow rate. For these cases the effective oil temperature (T_5) gives the closest agreement with the test data, while (T_0) overestimates the oil flow rate by as much as 45% (2500 rpm, P_s=137.9 kN/m^2 (20 psi)). For the case where (T_5) is taken as the effective oil temperature the theoretical predictions overestimate the experimentally determined oil flow rate by a maximum of 24%.

3. The agreement between the experimental data and the author's theoretical predictions are better at lower journal speeds than at higher speeds. For higher shaft speeds the oil temperature rise between the bearing inlet and outlet could be as high as 28°C. Hence, the assumption of an isoviscous lubricant is less tenable.

It can be seen from Table 7.2 that the temperature distribution within the bearing was biased more to the outlet than the inlet temperature. However, the temperature rise between the oil supply groove and thermocouples at axial positions (3) can be several degrees, and this region of lower bearing (and presumably oil temperatures) could significantly influence the oil flow rate entering the bearing. A more accurate prediction of the bearing oil flow rate could be made if this region was modelled and an account of the varying viscosity considered. In addition, in any subsequent experimental work the axial temperature profile in this region of the bearing could be investigated.

Figures 7.3 and 7.4 give a comparison of the experimentally determined oil flow rates with those predicted by the author's rigorous and simple preditive techniques. The effective oil temperature has been taken to be equal to (T_5). The close agreement of all the sets of data is apparent. This is due to the dimensionless bearing supply pressures which can be as high as 0.5.

7.4.2 The Oil Flow Rate Variation with Shaft Rotational Frequency

Figure 7.5 shows the effect of the journal rotational frequency on the oil flow rate. A comparison is given between the experimental data and the predictions from the author's film history solution technique, using the three effective oil temperatures defined previously. As seen in Figures 7.1 and 7.2, the theoretical predictions for which the effective temperature was taken as (T_5) gave the closest agreement with the experimental data.

In addition, it should also be noted that the experimental data reflects a decrease in the oil flow rate with increase in shaft speed, whereas the author's predictions tend to give the opposite trend. This could be due to several factors. Since the temperature rise through the bearing increases as the journal speed is increased, there is a greater range of temperature between which the effective temperature can be, and the assumption of an isoviscous oil film becomes less valid. In addition, the temperature of the oil rises rapidly in the axial direction from the bearing groove to thermocouples at axial position number 3, where it then remains almost constant until the bearing edge.

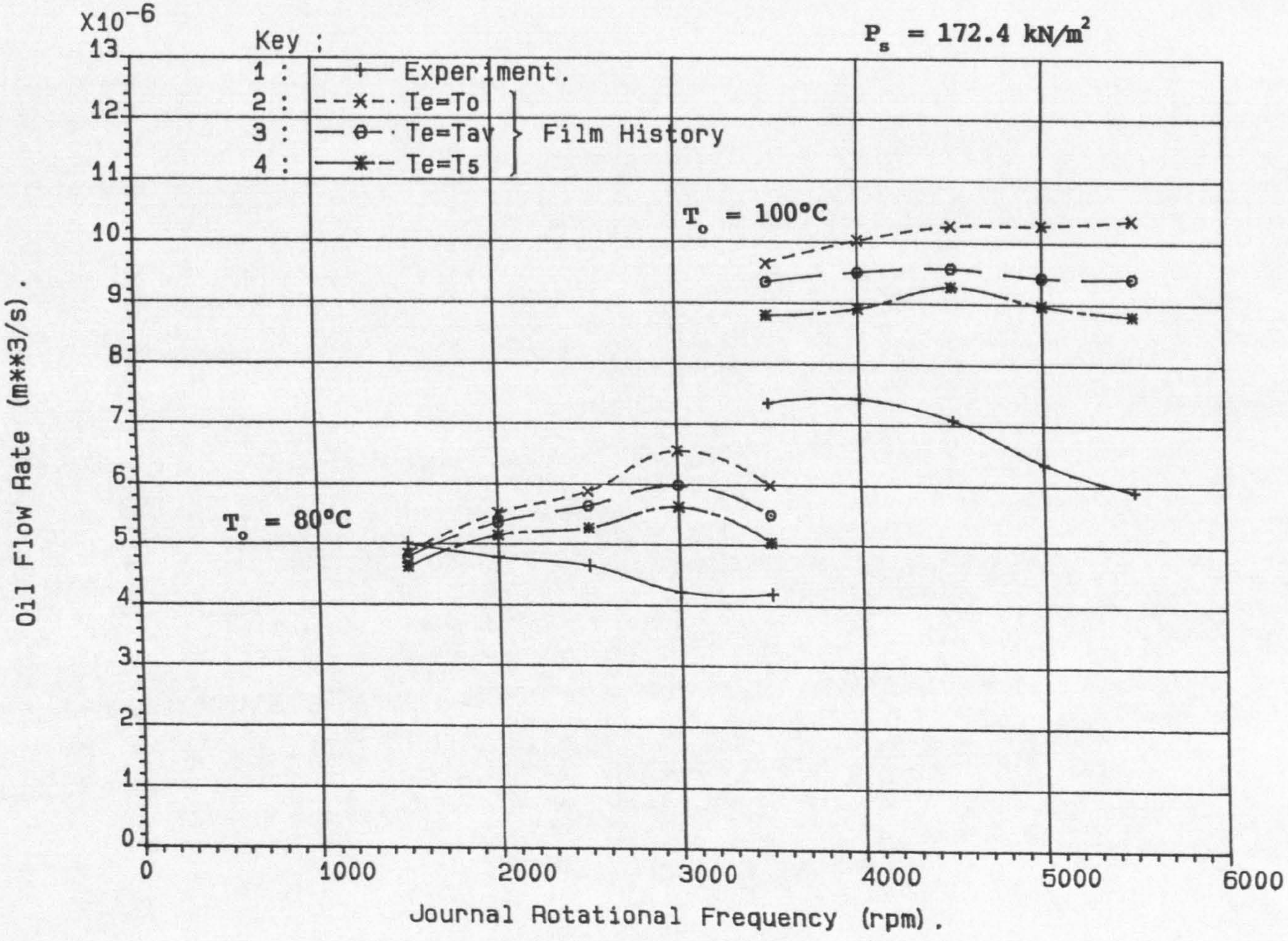

Figure 7.5 Oil Flow Rate Variation With Journal Rotational Speed.

It has been noted in Section 7.4.1 that a more accurate oil flow rate prediction could be made if the viscosity variation in this region of the bearing was modelled. The oil flow rate variation with journal speed is shown in Figure 7.6. The effective oil temperature has been taken to be equal to (T_5) and a comparison between the experimental data and the author's predictions using the simplified oil film history solution technique, the pressure flow equation, and the selective summation of the steady state flow (Q_s) and the translational flow (Q_T) is given. It can be seen that as with the results of Jones (1982), the film history solution tends to overestimate the experimentally determined oil flow rate, while the pressure flow equation alone gives a good estimate of the total bearing side leakage.

It is interesting to note that for the Ricardo Hydra, operating at the conditions used in these tests, the pressure flow accounts for about 90% of the total flow when the pressure and hydrodynamic flow rate components were calculated from Equations 3.28. This indicates that for full central circumferentially grooved bearings the pressure flow equation alone can be used to give a good estimate of the bearing side leakage and a consideration of oil availability within the bearing is not worthwhile.

Figure 7.7 shows the oil flow rate variation with shaft speed predicted by the author's more rigorous analysis techniques. It can be seen that each curve gives the incorrect trend when compared with the experimental data. The oil temperature was 80°C and the supply pressure was 172.4 kN/m^2 (25 psi) and it can be seen that the agreement between all the theoretical pedictions and the experimental data is good at the lower shaft speeds. However, due

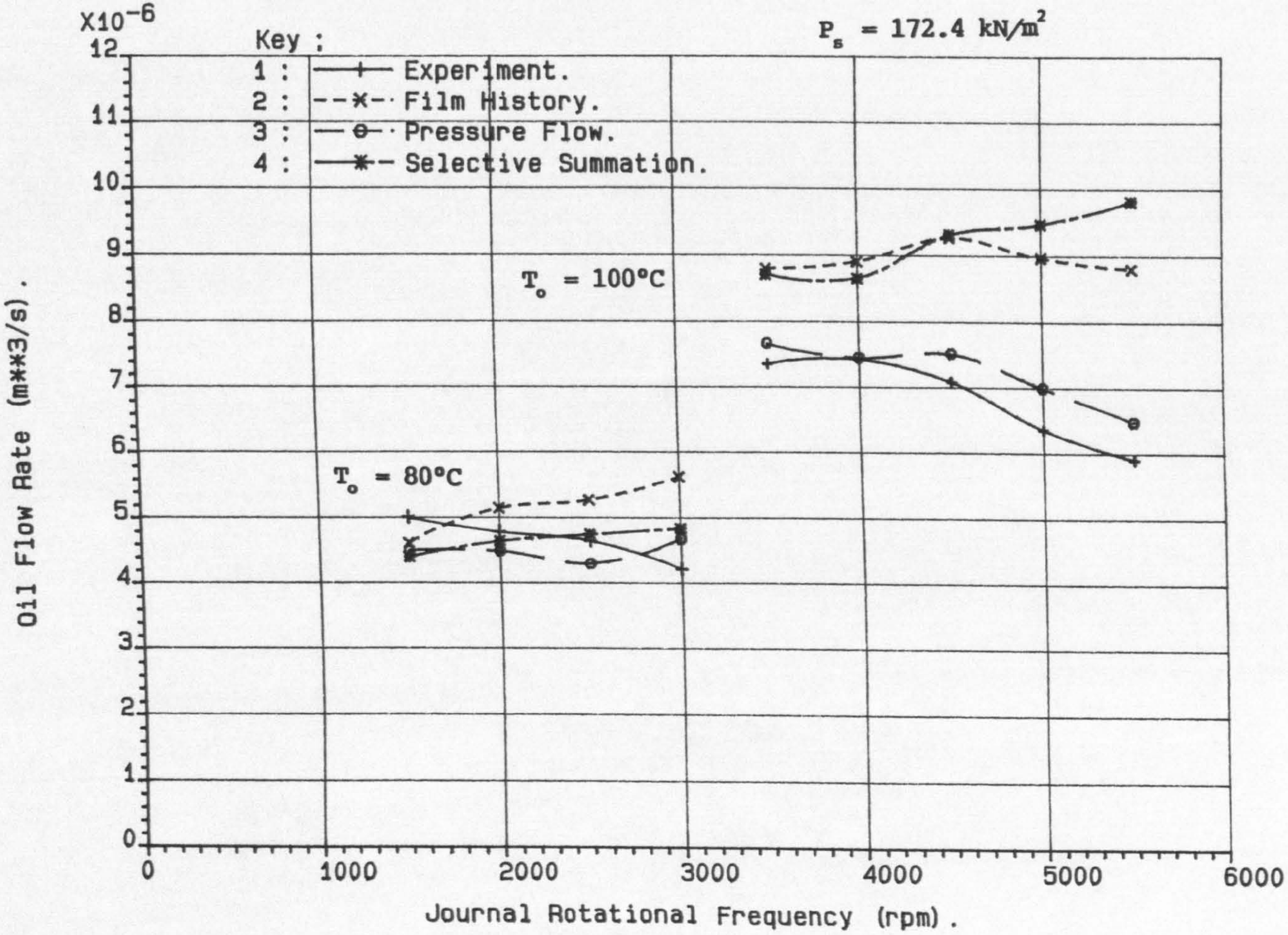

Figure 7.6 Oil Flow Rate Variation With Journal Rotational Frequency (Comparison Of Author's Predictions With Experimental Data).

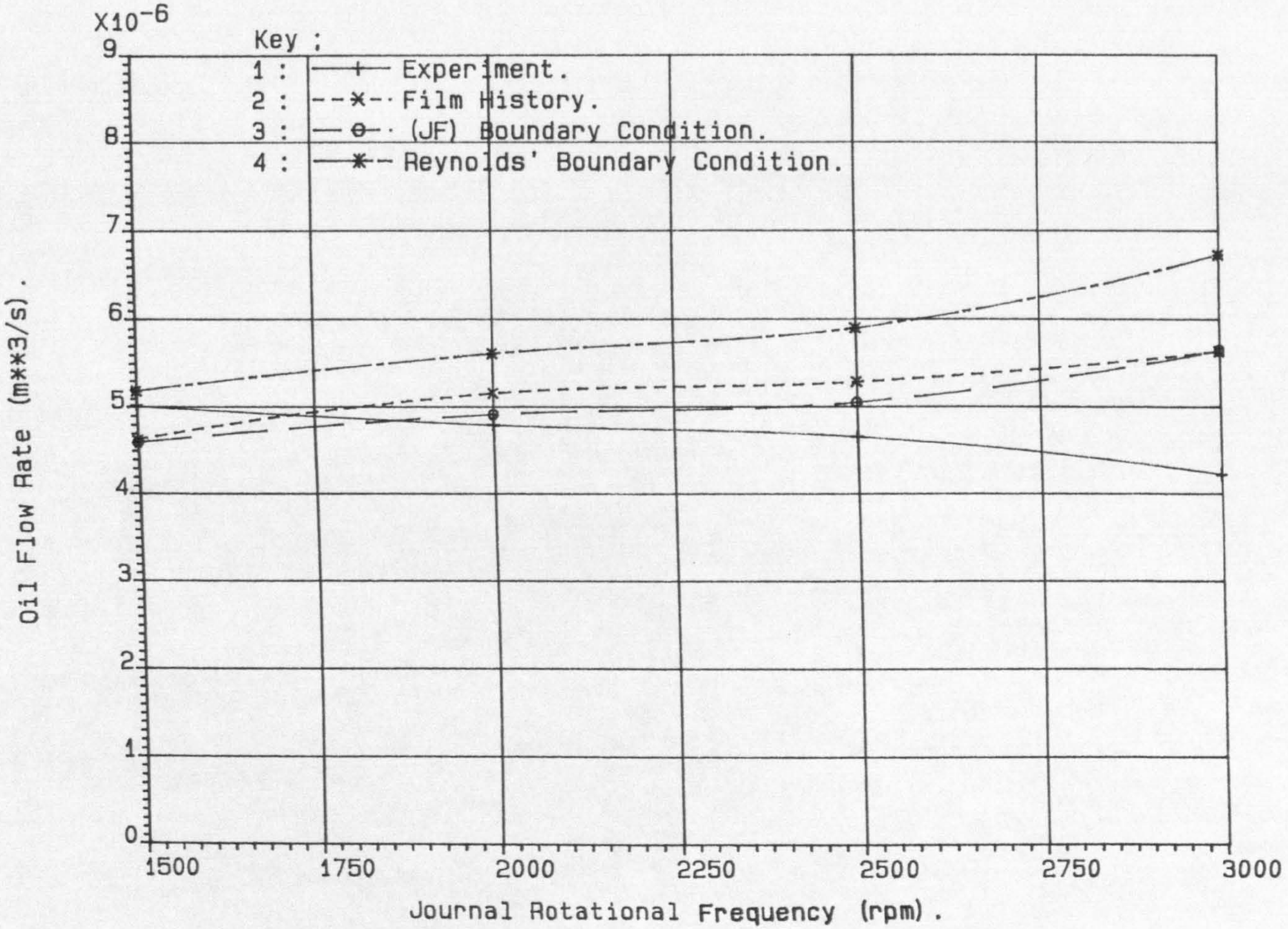

Figure 7.7 The Influence Of The Boundary Condition On The Theoretically Predicted Oil Flow Rate (Note false origin).

to the difference in the trends between theory and practice, the author's film history solution can be seen to overestimate the experimental flow rate by 35% at a shaft speed of 3000 rpm (50Hz).

7.4.3 The Effect of Considering the Effective Oil Temperature to be Equal to the Inlet Oil Temperature

The problem of the sharp temperature rise (in the axial direction) at the inlet to the bearing has been discussed previously and the possible influence of this on the oil flow rate entering the bearing has been pointed out. For the design of steadily loaded full circumferentially grooved bearings (ESDU 66023 (1966)) the oil flow rate entering the bearing is calculated by assuming that an appropriate oil viscosity would be that determined at the mean of the effective and inlet oil temperatures. In the present analysis this could be taken as being the mean of the outlet and inlet oil temperatures, however, in this section the effective oil temperature has been taken as equal to the inlet oil temperature since this provides a fundamental oil viscosity at a measured oil temperature.

Two methods of solution have been investigated. These were:-

(i) The effective temperature for the orbit and oil flow rate predictions has been set equal to the inlet oil temperature.

(ii) The journal orbit was calculated by assuming that the effective oil temperature was equal to the effective temperatures defined in Section 7.3. Then the oil flow rate was determined from the pressure flow equation at the viscosity determined from the inlet oil temperature. For the film history solution the Reynolds equation was solved by normalizing the oil supply pressure with respect to the inlet oil viscosity.

However, for all the test points considered, this leads to predictions of very low oil flow rates and for case (i) the power loss was increased substantially.

7.5 The Thermal Solution

For all the theoretical predictions given so far in this chapter, the effective oil temperature has been determined from the experimentally determined temperature distribution in the bearing and the outlet oil temperature. However, such data will not be available at the design stage, and hence, the effective oil temperature will have to be estimated by the designer. This could be determined by reading across from other similar engines, or by balancing the predicted power loss within the bearing to the product of the oil mass flow rate, specific heat and temperature rise through the bearing. It should be noted that this does not necessarily give the correct effective or outlet oil temperature, since the influence of heat transfer from the bearing is not modelled and the relationship between the two temperatures is not known. Hence, two important assumptions were made regarding the analysis. These were:-

(i) The effective oil temperature has been taken as being equal to the calculated outlet temperature from the bearing.

(ii) An adiabatic situation was assumed in which all the viscous energy dissipation in the bearing was carried away by the oil (i.e. $K=1$).

Figures 7.8, 7.9 and 7.10 give a comparison of the experimentally determined outlet oil temperature, oil flow rate and power loss with those predicted by the author. The oil inlet temperature was fixed at 55°C for shaft speeds within the range 1500-4000rpm (25 - 66.7 Hz) and at 95°C for shaft speeds within the range 3000-5500rpm (50 - 91.7 Hz). The oil supply pressure was 310.3 kN/m^2 (45 psi) and the experimentally determined power loss prediction was made by calculating the energy required to raise the oil flowing through the bearing from the inlet to the outlet temperature. The oil specific heat was calculated from Equation 7.1 at the mean of the oil inlet and outlet temperatures.

The predictions of the selective summation technique are not included in the present analysis, since it can be seen that it does not provide an advantageous oil flow rate specification technique. This was shown in Section 7.4. For the simple analytical solution presented, the power loss (2π film assumed) and oil flow rate (pressure flow equation) have been calcuated for a journal centre orbit determined from finite bearing theory.

Figure 7.8 shows the outlet oil temperature variation with shaft speed. The close agreement between the experimental and theoretical predictions is apparent, particularly at the lower journal speeds for each inlet oil temperature. This is due to the relatively low oil temperature rise through the bearing. At higher shaft speeds the discrepancies are about 5-6°C, but this is quite

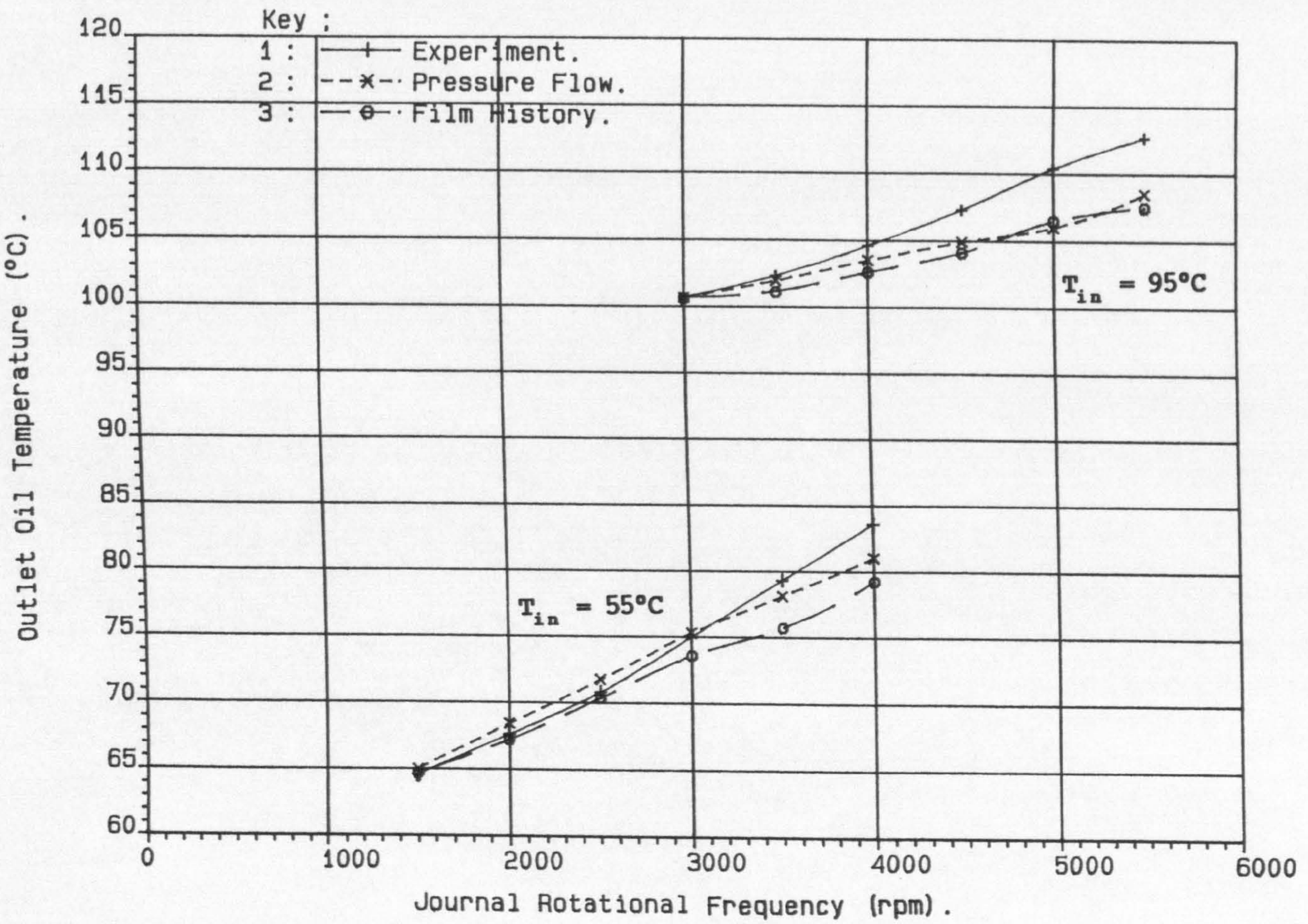

Figure 7.8 Outlet Oil Temperature Variation With Journal Rotational Frequency - Thermal Solution (Note false origin).

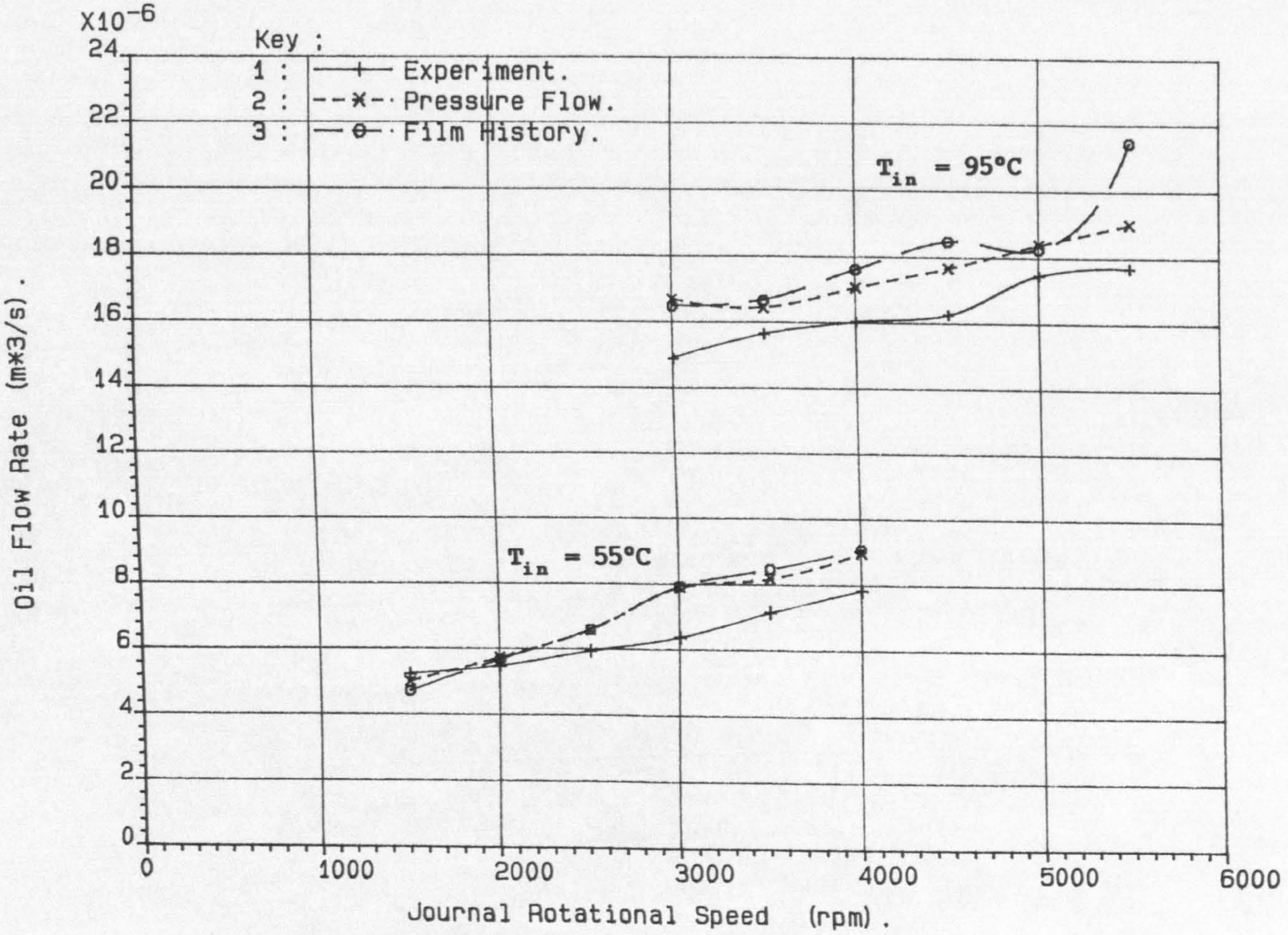

Figure 7.9 Oil Flow Rate Variation With Journal Rotational Frequency - Thermal Solution.

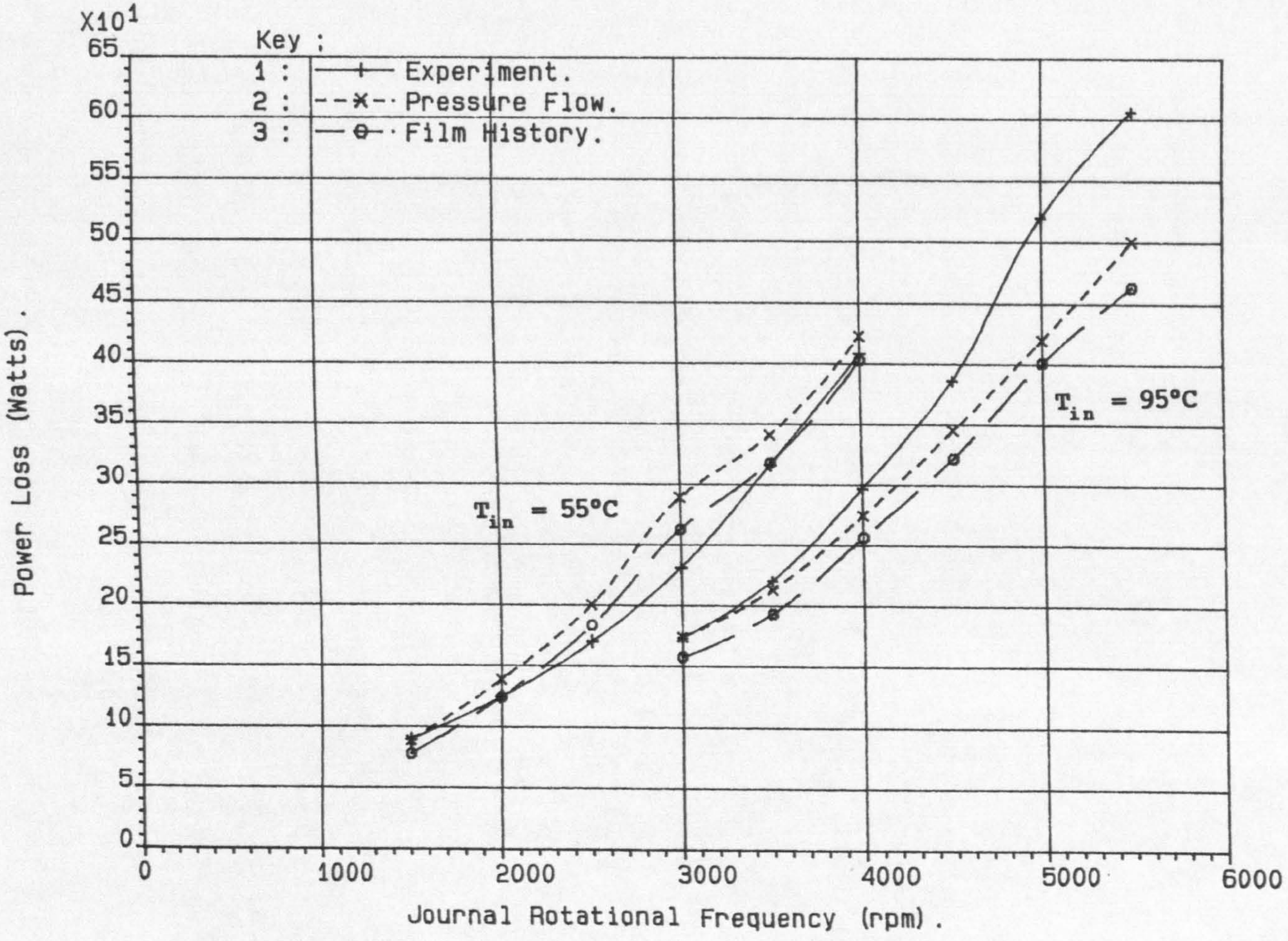

Figure 7.10 Power Loss Variation With Journal Rotational Frequency - Thermal Solution.

satisfactory.

The oil flow rate variation with shaft speed is shown in Figure 7.9. It can be seen that the author's predictions generally overestimate the experimentally determined values. This can be as much as about 25% at a shaft speed of 3000 rpm (50Hz) and an inlet oil temperature of 55°C. However, the theoretical predictions generally overestimate the experimental data by between 10 and 20%.

A comparison of the experimental measurements and theoretical predictions of the bearing power loss is given in Figure 7.10. It can be seen that for an inlet oil temperature of 55°C the theoretical predictions overestimate the experimental data by a maximum of 26%. This occurs at a journal rotational speed of 3000 rpm. For an inlet oil temperature of 95°C the maximum discrepancy between the theoretical predictions and the experimental data occurs at a shaft rotational speed of 5500 rpm. For this case the experimentally determined power loss is about 33% greater than the lowest theoretical prediction.

It can be seen from the figures that the rigorous film history solution has no benefit for the analysis of the Ricardo Hydra main bearing. The performance characteristics can be calculated based on assuming a fully flooded bearing for the purposes of shear power loss predictions, and by calculating the oil flow rate from the pressure flow equation.

7.6 The Influence of the Diametral Clearance on the Bearing Performance

It was pointed out in the previous section that simple expressions for the oil flow rate and power loss can be used in an iterative solution to determine the performance characteristics of the bearing under consideration.

However, these differences are of secondary importance from a design point of view, since the tolerances on the bearing and journal diameters (for the Ricardo Hydra) could give a diametral clearance in the range 50-120μm. This corresponds to a factor of 2.4, and from the pressure flow equation (Equation 1.6) could give oil flow rates which vary by a factor of about 13.8. Similarly, the power loss, minimum oil film thickness and outlet oil temperature will be affected. This is shown in Figures 7.11, 7.12, 7.13 and 7.14 where the results of a thermal solution are presented. The variation of the different performance characteristics with journal rotational frequency is shown. The oil inlet temperature for all the figures was 95°C and the analysis assumed a fully flooded bearing. The oil flow was calculated from the pressure flow equation.

Figure 7.11 shows the outlet oil temperature variation with shaft speed for the extremes of diametral clearances. The theoretical predictions for a diametral clearance of 88μm are also plotted. It can be seen that a decrease in the bearing clearance gives a marked increase in the outlet oil temperature. This is principally due to the decrease in the oil flow rate, since the power loss is relatively unaffected by clearance changes. This is shown in Figures 7.12 and 7.13.

It can be seen from Figure 7.12 that the oil flow rate through the larger diametral clearance bearing can be between 7.5

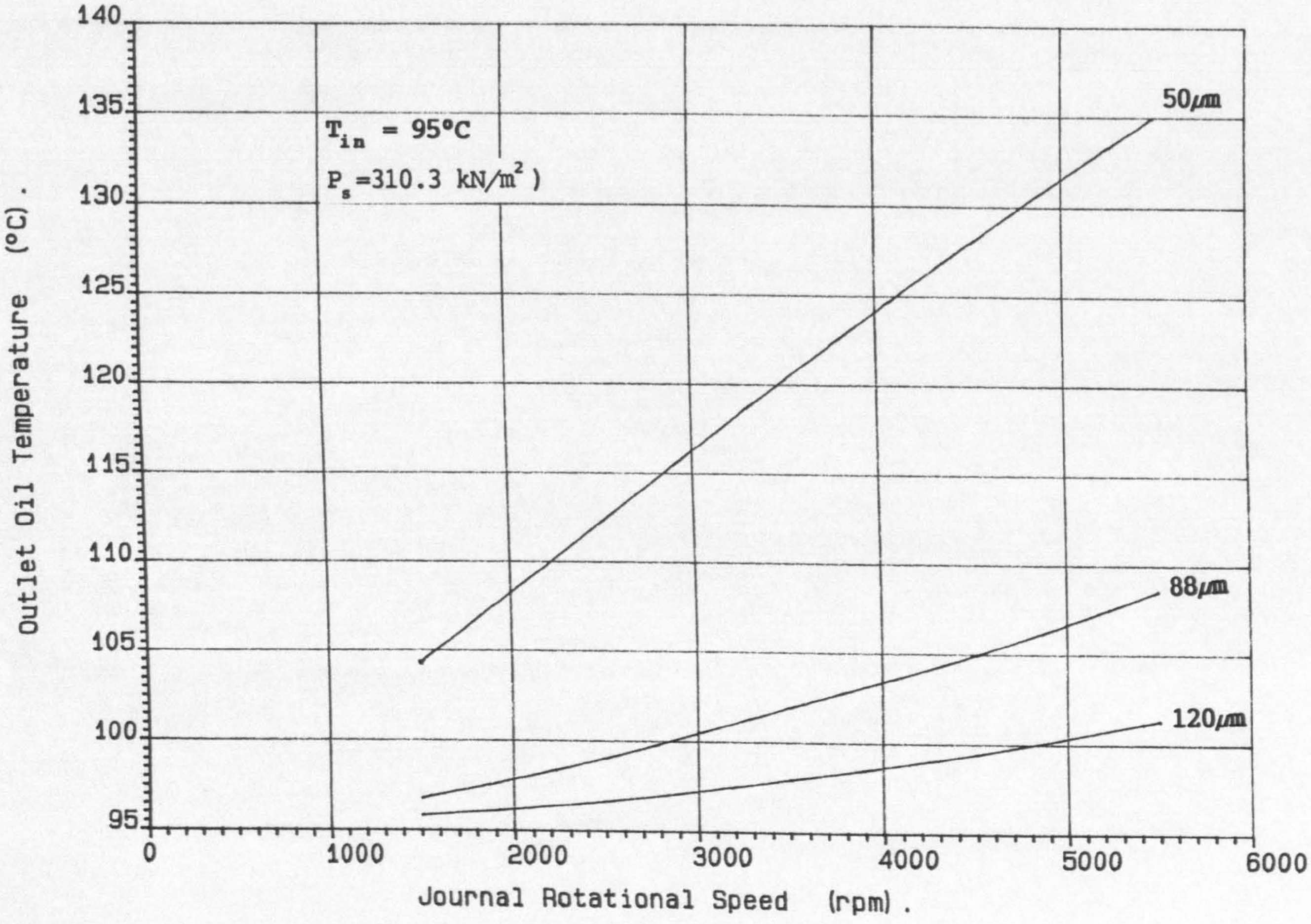

Figure 7.11 Outlet Oil Temperature Variation With Journal Rotational Frequency For Three Diametral Clearances (Note false origin) .

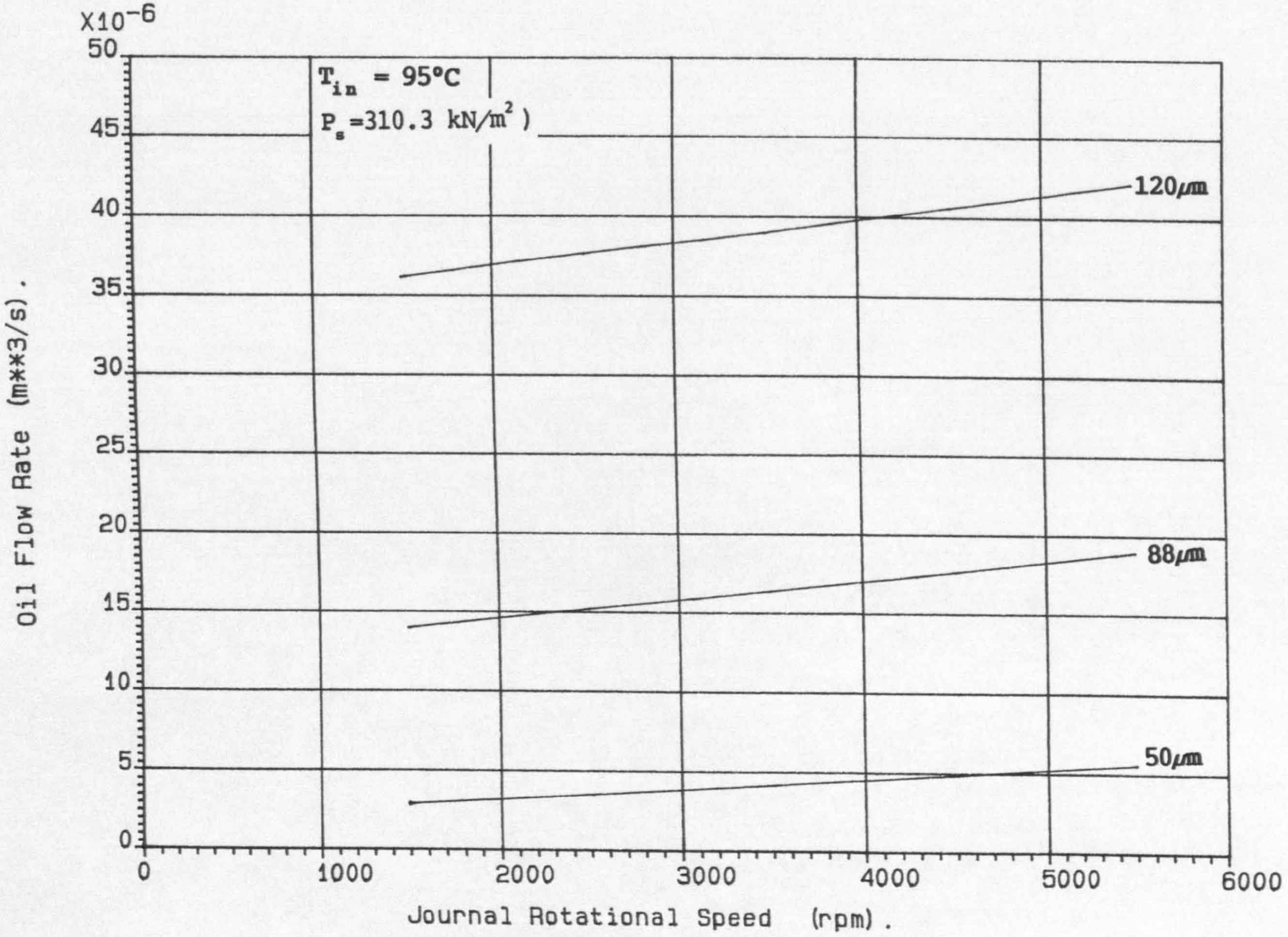

Figure 7.12 Oil Flow Rate Variation With Journal Rotational Frequency For Three Diametral Clearances.

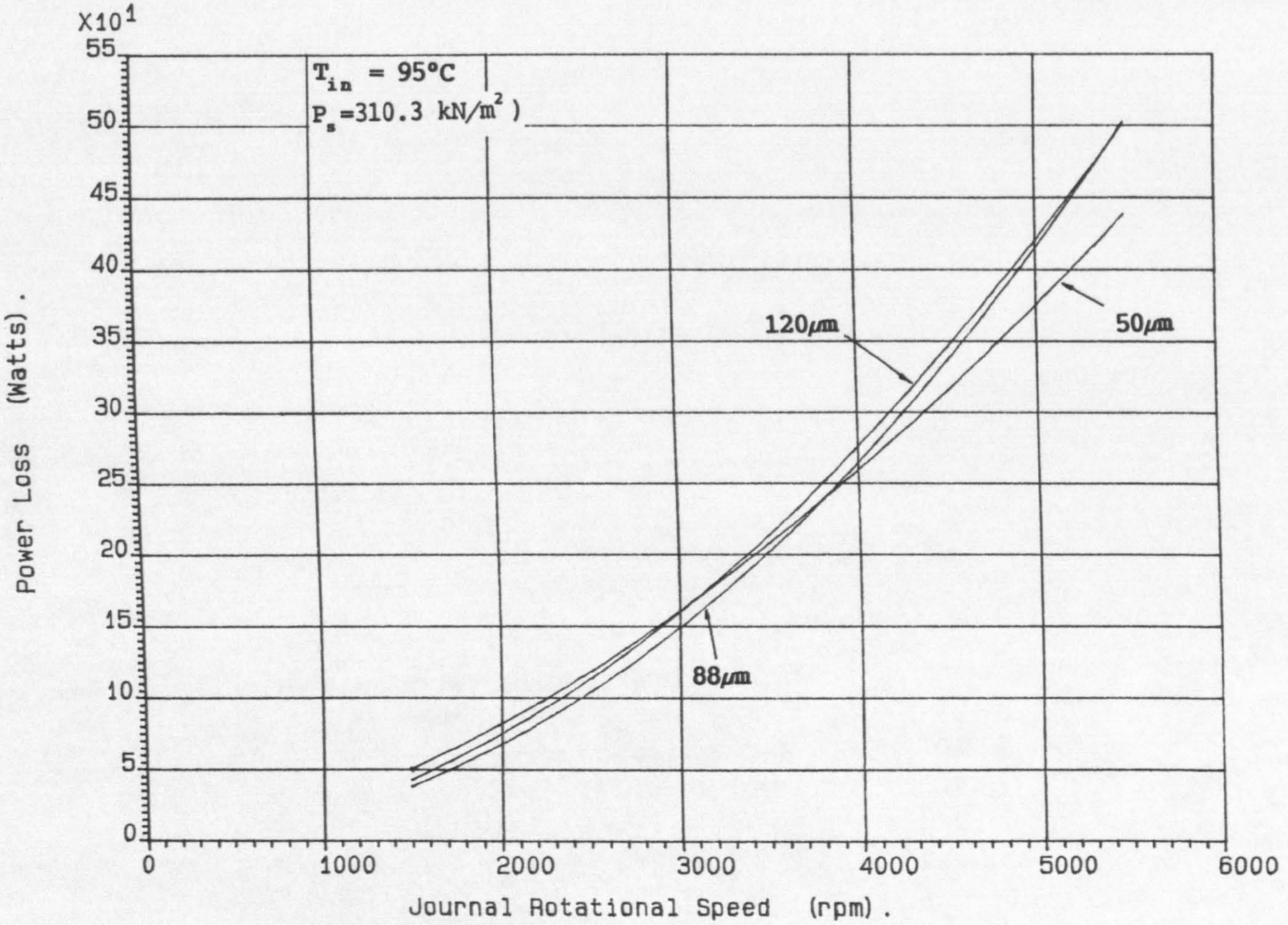

Figure 7.13 Power Loss Variation With Journal Rotational Frequency For Three Diametral Clearances.

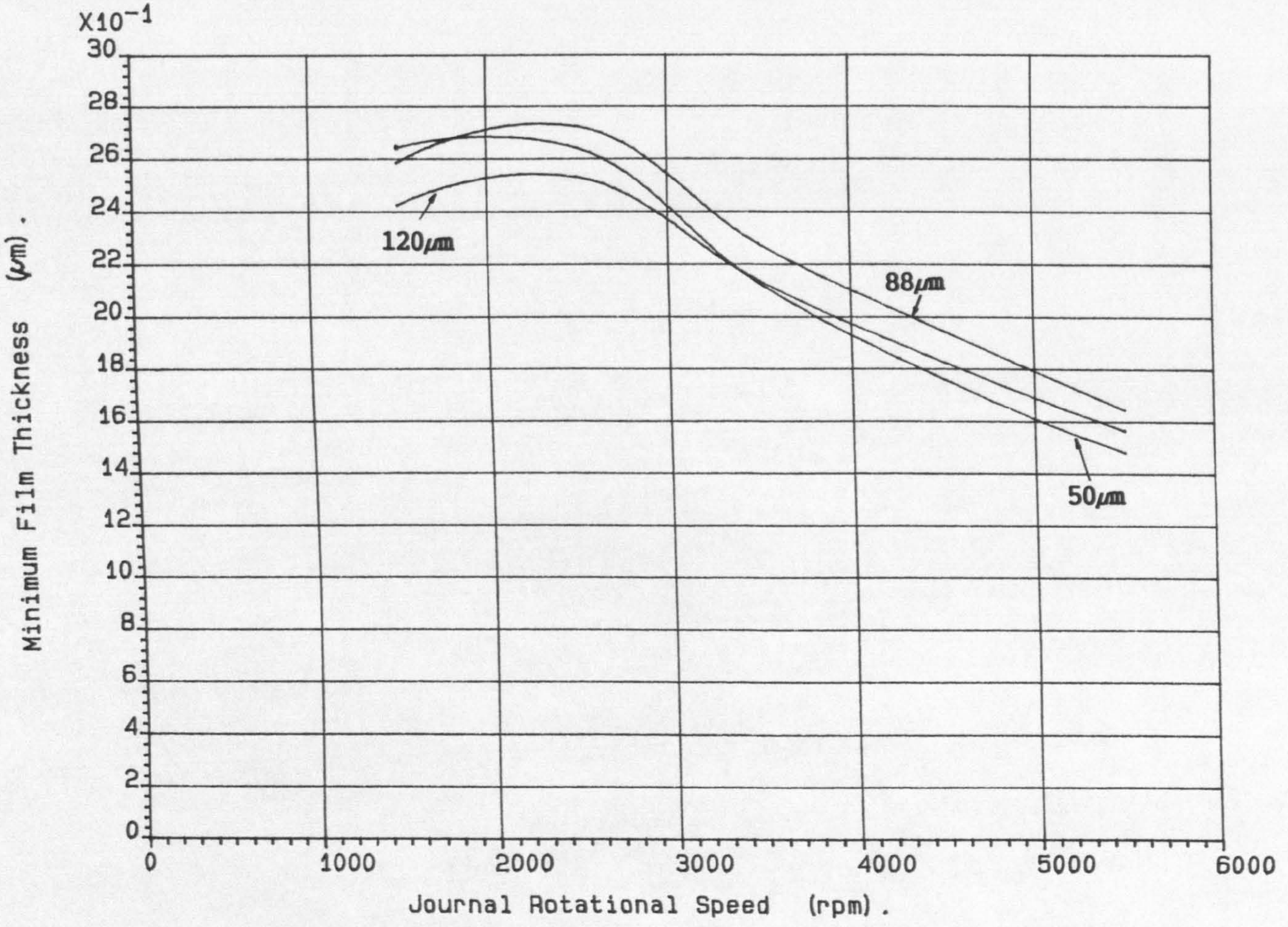

Figure 7.14 Minimum Film Thickness Variation With Journal Rotational Frequency For Three Diametral Clearances.

and 12.5 times greater than the oil flow rate from the smaller diametral clearance bearing. For the experimental diametral clearance of 88μm the theoretical flow rate predictions are at most 1.5 times greater than the experimental data (see Figures 7.1 to 7.7), an inaccuracy of the design stage which is negligible when compared to the possible variations in oil flow rate from production bearings.

Figure 7.13 shows the power loss variation with shaft speed. It can be seen that for this case the diameteral clearance has a minimal effect on the power loss, even though the velocity gradient across the film is much higher at lower clearances. However, since the effective oil temperature is also much higher, there is a balance resulting in a relatively small power loss variation.

Figure 7.14 shows the variation of the minimum oil film thickness with shaft speed for diametral clearances of 50, 88 and 120μm. It can be seen that the minimum film thickness increases for shaft speeds of 1500-2500 rpm (25-41.7 Hz) and then falls as the shaft speed is increased to 5500 rpm (91.7 Hz). These trends are caused by a combination of several factors, including:

(i) The reduction in the oil effective viscosity
(ii) The increased inertia loading
(iii) The increase in journal rotational frequency tending to give lower eccentricty ratios.

7.7 The Variation of Oil Flow Rate with Crank Angle

Figure 7.15 shows the perdicted instantaneous oil flow rate variation with crank angle for the film history and pressure flow solutions. This particular test condition is presented since it illustrates an important difference between the solutions in which the journal centre translational velocity (and rotational component) are considered to determine the bearing side leakage, and that where just the pressure flow is considered.

It can be seen from Figure 7.15 that the pressure flow variation with crank angle 'leads' the flow rate variation with crank angle which was determined from the film history solution. This can be illustrated by inspection of the flow rate variations between crank angles of about 300° and 480°. The reason for this is that when the journal centre position moves from a high to low eccentricity ratio (crank angle of ≈ 330°) the pressure flow immediately starts to fall. However, the film history solution predicts a flow peak (due to the velocity component of flow) followed by a decrease in the oil flow rate due to the lower eccentricity ratios. This point was also noted in relation to Figures 5.3 and 5.4 where an almost constant pressure flow was obtained throughout the journal centre orbit, except for small 'dips' at the position of the flow peaks predicted by the film history solution and the hydrodynamic flow rate equation.

7.8 The Journal Centre Orbit Determination

The experimental determination of the journal centre orbit was unsuccessful and for this reason only one of the measured orbits

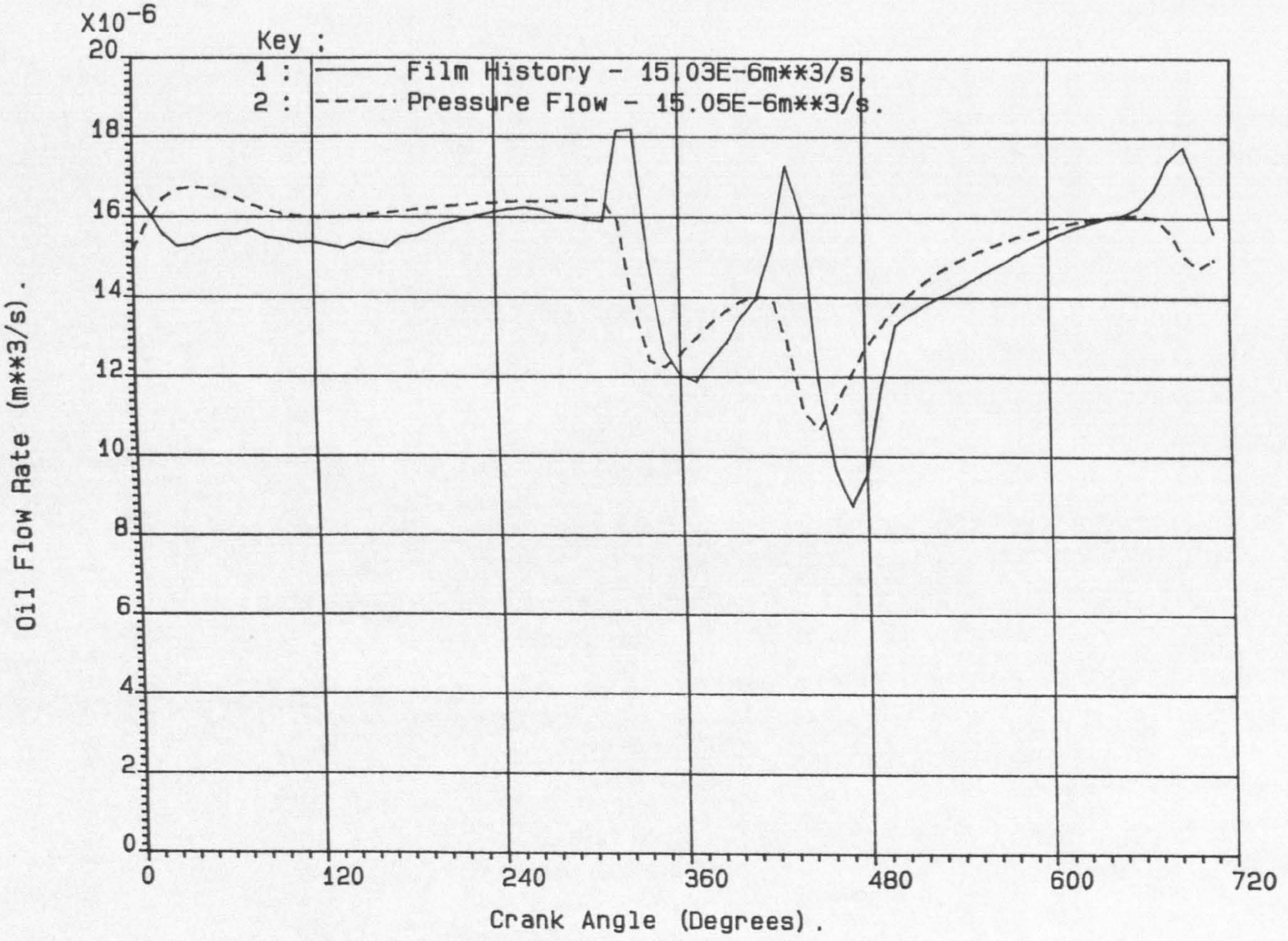

Figure 7.15 Oil Flow Rate Variation With Crank Angle.
(1500rpm T_e =100°C P_s =310.3kN/m**2)

presented.

At high journal rotational frequencies (4000 rpm (66.7Hz.)) and above, it was observed that the oscilloscope trace had what appeared to be high frequency noise superimposed on the required signal. This masked any orbit measurement which may have been obtained. The reasons for this are not clear, but it could have been due to deflections and oscillations of the shaft, bearing or the transducer carrying ring. The transducers were, however, secured firmly into the carrying ring by tightening the locking nuts, and the transducer holder was secured firmly to the bearing housing.

The theoretical orbit prediction for the Ricardo Hydra at a shaft rotational frequency of 3000 rpm is given in Figure 7.16. For journal rotational frequencies of 3000 rpm (50 Hz) and 3500 (58.3 Hz) what could be seen to approximate to the theoretically predicted inertia loop was observed, in addition to a vague overall similarity between the theoretical and experimentally determined orbit. This is shown in Figure 7.16 for a journal rotational speed of 3000 rpm (50 Hz) and an effective oil temperature of 80°C.

7.9 Errors Associated with Determining the Bearing Diametral Clearance

Some of the errors associated with the oil flow rate determination were discussed in Chapter 6. However, the uncertainties associated with the determination of the bearing diametral clearance, and its subsequent use in the theoretical analysis, are perhaps the most significant reason why differences

Predicted Orbit

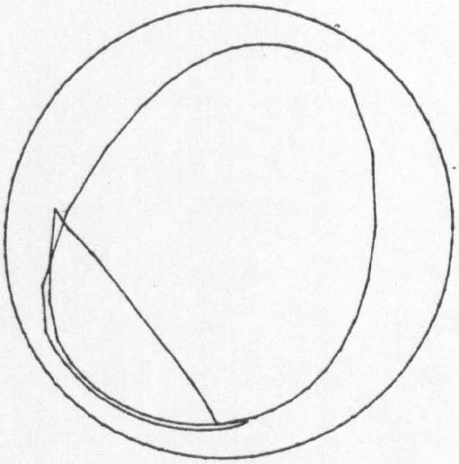

Measured Orbit

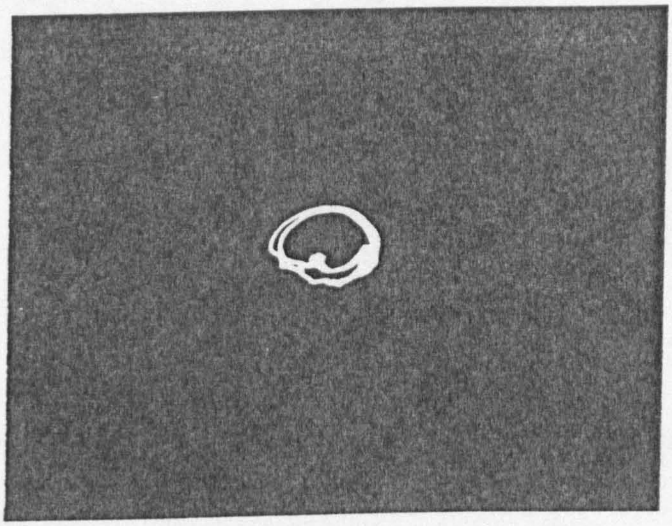

Figure 7.16 Comparison of The Theoretical (Finite Bearing Theory) and Measured Journal Orbits (3000rpm T_o = 80°C)

were obtained between the theoretical and experimental data.

The clearance was determined by calculating the difference between the bearing and journal diameters. These were measured at several angular positions for each bearing land (and corresponding shaft axial positions) and a mean value for each was calculated. However, it was found that the differences in the diameters due to out of roundness of the components could cause the diametral clearance to vary by about ± 6μm. This meant that the 'cold' diametral clearance of the bearing could be within the range 82-94μm and this could influence the bearing side leakage significantly.

In addition, it was observed that the bearing diameter could vary by several micrometres at the same angular position for each bearing load. Since the theoretical minimum film thicknesses were of the same order of magnitude, it is apparent that one of the bearing lands would have taken more than half the total load acting on that bearing. This would have influenced the journal eccentricity ratio, power loss, oil flow rates and bearing temperatues, and hence accounted for some of the differences in the experimental and theoretical data.

Thus it can be seen that in addition to the factor of 2.4 on the diametral clearance, which is permitted from the journal and bearing tolerances, the out of roundness of the actual components (before loading) is an important feature. Two bearings which have nominally the same diametral clearance can have totally different shapes. This emphasises the point made earlier, that rigorous film history analyses have no benefit for the consideration of the Ricardo Hydra bearings.

A rigorous analysis at the design stage would only be worthwhile if it was known that the bearings could be made with a small tolerance on the diametral clearance, and the bearing and journal shapes could be stringently controlled on production engines. Such constraints would inevitably lead to more efficient engines and it was pointed out by Monaghan (1987) that if all engines could be manufactured such that their frictional losses were as low as the best in the scatter band, then a 5% fuel saving could be made.

7.10 Conclusions

In this chapter experimental data for the Ricardo Hydra has been presented and compared with the author's theoretical predictions. The conclusions which can be drawn from this work will now be presented:

1. Three possible effective oil temperatures have been defined. These were the outlet oil temperature and two additional average temperatures which were obtained from the readings of the thirty-two bearing thermocouples. It was found that the definition which gave the lowest effective temperature provided the closest agreement between the author's theoretical predictions and the experimental data.

2. An almost linear increase of the oil flow rate with supply pressure was obtained, even though the test points had slightly different effective oil temperatures. For a constant viscosity, the pressure flow equation predicts a

linear increase in the oil flow rate with supply pressure.

3. The experimental data gave a general decrease in the bearing side leakage as the shaft rotational frequency was increased. Only the flow rate predictions based on the pressure flow equation gave this trend. The more rigorous analyses gave an increase in the bearing oil flow rate with increase in the shaft rotational frequency.

4. As with the results of Cooke (1983), the oil flow rate predictions based on the film history solution tend to overestimate the experimentally determined oil flows, while the pressure flow equation provides predictions which are slightly lower than these values.

5. Theoretical analyses where the effective oil temperature has been determined from a thermal balance within the bearing are encouraging. This is particularly true for lower shaft rotational speeds where the oil temperature rise through the bearing was only a few degrees.

6. In view of the possible range of diametral clearances and variations in the journal and bearing shapes, it is concluded that rigorous analyses involving film history considerations have no advantage for the performance predictions of full central circumferentially grooved bearings.

CHAPTER 8

CHAPTER 8

Conclusions And Suggestions For Future Work

8.1 Conclusions

The objective of the research work, presented in this thesis, was to develop analytical techniques for the performance predictions in relation to dynamically loaded journal bearings. The results of the predictive techiques were then to be compared with experimental data collected as part of the research. These objectives have been achieved. Several computer programs of varying complexity have been developed and a considerable amount of experimental data for the front main bearing of a single cylinder engine has been amassed. For the present work the analysis has been limited to a consideration of full central circumferentially grooved bearings and the main conclusions of the research work will now be reviewed.

(1) The algorithm of Elrod and Adams (1974) has been used to develop an extensive amount of data for the performance prediction of steadily loaded full central circumferential grooved bearings. The oil flow rate data has been curve fitted and it has been shown that the pressure flow alone (without a consideration of bearing surface motion) gives an excellent estimate of the total bearing side leakage.

(2) The author has developed a simplified oil film history solution technique in which the journal centre velocities were determined from mobility curve fits. This gave

excellent agreement with the limited published data relating to previous film history solution techniques where the film history effect on the journal centre orbit was considered.

(3) Comparison of the author's oil flow rate predictions with the experimental data collected for the Ricardo Hydra engine showed that the oil flow rate in dynamically loaded full central circumferentially grooved bearings could be determined accurately from the pressure flow equation. No benefit was obtained by carrying out a rigorous film history solution analysis. In addition, it was found that the shear power loss could be determined accurately by considering a fully flooded bearing (2π film shear).

(4) In view of (3), it was found that a simple thermal analysis could be carried out to determine the bearing operating characteristics. The agreement with the experimental data was excellent.

(5) The tolerances on the journal and bearing diameters meant that for the Ricardo Hydra, the diametral clearance could vary by a factor of 2.4 for nominally identical bearing assemblies. This gave oil flow rates for the two cases which could vary by a factor of 12.5 (from the pressure flow equation). In view of this it is apparent that a rigorous analysis of such bearings cannot be justified. The need for accurate predictions of the performance of such bearings will only become necessary when the diametral clearance of the bearing can be stringently controlled. This is a manufacturing problem.

8.2 Suggestions For Future Work

The extension of the work presented in this thesis to partially grooved bearings and an experimental determination of the performance characteristics of such bearings would be a useful addition to the literature. The course of research could parallel that presented in this thesis, and hence, the following objectives could be set:

(1) A consideration of oil flow rate, power loss and load capacity for steadily loaded partial groove bearings. An attempt could be made to curve fit the data for the bearing side leakage as in the present work. The form given by Martin and Lee (1982) would provide a starting point.

(2) The generation of mobility data for partially grooved bearings. Since dynamically loaded bearings operate at high eccentricity ratios for much of the engine cycle, the region of high pressure generation has a relatively small angular extent. Hence, it is likely to lie in either the grooved or full bearing land width region. For these areas the mobility curve fits presented in this thesis are applicable. However, for cases where the pressure region is likely to lie close to the region of groove "run out" additional data needs to be generated.

(3) An approximate film history solution could then be carried out, using the new mobility curve fits of (2). The influence of the film history on the journal orbit would need to be established by comparison of the orbits where

film history is considered and where the mobility equations are used.

(4) An experimental investigation into the flow through steadily and/or dynamically loaded bearings would provide a useful validation for the work described in (1) - (3). The oil axial temperature profile close to the groove would be an important and interesting parameter to investigate. This may lead to a clearer understanding of the influence of the oil inlet temperature on the bearing effective temperature.

Subsequent to obtaining a clear understanding of the operation of partial groove bearings the analysis of oil hole fed bearings would provide a further research area.

REFERENCES

Ayele, K. (1988), 'Oil Flow in Steadily Loaded Central Circumferentially Grooved Journal Bearings. M.Sc. Thesis, Dept. of Mech. Eng., University of Leeds.

Bell, J.C. (1988), 'Private Communication', Shell Thornton Research Centre, Chester.

Booker, J.F. (1965), 'Dynamically Loaded Journal Bearings: Mobility Method of Solution'. Trans. ASME, Jnl. Basic Engineering, Sept. 1965, pps 537-546.

Booker, J.F. (1979), 'Design of Dynamically Loaded Journal Bearings'. The Design Engineering Conference Chicago, Illinois, May 7-10, 1979, pps. 31-44.

Cameron, A. (1981), 'Basic Lubrication Theory', 3rd Edition. Ellis Horwood Series in Engineering Science. pp.25.

Campbell, J., Love, P.P., Martin, F.A., Rafique, S.O. (1967)., 'Bearings for Reciprocating Machinery: A Review of the Present State of Theoretical, Experimental and Service Knowledge'. Conference on Lubrication and Wear : Fundamentals and Applications to Design. Pub. Instn. Mech. Engs.

Clayton, G.A. and Taylor, C.M. (1988), 'Thermal Considerations in Engine Bearings', Proc. 15th Leeds-Lyon Symposium on Tribology, Tribological Design of Machine Elements. Pub. Elsevier, pps. 333 - 342.

Cooke, W.L. (1983), 'Performance of Dynamically Loaded Journal Bearings, Part 1 : Effect of Varying Bearing Geometry and Oil Supply Conditions, NEL Report No. 683.

Dubois, G. and Ocvirk, F.W. (1953), 'Analytical Derivation and Experimental Evaluation of Short Bearing Approximation for Full Journal Bearings', N.A.C.A. Report, 1157.

Elrod, H.G. (1981), 'A Cavitation Algorithm'. Trans. ASME, Jnl. of Lub. Tech., July 1981, Vol. 103, pps. 350-354.

Elrod, H.G. and Adams, M.L. (1974), 'A Computer Program for Cavitation and Starvation Problems'. 1st Leeds-Lyon Symposium on Tribology, Cavitation and Related Phenomena in Lubrication.

ESDU Item No. 66023 (1966), 'Calculation Methods for Steadily Loaded Pressure Fed Hydrodynamic Journal Bearings'.

ESDU Item No. 84031 (1984), 'Calculation Methods for Steadily Loaded Axial Groove Hydrodynamic Journal Bearings'.

Goenka, P.K. (1984), 'Analytical Curve Fits for Solution Parameters of Dynamically Loaded Journal Bearings'. Trans. A.S.M.E.; Jnl. of Trib., Oct 1984, Vol. 106, pps. 421-428.

Jakobsson, B. and Floberg, L, (1957), 'The Finite Journal Bearing Considering Vaporization'. Trans. Chalmers Univ. Technology, No. 190, Göteborg.

Jones, G.J. (1982), 'Crankshaft bearings: oil film history'. 9th Leeds-Lyon Symposium on Tribology, Tribology of Reciprocating Engines. pps. 83-88.

Jakeman, R.W. (1984). 'A Numerical Analysis Method Based on Flow Continuity for Hydrodynamic Journal Bearings'. Tribology International, Vol. 17, No. 6, pps. 325-333.

Lundholm, G. (1979), 'The Circumferential Groove Journal Bearing Considering Cavitation and Dynamic Stability'. ACTA Polytechnica Scandinavica, Mech-Eng. Series No. 42.

Martin, F.A. (1982), 'Developments in Engine Bearings'. 9th Leeds-Lyon Symposium on Tribology, Tribology of Reciprocating Engines, pps. 9-28.

Martin, F.A. (1985), 'Friction in Internal Combustion Engine Bearings'. Publ. I.Mech.E. (1985), C67/85.

Martin, F.A. (1989), 'Consultant to T & N Technology'. Private Communication.

Martin, F.A. and Lee, C.S. (1982), 'Feed Pressure Flow in Plain Journal Bearings'. Trans. ASLE, Vol. 26, 3, pps. 381-392.

McCallion, H., Lloyd, T. and Yousif, F.B. (1971), 'The Influence of Oil Supply Conditions on the Film Extent and Oil Flow in Journal Bearings', Proc. Inst. Mech. Eng. Tribology Convention.

Miranda, A.A.S. (1983), 'Oil Flow, Cavitation and Film Reformation in Journal Bearings Including an Interactive Computer-Aided Design Study'. Ph.D. Thesis, Dept. Mech. Eng., Univ. of Leeds.

Monaghan, M.L. (1987), 'Engine Friction - A Change in Emphasis'. Auto-tech '87, The Institution of Mechanical Engineers, B.P. Tribology Lecture 1987.

Ollson, K.O. (1965), 'Cavitation in Dynamically Loaded Bearings', Trans. Chalmers University of Technology, No. 308, Göteborg.

Paydas, A. (1988), 'An Investigation into Fluid Film Lubrication in Dynamically Loaded Bearings'. Ph.D. Thesis, Lancs. Poly, U.K.

Reynolds, O. (1886), 'On the Theory of Lubrication and its Application to Mr. Beauchamps Tower's Experiments, Including an Experimental Determination of the Viscosity of Olive Oil'. Phil. Trans. Soc., 177, 157.

Rowe, W.B. and Chong, F.S., (1984), 'A Computer Algorithm for Cavitating Bearings. Requirements of Boundary Conditions which Satisfy the Principle of Mass

Conservation'. Tribology International, 1984, Vol. 17, No.5, pps. 243-250.

Ruddy, A.V. (1979), 'The Dynamics of Rotor-Bearing Systems with Particular Reference to the Influence of Fluid-Film Journal Bearings and the Modelling of Flexible Rotors'. Ph.D. Thesis, Dept. of Mech. Eng., University of Leeds (1979).

Vijayaraghaven, D., Keith, T.G. (1988), 'Development and Evaluation of a Cavitation Algorithm', Dept. of Mech. Eng., University of Toledo, Ohio, U.S.A.

Appendix 1

Eccentricity Ratio	Dimensionless Load Capacity ($\bar{W}$)				
(ε)	b/d = 0.1	b/d = 0.2	b/d = 0.3	b/d = 0.4	b/d = 0.5
0.96	2.42	7.57	12.3	15.9	18.5
0.94	1.15	3.82	6.59	8.90	10.6
0.92	0.670	2.19	4.13	5.76	7.03
0.90	0.412	1.54	2.87	4.17	5.17
0.80	0.117	0.420	0.835	1.32	1.81
0.70	0.0582	0.223	0.434	0.702	0.966
0.60	0.0345	0.144	0.284	0.464	0.628
0.50	0.0223	0.0989	0.203	0.333	0.452
0.40	0.0146	0.0614	0.140	0.237	0.335
0.30	0.00928	0.0416	0.0965	0.163	0.238
0.20	0.00583	0.0271	0.0631	0.105	0.152
0.10	0.00240	0.0130	0.0371	0.0579	0.0767

Table A1.1 Dimensionless Load Variation With Eccentricity Ratio and Width-to-Diameter Ratio (Dimensionless Supply Pressure = 1.0)

Eccentricity Ratio	Dimensionless Load Capacity ($\bar{W}$)				
(ε)	b/d = 0.1	b/d = 0.2	b/d = 0.3	b/d = 0.4	b/d = 0.5
0.96	2.42	7.57	12.3	15.9	18.5
0.94	1.14	3.82	6.59	8.90	10.6
0.92	0.671	2.20	4.13	5.76	7.03
0.90	0.412	1.55	2.89	4.16	5.18
0.80	0.115	0.422	0.848	1.32	1.81
0.70	0.0583	0.212	0.425	0.678	0.950
0.60	0.0372	0.137	0.272	0.430	0.602
0.50	0.0229	0.0944	0.193	0.305	0.424
0.40	0.0153	0.0655	0.138	0.224	0.313
0.30	0.00881	0.0412	0.0941	0.158	0.229
0.20	0.00585	0.0271	0.0598	0.100	0.150
0.10	0.00239	0.013	0.0317	0.0505	0.0738

Table A1.2 Dimensionless Load Variation With Eccentricity Ratio and Width-to-Diameter Ratio (Dimensionless Supply Pressure = 0.5)

Eccentricity Ratio	Dimensionless Load Capacity ($\bar{W}$)				
(ε)	b/d = 0.1	b/d = 0.2	b/d = 0.3	b/d = 0.4	b/d = 0.5
0.96	2.42	7.57	12.3	15.9	18.5
0.94	1.15	3.82	6.60	8.90	10.6
0.92	0.671	2.19	4.13	5.76	7.02
0.90	0.411	1.59	2.93	4.17	5.15
0.80	0.117	0.424	0.850	1.29	1.73
0.70	0.0544	0.196	0.400	0.626	0.848
0.60	0.0345	0.116	0.231	0.362	0.486
0.50	0.0239	0.0753	0.152	0.231	0.304
0.40	0.0164	0.0573	0.107	0.157	0.203
0.30	0.0112	0.0410	0.0769	0.111	0.140
0.20	0.00735	0.0262	0.0532	0.0778	0.0979
0.10	0.00444	0.0129	0.0275	0.0456	0.0613

Table A1.3 Dimensionless Load Variation With Eccentricity Ratio and Width-to-Diameter Ratio (Dimensionless Supply Pressure = 0.1)

Eccentricity Ratio	Dimensionless Load Capacity ($\bar{W}$)				
(ε)	b/d = 0.1	b/d = 0.2	b/d = 0.3	b/d = 0.4	b/d = 0.5
0.96	2.42	7.57	12.31	15.9	18.4
0.94	1.15	3.82	6.59	8.90	10.5
0.92	0.671	2.19	4.13	5.76	6.93
0.90	0.411	1.58	2.92	4.12	5.01
0.80	0.117	0.423	0.837	1.24	1.61
0.70	0.0526	0.191	0.382	0.573	0.743
0.60	0.0320	0.109	0.212	0.314	0.401
0.50	0.0223	0.0712	0.132	0.190	0.237
0.40	0.0159	0.0499	0.0881	0.122	0.149
0.30	0.0108	0.0360	0.0612	0.0821	0.0984
0.20	0.00690	0.0247	0.0426	0.0566	0.0670
0.10	0.00345	0.0125	0.0255	0.0363	0.0441

Table A1.4 Dimensionless Load Variation With Eccentricity Ratio and Width-to-Diameter Ratio (Dimensionless Supply Pressure = 0.05)

Eccentricity Ratio (ε)	Dimensionless Load Capacity ($\bar{W}$)				
	b/d = 0.1	b/d = 0.2	b/d = 0.3	b/d = 0.4	b/d = 0.5
0.96	2.42	7.55	11.98	14.9	16.7
0.94	1.15	3.80	6.29	8.05	9.10
0.92	0.670	2.28	3.84	5.00	5.70
0.90	0.411	1.56	2.69	3.54	4.05
0.80	0.114	0.392	0.673	0.869	1.02
0.70	0.0496	0.162	0.264	0.334	0.384
0.60	0.0276	0.0826	0.127	0.156	0.177
0.50	0.0175	0.0472	0.0688	0.0831	0.0925
0.40	0.0120	0.0291	0.0407	0.0481	0.0529
0.30	0.00855	0.0191	0.0257	0.0297	0.0324
0.20	0.00593	0.0129	0.0170	0.0194	0.0210
0.10	0.00314	0.00835	0.0112	0.0130	0.0141

Table A1.5 Dimensionless Load Variation With Eccentricity Ratio and Width-to-Diameter Ratio (Dimensionless Supply Pressure = 0.01)

Eccentricity Ratio (ε)	Dimensionless Power Loss ($\bar{H}$)				
	b/d = 0.1	b/d = 0.2	b/d = 0.3	b/d = 0.4	b/d = 0.5
0.96	4.92	5.00	5.21	5.41	5.58
0.94	4.17	4.17	4.32	4.47	4.60
0.92	3.71	3.68	3.77	3.88	4.00
0.90	3.41	3.37	3.44	3.53	3.61
0.80	2.59	2.53	2.53	2.55	2.57
0.70	2.19	2.18	2.16	2.15	2.15
0.60	1.95	1.97	1.95	1.94	1.93
0.50	1.80	1.80	1.82	1.80	1.79
0.40	1.69	1.70	1.71	1.71	1.70
0.30	1.62	1.63	1.63	1.63	1.64
0.20	1.58	1.58	1.58	1.58	1.58
0.10	1.55	1.55	1.55	1.55	1.55

Table A1.6 Dimensionless Power Loss Variation with Eccentricity Ratio and Width-to-Diameter Ratio (Dimensionless Supply Pressure = 1.0)

Eccentricity Ratio (ε)	Dimensionless Power Loss ($\bar{H}$)				
	b/d = 0.1	b/d = 0.2	b/d = 0.3	b/d = 0.4	b/d = 0.5
0.96	4.82	4.91	5.12	5.32	5.48
0.94	4.06	4.08	4.22	4.37	4.50
0.92	3.61	3.59	3.68	3.79	3.89
0.90	3.35	3.28	3.35	3.43	3.51
0.80	2.44	2.45	2.44	2.45	2.47
0.70	2.09	2.12	2.09	2.07	2.06
0.60	1.89	1.93	1.89	1.87	1.85
0.50	1.78	1.80	1.78	1.75	1.72
0.40	1.70	1.70	1.70	1.67	1.65
0.30	1.63	1.63	1.63	1.63	1.61
0.20	1.58	1.58	1.58	1.58	1.58
0.10	1.55	1.55	1.55	1.55	1.55

Table A1.7 Dimensionless Power Loss Variation with Eccentricity Ratio and Width-to-Diameter Ratio (Dimensionless Supply Pressure = 0.5)

Eccentricity Ratio (ε)	Dimensionless Power Loss ($\bar{H}$)				
	b/d = 0.1	b/d = 0.2	b/d = 0.3	b/d = 0.4	b/d = 0.5
0.96	4.62	4.73	4.93	5.11	5.25
0.94	3.86	3.90	4.03	4.16	4.26
0.92	3.42	3.41	3.49	3.58	3.60
0.90	3.21	3.10	3.15	3.22	3.28
0.80	2.38	2.28	2.25	2.24	2.24
0.70	2.07	1.98	1.90	1.87	1.85
0.60	1.90	1.79	1.72	1.68	1.65
0.50	1.79	1.69	1.62	1.58	1.54
0.40	1.69	1.64	1.57	1.52	1.49
0.30	1.62	1.60	1.55	1.51	1.48
0.20	1.58	1.58	1.55	1.52	1.50
0.10	1.55	1.55	1.55	1.55	1.53

Table A1.8 Dimensionless Power Loss Variation with Eccentricity Ratio and Width-to-Diameter Ratio (Dimensionless Supply Pressure = 0.1)

Eccentricity Ratio (ε)	Dimensionless Power Loss ($\bar{H}$)				
	b/d = 0.1	b/d = 0.2	b/d = 0.3	b/d = 0.4	b/d = 0.5
0.96	4.55	4.60	4.84	5.00	5.10
0.94	3.79	3.83	3.90	4.05	4.13
0.92	3.34	3.33	3.40	3.47	3.52
0.90	3.06	3.02	3.05	3.10	3.12
0.80	2.30	2.20	2.15	2.13	2.13
0.70	2.00	1.88	1.81	1.77	1.70
0.60	1.83	1.72	1.64	1.59	1.59
0.50	1.74	1.62	1.54	1.50	1.50
0.40	1.68	1.57	1.50	1.46	1.46
0.30	1.62	1.55	1.49	1.45	1.46
0.20	1.58	1.55	1.51	1.47	1.48
0.10	1.55	1.55	1.54	1.52	1.53

Table A1.9 Dimensionless Power Loss Variation with Eccentricity Ratio and Width-to-Diameter Ratio (Dimensionless Supply Pressure = 0.05)

Eccentricity Ratio (ε)	Dimensionless Power Loss ($\bar{H}$)				
	b/d = 0.1	b/d = 0.2	b/d = 0.3	b/d = 0.4	b/d = 0.5
0.96	4.39	4.44	4.55	4.57	4.59
0.94	3.63	3.80	3.65	3.66	3.67
0.92	3.18	3.11	3.11	3.12	3.12
0.90	2.89	2.79	2.78	2.78	2.80
0.80	2.09	1.98	1.92	1.89	1.87
0.70	1.80	1.67	1.60	1.57	1.55
0.60	1.68	1.52	1.46	1.43	1.41
0.50	1.59	1.45	1.39	1.36	1.34
0.40	1.55	1.42	1.37	1.34	1.32
0.30	1.54	1.42	1.38	1.35	1.36
0.20	1.54	1.45	1.42	1.40	1.39
0.10	1.55	1.51	1.48	1.47	1.46

Table A1.10 Dimensionless Power Loss Variation with Eccentricity Ratio and Width-to-Diameter Ratio (Dimensionless Supply Pressure = 0.01)

```
C     ******************************************************************
      SUBROUTINE CALCS (IGAP,JGAP,M,N,B,D,PY,DX,DY)
C
C     The boundary conditions at the groove have already been set and
C     this coding represents one sweep through the finite difference
C     mesh.
C     PO(IGAP,JGAP) and P(IGAP,JGAP) are the pressures on successive
C     iterations.
C     QO(IGAP,JGAP) and Q(IGAP,JGAP) are the proportions of a mesh
C     square full of oil on successive iterations.
C     IGAP is the axial node designator.
C     JGAP is the circumferential node designator.
C     H(JGAP) is the dimensionless film thickness.
C     THETA(JGAP) is the angular displacement from the maximum film
C     thickness.
C     ******************************************************************
      IMPLICIT REAL*8 (A-H,O-Z)
C     VARIABLES TRANSFERED FROM MAIN PROGRAM.
      COMMON /Q/ Q(0:25,0:100),QO(0:25,0:100)
      COMMON /ANGLE/ H(0:100),THETA(100)
      COMMON /PBAR/ P(-5:25,-5:100),PO(-5:25,-5:100)
      BD=B/D
      DX=2*PY/M
      DY=1.0/(N-1)
      DO 2 IGAP=2,N-1
      DO 3 JGAP=1,M
      IF(Q(IGAP,JGAP).LT.0.995) THEN
      P(IGAP,JGAP)=0.0D0
      GOTO 3
      ENDIF
      IF(Q(IGAP,JGAP-1).GT.0.995)THEN
C     THIS IS THE FINITE DIFFERENCE FORM OF REYNOLDS' EQUATION.
      A1=-3*ER*SIN(THETA(JGAP))*H(JGAP)**2*(P(IGAP,JGAP+1)
     +-P(IGAP,JGAP-1))/(2*DX)
      A2=H(JGAP)**3*(P(IGAP,JGAP+1)+P(IGAP,JGAP-1))/(DX*DX)
      A3=H(JGAP)**3*(P(IGAP+1,JGAP)+P(IGAP-1,JGAP))/(4*BD*BD*DY*DY)
      A4=-6*ER*SIN(THETA(JGAP))
      A5=2*H(JGAP)**3*(1./(4*BD*BD*DY*DY)+1/(DX*DX))
      VALUE=(A1+A2+A3-A4)/A5
      ELSE
C     THIS IMPOSES FLOW CONTINUITY AT REFORMATION BOUNDARY.
      A1=(H(JGAP-1)*Q(IGAP,JGAP-1)-H(JGAP)*Q(IGAP,JGAP))*DY/2
      A2=(H(JGAP-1)+H(JGAP))**3*P(IGAP,JGAP-1)*DY/(12*8*DX)
      A3=(H(JGAP+1)+H(JGAP))**3*P(IGAP,JGAP+1)*DY/(12*8*DX)
```

```
      A4=H(JGAP)**3*P(IGAP-1,JGAP)*DX/(48*DY*BD*BD)
      A5=H(JGAP)**3*P(IGAP+1,JGAP)*DX/(48*DY*BD*BD)
      A6=-(H(JGAP)+H(JGAP-1))**3*DY/(12*8*DX)
      A7=-(H(JGAP)+H(JGAP+1))**3*DY/(12*8*DX)
      A8=-2*H(JGAP)**3*DX/(48*DY*BD*BD)
      VALUE=(-A1-A2-A3-A4-A5)/(A6+A7+A8)
      ENDIF
      P(IGAP,JGAP)=PO(IGAP,JGAP)+1.5*(VALUE-PO(IGAP,JGAP))
      IF(P(IGAP,JGAP).LT.0.0)P(IGAP,JGAP)=0
    3 CONTINUE
    2 CONTINUE
C     DETERMINATION OF Q(IGAP,JGAP) AT CAVITATED NODES.
      DO 54 IGAP=2,N-1
      DO 55 JGAP=1,M
      IF(P(IGAP,JGAP).LT.1E-6)THEN
      GRAD4=(P(IGAP+1,JGAP)-P(IGAP,JGAP))/DY
      GRAD3=(P(IGAP,JGAP)-P(IGAP-1,JGAP))/DY
      GRAD2=(P(IGAP,JGAP+1)-P(IGAP,JGAP))/DX
      GRAD1=(P(IGAP,JGAP)-P(IGAP,JGAP-1))/DX
C     DETERMINATION OF COMPONENT OIL FLOW RATES.
      QXPIN=-((H(JGAP)+H(JGAP-1))/2)**3*GRAD1*DY/12
      QXPOUT=-((H(JGAP)+H(JGAP+1))/2)**3*GRAD2*DY/12
      QXCOUT=(H(JGAP)+H(JGAP+1))*DY/4
      QXCIN=Q(IGAP,JGAP-1)*(H(JGAP-1)+H(JGAP))*DY/4
      QYPIN=-H(JGAP)**3*GRAD3*DX/(48*BD*BD)
      QYPOUT=-H(JGAP)**3*GRAD4*DX/(48*BD*BD)
      VOLSTA=H(JGAP)*DX*DY
      QSTORE=QXPIN+QXCIN+QYPIN-QXPOUT-QYPOUT
      QSTART=VOLSTA*Q(IGAP,JGAP)
      Q(IGAP,JGAP)=QSTORE/QXCOUT
      IF(Q(IGAP,JGAP).GT.0.995)Q(IGAP,JGAP)=1.0
      ELSE
      Q(IGAP,JGAP)=1
      ENDIF
   55 CONTINUE
   54 CONTINUE
      RETURN
      END
```

Figure A1.1 The Computer Coding For The Imposition Of The Jakobsson-Floberg Boundary Condition.

Appendix 2

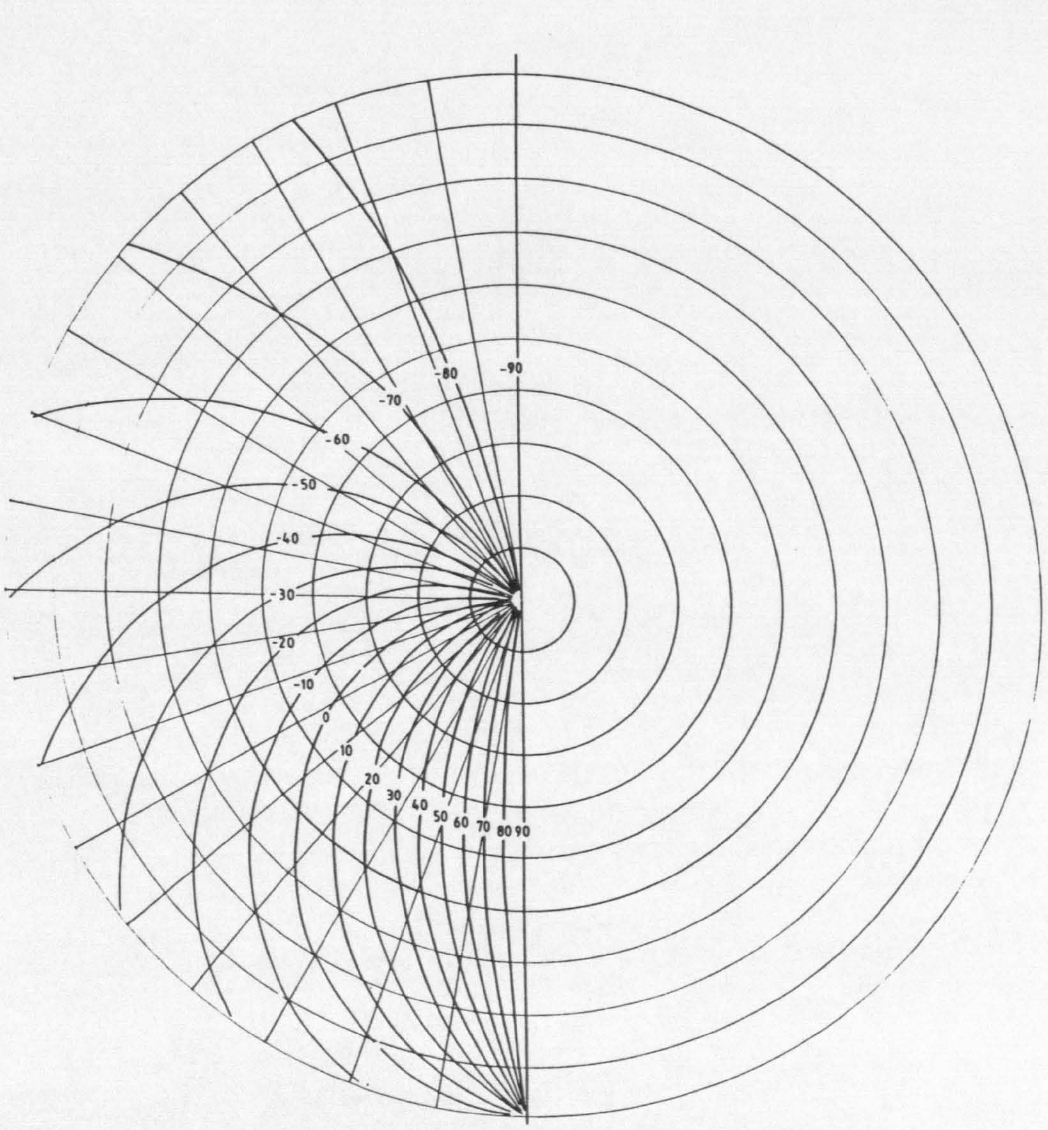

$$Q_z = \frac{2\varepsilon rbc\dot{\phi}}{\cos\theta}$$

$$Q_z = \frac{2rbc\dot{\varepsilon}}{\sin\theta}$$

Figure A2.1 Inlet Film Angle (θ_1) Variation With Attitude Angle And Eccentricity Ratio (Short Bearing Theory).

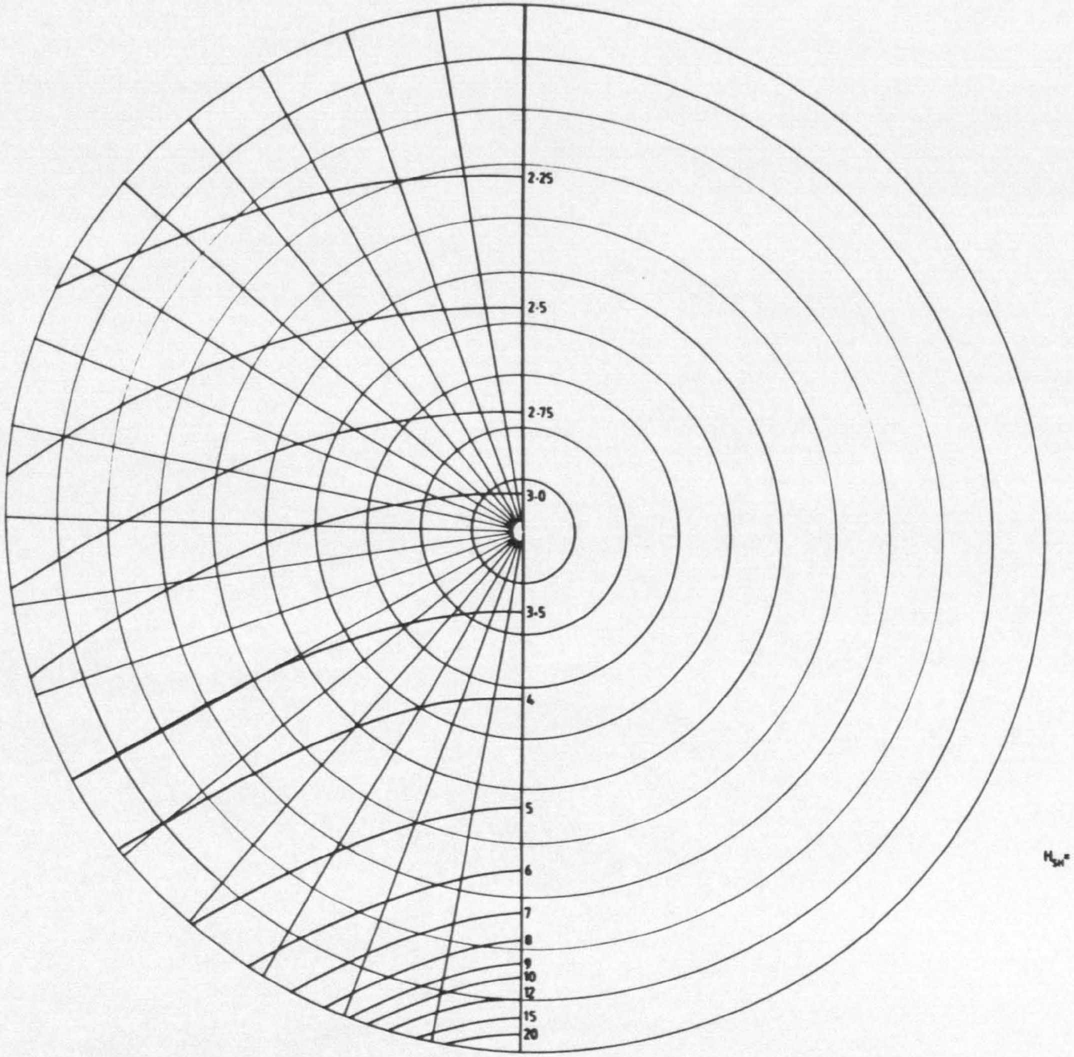

$$H_{SH} = \frac{\eta r^2 b(\Omega_S - \Omega_B)^2}{(c/r)} J_1^{\circ\circ}$$

Figure A2.2 PI Film Shear Component ($J_1^{\circ\circ}$) Variation With Attitude Angle And Eccentricity Ratio (Short Bearing Theory).

Appendix 3

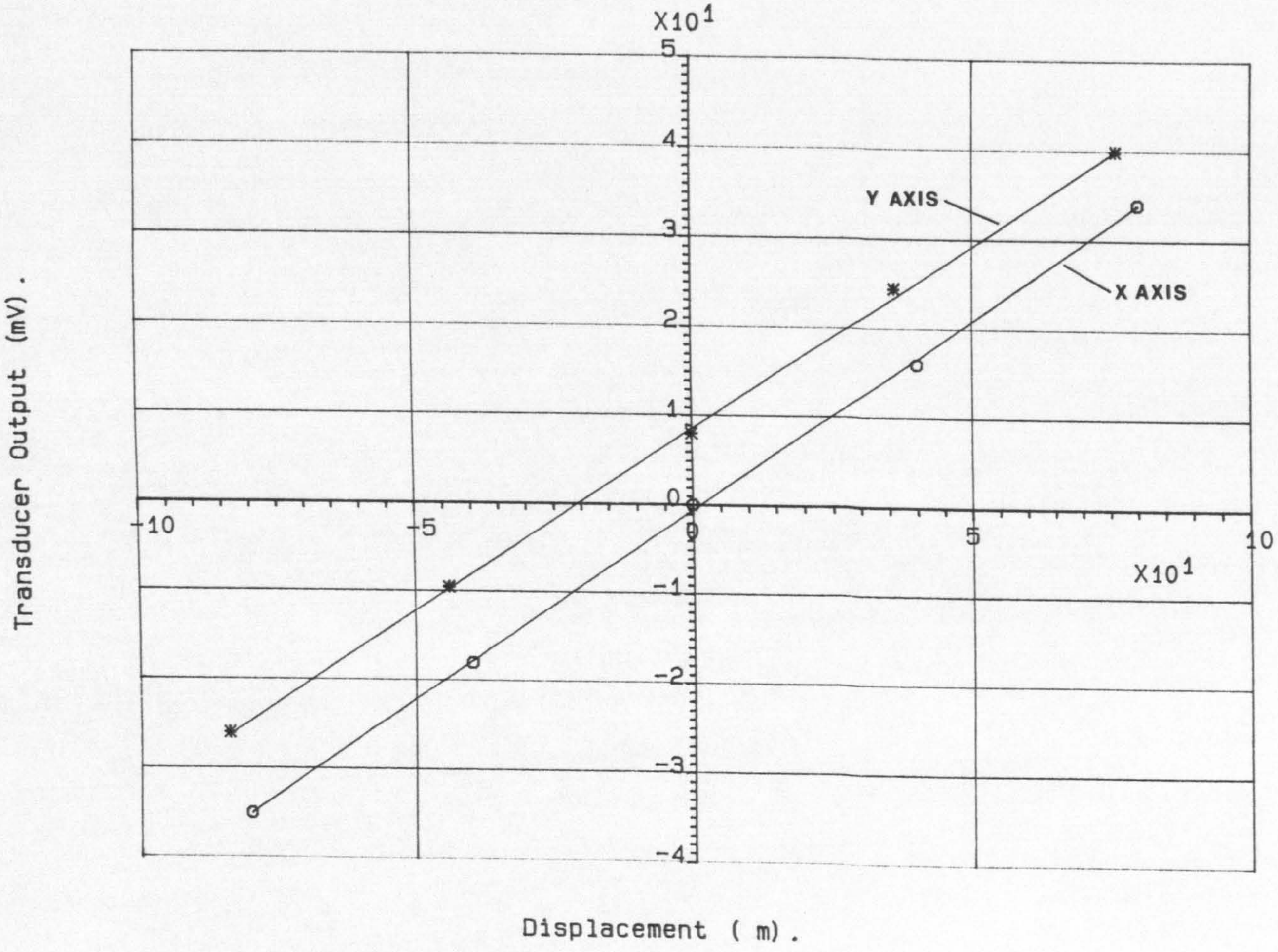

Figure A3.1 Calibration Curve For Proximity Transducers.
(Y axis curve has been moved 8mV vertically for clarity).

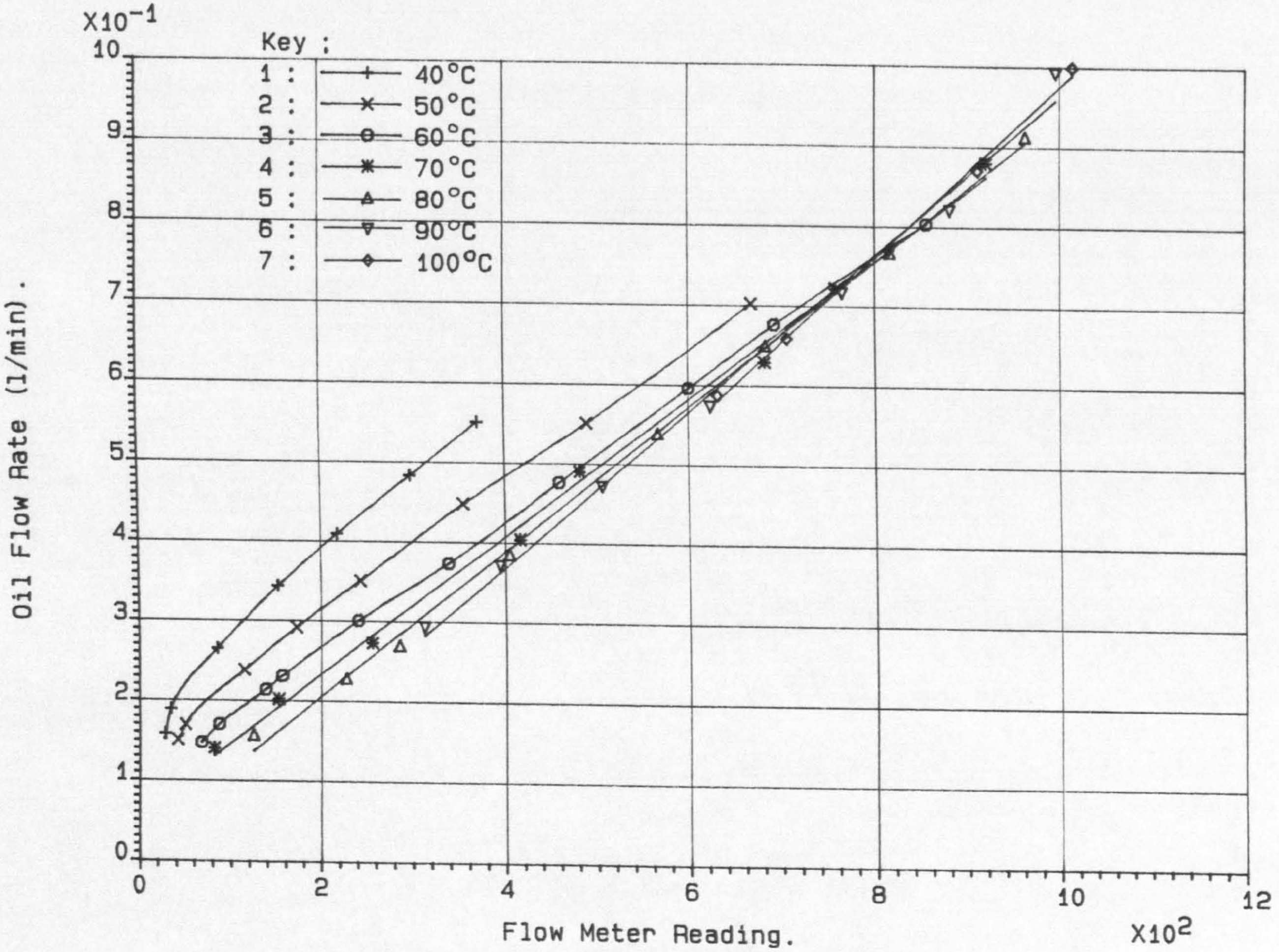

Figure A3.2 Flow Meter Calibration Curve For Shell Rotella X30.

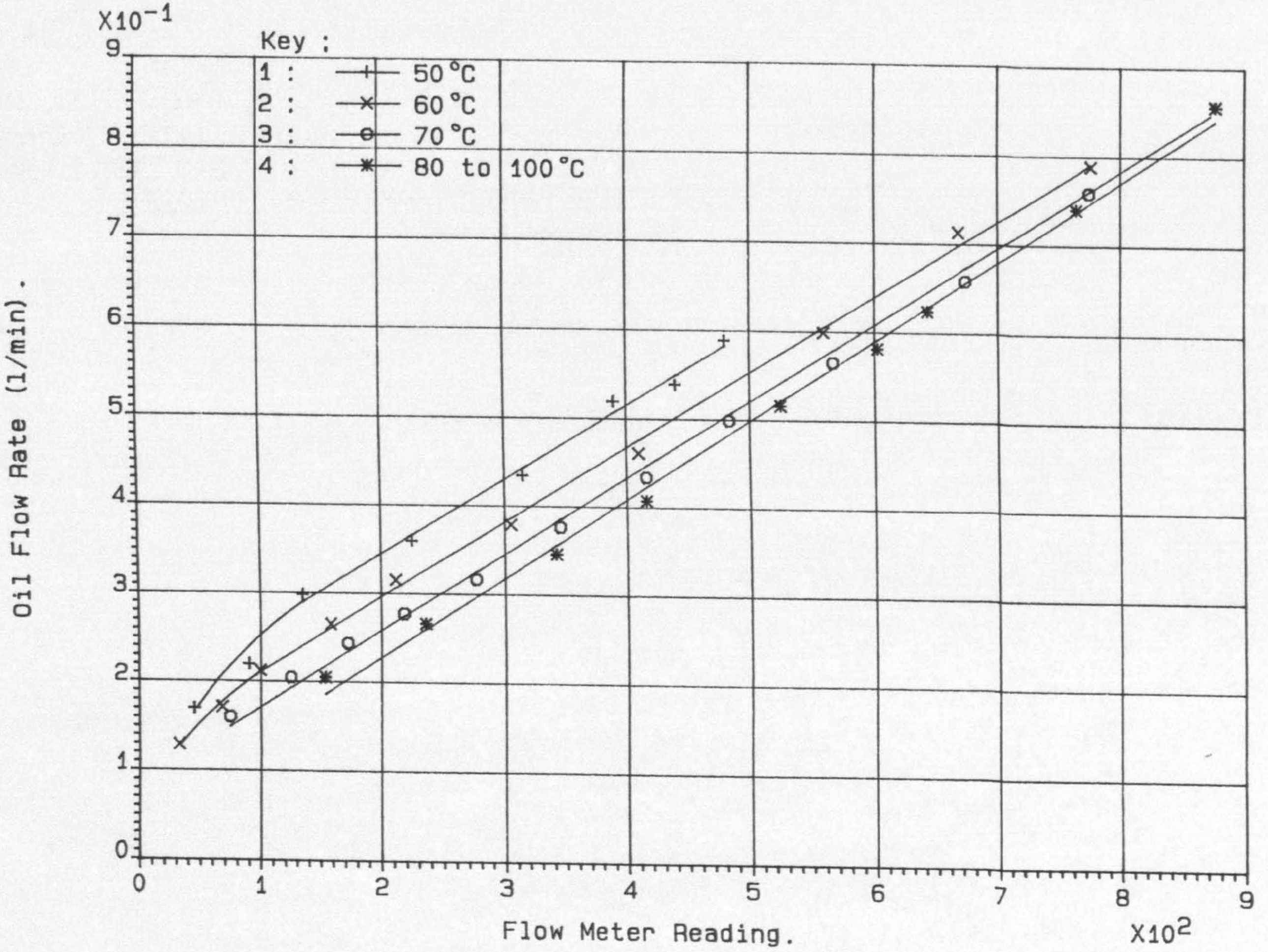

Figure A3.3 Flow Meter Calibration Curve For Shell Rotella X15W40.

Appendix 4

Crank Angle (degrees)	Total Load		Crank Angle (degrees)	Total Load	
	(N)	(degrees)		(N)	(degrees)
0	3927.4	180	360	382.6	360
10	6509.2	177	370	400.1	2
20	6966.4	174	380	409.1	4
30	5166.4	171	390	366.2	7
40	3651.1	168	400	284.9	15
50	2661.4	165	410	198.5	31
60	2051.0	162	420	145.0	68
70	1675.6	160	430	173.9	108
80	1449.3	158	440	252.6	130
90	1305.7	158	450	336.1	140
100	1209.6	158	460	413.7	146
110	1133.5	159	470	476.9	150
120	1075.4	160	480	524.0	154
130	1022.8	162	490	555.9	158
140	966.3	165	500	572.0	162
150	896.3	168	510	581.9	166
160	807.1	172	520	583.5	170
170	727.8	176	530	585.8	175
180	686.6	180	540	588.6	180
190	669.8	185	550	591.4	185
200	667.4	189	560	595.2	190
210	663.1	193	570	596.5	194
220	653.6	197	580	598.0	198
230	634.6	201	590	593.0	201
240	617.4	204	600	590.1	204
250	590.5	207	610	567.0	207
260	540.9	210	620	540.9	210
270	468.5	213	630	505.8	212
280	386.0	218	640	478.9	213
290	289.7	225	650	461.6	214
300	194.3	242	660	478.6	212
310	135.6	280	670	554.7	207
320	165.9	324	680	736.6	200
330	242.5	344	690	1073.6	193
340	312.7	353	700	1585.2	188
350	365.7	357	710	2167.1	184

Table A4.1 Ricardo Hydra Load Variation With Crank Angle
(1500 r.p.m. 15 Nm)

Crank Angle (degrees)	Total Load		Crank Angle (degrees)	Total Load	
	(N)	(degrees)		(N)	(degrees)
0	3458.3	180	360	854.2	360
10	6005.9	177	370	863.7	1
20	6564.5	173	380	843.6	3
30	4983.5	170	390	756.1	5
40	3516.5	166	400	625.6	10
50	2582.5	162	410	462.9	19
60	2037.6	159	420	311.8	41
70	1739.2	156	430	260.5	82
80	1581.0	155	440	342.4	116
90	1497.9	154	450	475.2	133
100	1453.4	155	460	604.3	142
110	1423.8	156	470	714.3	148
120	1399.0	158	480	794.9	152
130	1366.5	161	490	852.2	156
140	1323.9	164	500	884.1	161
150	1265.5	167	510	899.8	165
160	1184.0	171	520	905.7	170
170	1101.6	175	530	907.7	175
180	1040.2	180	540	910.2	180
190	1009.0	185	550	910.5	185
200	995.2	190	560	917.1	190
210	986.6	194	570	917.1	195
220	974.0	199	580	912.9	199
230	948.0	202	590	875.5	203
240	893.6	206	600	852.9	207
250	809.5	210	610	812.1	210
260	714.0	215	620	742.4	214
270	595.5	220	630	650.5	218
280	457.3	230	640	558.1	223
290	321.2	249	650	477.9	228
300	255.5	288	660	419.8	232
310	326.8	325	670	407.3	229
320	466.8	343	680	492.8	216
330	607.2	351	690	752.9	201
340	724.2	356	700	1221.6	191
350	806.9	358	710	1797.0	185

Table A4.2 Ricardo Hydra Load Variation With Crank Angle
(2000 r.p.m. 15 Nm)

Crank Angle (degrees)	Total Load		Crank Angle (degrees)	Total Load	
	(N)	(degrees)		(N)	(degrees)
0	3071.1	180	360	1454.1	360
10	5513.3	176	370	1453.6	1
20	6114.8	173	380	1400.6	2
30	4671.5	169	390	1251.6	5
40	3276.2	164	400	1039.9	8
50	2424.5	159	410	793.0	16
60	1977.5	154	420	551.0	32
70	1776.9	152	430	406.8	68
80	1717.8	151	440	477.0	108
90	1721.2	151	450	664.5	129
100	1749.5	152	460	857.9	140
110	1776.7	154	470	1023.9	146
120	1794.4	157	480	1149.9	151
130	1789.0	159	490	1235.4	156
140	1763.5	161	500	1286.6	160
150	1715.5	166	510	1312.6	165
160	1641.8	170	520	1320.2	169
170	1559.3	175	530	1324.8	175
180	1496.9	180	540	1326.5	180
190	1454.9	185	550	1330.6	185
200	1435.9	190	560	1334.6	191
210	1416.5	195	570	1335.5	195
220	1387.9	199	580	1324.1	200
230	1336.7	203	590	1324.7	204
240	1259.5	209	600	1220.5	208
250	1138.0	212	610	1147.6	212
260	971.0	217	620	1011.7	217
270	766.5	226	630	848.0	223
280	563.8	241	640	683.8	231
290	419.5	270	650	533.7	244
300	442.6	310	660	434.1	261
310	630.6	336	670	382.1	272
320	872.8	352	680	345.6	266
330	1101.4	354	690	406.9	230
340	1281.1	357	700	767.9	200
350	1396.1	359	710	1323.5	187

Table A4.3 Ricardo Hydra Load Variation With Crank Angle (2500 r.p.m. 15 Nm)

Crank Angle (degrees)	Total Load		Crank Angle (degrees)	Total Load	
	(N)	(degrees)		(N)	(degrees)
0	3060.0	180	360	2227.0	360
10	5805.3	176	370	2217.0	1
20	5991.5	172	380	2106.8	2
30	4291.1	167	390	1872.5	4
40	2939.0	160	400	1559.4	8
50	2198.3	153	410	1198.6	14
60	1876.1	149	420	840.6	29
70	1802.0	146	430	599.5	61
80	1855.4	146	440	645.4	102
90	1962.0	148	450	894.3	126
100	2078.6	150	460	1166.7	138
110	2180.0	152	470	1398.1	145
120	2246.1	155	480	1575.6	150
130	2279.8	158	490	1698.8	155
140	2275.1	162	500	1769.9	159
150	2236.7	166	510	1807.6	164
160	2170.6	170	520	1820.5	169
170	2090.6	175	530	1824.5	175
180	2022.5	180	540	1828.7	180
190	1975.4	185	550	1836.0	185
200	1942.0	190	560	1843.6	191
210	1971.7	195	570	1845.1	196
220	1883.0	200	580	1824.8	200
230	1811.6	204	590	1755.9	205
240	1699.2	208	600	1691.5	209
250	1528.5	213	610	1515.6	213
260	1303.5	219	620	1333.3	218
270	1028.1	228	630	1096.8	226
280	739.8	246	640	847.4	238
290	581.9	283	650	651.6	258
300	722.6	322	660	574.3	286
310	1041.1	341	670	599.7	308
320	1395.9	350	680	596.7	317
330	1722.0	355	690	456.3	309
340	1989.1	357	700	316.0	247
350	2160.5	359	710	789.7	193

Table A4.4 Ricardo Hydra Load Variation With Crank Angle
(3000 r.p.m. 15 Nm)

Crank Angle (degrees)	Total Load		Crank Angle (degrees)	Total Load	
	(N)	(degrees)		(N)	(degrees)
0	2819.3	180	360	3110.2	360
10	5539.7	175	370	3067.9	1
20	5388.3	170	380	2900.1	2
30	3641.5	163	390	2584.0	4
40	2438.2	154	400	2150.2	7
50	1878.2	144	410	1659.9	14
60	1731.1	139	420	1166.8	28
70	1810.6	139	430	826.8	58
80	2003.5	141	440	858.8	99
90	2239.5	144	450	1172.4	125
100	2461.6	148	460	1537.4	137
110	2649.4	151	470	1854.6	145
120	2782.1	154	480	2096.3	150
130	2852.4	157	490	2257.8	155
140	2874.4	161	500	2352.5	159
150	2852.2	165	510	2400.7	164
160	2795.0	170	520	2419.0	169
170	2717.5	175	530	2425.4	174
180	2651.4	180	540	2432.0	180
190	2601.6	185	550	2439.6	186
200	2569.2	191	560	2451.0	191
210	2536.5	196	570	2449.0	196
220	2485.2	200	580	2418.9	200
230	2393.5	205	590	2837.5	203
240	2234.3	209	600	2183.1	209
250	1995.8	214	610	1997.6	214
260	1684.0	220	620	1733.6	220
270	1317.4	231	630	1399.8	228
280	959.2	250	640	1060.4	243
290	791.9	287	650	823.1	269
300	1029.6	325	660	820.4	302
310	1503.1	343	670	981.8	324
320	2009.1	351	680	1106.4	334
330	2447.4	355	690	1029.5	337
340	2794.0	358	700	689.9	332
350	3018.4	359	710	210.7	252

Table A4.5 Ricardo Hydra Load Variation With Crank Angle (3500 r.p.m. 15 Nm)

Crank Angle (degrees)	Total Load		Crank Angle (degrees)	Total Load	
	(N)	(degrees)		(N)	(degrees)
0	2565.2	180	360	4165.9	360
10	5346.1	174	370	4104.1	1
20	4868.7	169	380	3848.0	2
30	3122.9	159	390	3417.7	4
40	2065.2	145	400	2840.0	7
50	1685.7	133	410	2192.6	14
60	1700.4	129	420	1542.1	27
70	1919.4	132	430	1099.3	55
80	2598.4	137	440	1111.0	98
90	2598.4	142	450	1507.2	124
100	2941.4	146	460	1983.3	137
110	3219.3	150	470	2387.9	144
120	3422.2	153	480	2694.8	150
130	3543.3	157	490	2909.3	155
140	3589.7	161	500	3036.6	159
150	3577.2	165	510	3094.1	164
160	3525.9	170	520	3115.4	169
170	3453.5	175	530	3123.9	174
180	3386.7	180	540	3129.8	180
190	3334.9	185	550	3140.7	186
200	3300.7	191	560	3155.9	191
210	3259.0	196	570	3154.6	196
220	3189.6	200	580	3114.4	201
230	3065.5	205	590	3527.7	203
240	2858.6	209	600	2728.4	210
250	2548.5	214	610	2503.0	215
260	2136.8	221	620	2180.4	221
270	1652.2	232	630	1740.2	230
280	1198.6	254	640	1303.2	247
290	1042.1	293	650	1044.5	277
300	1391.0	327	660	1142.3	311
310	2006.2	344	670	1452.7	331
320	2678.5	352	680	1720.6	341
330	3286.5	356	690	1755.1	345
340	3755.3	358	700	1472.1	346
350	4053.4	359	710	697.8	341

Table A4.6 Ricardo Hydra Load Variation With Crank Angle (4000 r.p.m. 15 Nm)

Crank Angle (degrees)	Total Load		Crank Angle (degrees)	Total Load	
	(N)	(degrees)		(N)	(degrees)
0	2618.0	180	360	5323.2	360
10	5368.9	174	370	5230.0	1
20	4254.5	166	380	4898.3	2
30	2541.4	152	390	4327.6	4
40	1713.9	130	400	3611.4	7
50	1566.4	116	410	2794.5	13
60	1721.4	117	420	1964.2	27
70	2059.5	125	430	1376.7	57
80	2514.5	133	440	1398.7	98
90	3016.6	140	450	1897.6	124
100	3483.4	145	460	2487.1	137
110	3874.7	149	470	2997.6	144
120	4150.4	153	480	3390.6	150
130	4318.0	156	490	3649.8	154
140	4398.6	160	500	3811.2	159
150	4405.7	165	510	3890.7	164
160	4360.4	170	520	3915.8	169
170	4281.4	175	530	3920.0	174
180	4219.6	180	540	3925.8	180
190	4168.4	185	550	3939.9	186
200	4135.0	191	560	3958.5	191
210	4090.3	196	570	3954.3	196
220	4010.2	200	580	3903.2	201
230	3855.9	205	590	4579.1	203
240	3596.3	209	600	3495.5	210
250	3203.1	214	610	3209.6	214
260	2691.8	221	620	2697.2	221
270	2077.6	232	630	2135.4	231
280	1506.3	254	640	1590.0	250
290	1324.0	294	650	1310.1	282
300	1791.2	328	660	1516.6	316
310	2583.0	344	670	1991.6	335
320	3418.4	352	680	2420.6	344
330	4174.2	356	690	2589.8	348
340	4772.8	358	700	2381.8	350
350	5168.3	359	710	1278.0	348

Table A4.7 Ricardo Hydra Load Variation With Crank Angle
(4500 r.p.m. 15 Nm)

Crank Angle (degrees)	Total Load		Crank Angle (degrees)	Total Load	
	(N)	(degrees)		(N)	(degrees)
0	537.7	180	360	6548.7	360
10	3689.5	171	370	6452.8	1
20	3619.1	162	380	6025.1	2
30	2157.2	142	390	5371.5	4
40	1598.9	113	400	4462.1	7
50	1646.1	101	410	3430.6	14
60	1888.0	108	420	2417.5	27
70	2323.9	121	430	1700.8	56
80	2913.3	131	440	1734.6	98
90	3557.4	139	450	2332.7	123
100	4158.0	144	460	3055.0	136
110	4643.9	148	470	3694.5	144
120	5009.3	152	480	4174.3	150
130	5243.1	156	490	4491.1	154
140	5355.5	160	500	4695.5	159
150	5359.4	165	510	4776.6	164
160	5310.4	169	520	4816.3	169
170	5247.2	175	530	4819.5	174
180	5179.0	180	540	4823.6	180
190	5126.4	185	550	4845.3	186
200	5093.4	191	560	4856.6	191
210	5041.7	196	570	4850.9	196
220	4944.4	200	580	4790.7	201
230	4753.2	205	590	4702.7	205
240	4435.7	209	600	4331.4	210
250	3953.3	214	610	5625.8	209
260	3320.8	221	620	3306.9	221
270	2573.7	232	630	2582.0	232
280	1865.5	254	640	1913.6	252
290	1631.4	293	650	1614.9	285
300	2200.9	328	660	1950.6	319
310	3177.5	344	670	2603.3	337
320	4213.6	352	680	3206.5	346
330	5149.1	356	690	3507.1	350
340	5881.1	358	700	3383.5	352
350	6362.6	359	710	2677.6	354

Table A4.8 Ricardo Hydra Load Variation With Crank Angle (5000 r.p.m. 15 Nm)

Crank Angle (degrees)	Total Load		Crank Angle (degrees)	Total Load	
	(N)	(degrees)		(N)	(degrees)
0	782.9	360	360	7912.3	360
10	2538.8	166	370	7760.6	1
20	2905.2	156	380	7304.4	2
30	1781.0	124	390	6480.9	4
40	1645.8	90	400	5387.7	7
50	1838.9	86	410	4152.2	14
60	2096.5	99	420	2937.7	27
70	2588.4	116	430	2064.1	56
80	3308.1	129	440	2073.3	97
90	4108.6	137	450	2825.1	123
100	4867.9	143	460	3693.9	136
110	5486.9	148	470	4453.8	144
120	5945.4	152	480	5042.1	150
130	6230.7	156	490	5436.5	154
140	6376.4	160	500	5670.2	159
150	6414.7	165	510	5773.6	164
160	6355.1	169	520	5808.7	169
170	6291.2	175	530	5814.3	174
180	6209.9	180	540	5820.4	180
190	6155.6	185	550	5837.3	186
200	6115.1	191	560	5860.6	191
210	6059.5	196	570	5848.0	196
220	5927.3	201	580	5770.6	201
230	5701.5	205	590	5753.1	205
240	5313.4	210	600	5178.2	210
250	4741.2	215	610	4645.9	215
260	3979.0	222	620	3932.4	222
270	3094.7	233	630	3065.7	233
280	2254.0	254	640	2285.3	253
290	1974.8	294	650	1955.8	288
300	2662.5	328	660	2416.5	321
310	3843.5	344	670	3276.0	339
320	5097.1	352	680	4073.1	347
330	6218.8	356	690	4520.0	351
340	7109.1	358	700	4493.4	354
350	7682.2	359	710	3879.5	356

Table A4.9 Ricardo Hydra Load Variation With Crank Angle
(5500 r.p.m. 15 Nm)

Appendix 5

Oil Supply Pressure	Effective Oil Temperature (°C)			Inlet Oil Temperature (°C)	Oil Flow Rate (Q)
(kN/m^2)	T_o	T_{av}	T_5	T_{in}	m^3/s x10^6
310.3	80.0	78.6	75.6	66.0	8.32
275.8	80.0	78.6	75.7	68.0	7.26
241.3	80.0	78.7	75.7	66.0	6.27
206.8	80.0	78.6	75.7	66.0	5.28
172.4	80.0	78.5	75.4	64.0	4.21
137.9	80.0	78.4	73.6	60.0	3.42

Table A5.1 Experimental Data for Figures 7.1 and 7.3 (2500 rpm)

Oil Supply Pressure	Effective Oil Temperature (°C)			Inlet Oil Temperature (°C)	Oil Flow Rate (Q)
(kN/m^2)	T_o	T_{av}	T_5	T_{in}	m^3/s x10^6
310.3	80.0	77.4	73.7	58.0	7.40
275.8	80.0	77.2	73.5	56.0	6.61
241.3	80.0	77.0	73.4	54.0	5.62
206.8	80.0	76.8	73.6	52.0	4.86
172.4	80.0	76.9	73.7	52.0	4.20
137.9	80.0	76.5	73.5	50.0	3.72

Table A5.2 Experimental Data for Figures 7.2 and 7.4 (3500 rpm)

Journal Rotational Frequency	Effective Oil Temperature (°C)			Inlet Oil Temperature (°C)	Oil Flow Rate (Q)
(rpm)	T_o	T_{av}	T_5	T_{in}	$m^3/s \times 10^6$
1500	80.0	79.6	78.4	74.0	5.02
2000	80.0	79.1	77.7	70.0	4.80
2500	80.0	78.5	75.9	65.0	4.66
3000	80.0	77.6	75.3	56.0	4.23
3500	100.0	98.7	95.8	87.0	7.37
4000	100.0	97.5	94.4	80.0	7.45
4500	100.0	96.4	94.7	72.0	7.10
5000	100.0	95.0	92.3	63.0	6.37
5500	100.0	94.4	90.2	53.0	5.92

Table A5.3 Experimental Data for Figures 7.5, 7.6 and 7.7
(P_s = 172.4 kN/m^2)

Journal Rotational Frequency	Effective Oil Temperature (°C)			Inlet Oil Temperature (°C)	Oil Flow Rate (Q)
(rpm)	T_o	T_{av}	T_5	T_{in}	$m^3/s \times 10^6$
1500	64.6	64.1	61.6	55.0	5.23
2000	67.7	66.7	63.8	55.0	5.50
2500	70.9	69.3	65.9	55.0	5.60
3000	75.1	72.6	68.6	55.0	6.39
3500	79.4	76.5	72.2	55.0	7.17
4000	83.7	80.7	77.1	55.0	7.86

Table A5.4 Experimental Data for Figures 7.8, 7.9 and 7.10
(P_s = 310.3 kN/m^2)

Journal Rotational Frequency	Effective Oil Temperature (°C)			Inlet Oil Temperature (°C)	Oil Flow Rate (Q)
(rpm)	T_o	T_{av}	T_5	T_{in}	$m^3/s \ x10^6$
3000	100.7	99.6	97.7	95.0	14.9
3500	102.4	101.7	99.4	95.0	15.7
4000	104.7	104.2	101.6	95.0	16.1
4500	107.4	107.1	104.5	95.0	16.3
5000	110.5	110.4	108.7	95.0	17.5
5500	112.8	113.2	112.5	95.0	17.7

Table A5.5 Experimental Data for Figures 7.8 to 7.13 ($P_s = 310.3$ kN/m^2)

Journal Rotational Frequency	Effective Oil Temperature (°C)			Inlet Oil Temperature (°C)	Oil Flow Rate (Q)
(rpm)	T_o	T_{av}	T_5	T_{in}	$m^3/s \ x10^6$
1500	76.0	75.5	73.9	70.0	7.71
2000	78.1	77.2	75.1	70.0	7.82
2500	80.7	79.3	76.7	70.0	8.21
3000	83.8	81.8	78.6	70.0	8.60
3500	87.1	85.0	81.4	70.0	9.40
4000	90.9	88.6	84.9	70.0	10.02
4500	94.8	92.8	89.4	70.0	10.60
5000	97.1	95.5	92.6	70.0	11.20
5500	99.7	98.6	92.7	70.0	11.50

Table A5.6 Additional Experimental Data (Rotella X30, $P_s = 310.3$ kN/m^2)

Journal Rotational Frequency (rpm)	Effective Oil Temperature (°C)			Inlet Oil Temperature (°C)	Oil Flow Rate (Q)
	T_o	T_{av}	T_5	T_{in}	m^3/s x10^6
1500	88.4	88.0	87.2	85.0	11.2
2000	89.8	89.1	87.8	85.0	11.4
2500	91.4	90.5	88.6	85.0	11.7
3000	93.1	92.0	89.5	85.0	12.1
3500	96.3	95.2	92.1	85.0	12.7
4000	99.1	98.0	94.8	85.0	13.5
4500	102.0	101.0	97.9	85.0	13.8
5000	104.5	104.1	101.8	85.0	14.6
5500	106.8	106.8	105.7	85.0	15.1

Table A5.7 Additional Experimental Data (Rotella X30, P_s=310.3 kN/m^2)

Oil Supply Pressure (kN/m^2)	Effective Oil Temperature (°C)			Inlet Oil Temperature (°C)	Oil Flow Rate (Q)
	T_o	T_{av}	T_5	T_{in}	m^3/s x10^6
379.2	100.0	99.3	99.0	98.0	14.4
344.7	100.0	99.3	99.0	98.0	13.3
310.3	100.0	99.4	99.0	98.0	12.0
275.8	100.0	99.4	99.0	98.0	10.5
241.3	100.0	99.5	99.1	98.0	9.22
206.8	100.0	99.5	99.1	98.0	7.86
172.4	100.0	99.7	99.1	97.0	7.02
137.9	100.0	99.5	98.8	96.0	5.90

Table A5.8 Additional Experimental Data (Rotella X15W/40, 1500rpm)

Oil Supply Pressure	Effective Oil Temperature (°C)			Inlet Oil Temperature (°C)	Oil Flow Rate (Q)
	T_o	T_{av}	T_5	T_{in}	m^3/s x10^6
413.7	80.0	77.8	74.6	63.0	9.68
379.2	80.0	77.7	74.4	62.0	8.63
344.7	80.0	77.3	74.0	59.0	7.40
310.3	80.0	77.3	73.9	58.0	6.67
275.8	80.0	77.0	73.6	57.0	5.42
241.3	80.0	76.9	73.5	57.0	4.42
206.8	80.0	76.9	73.5	52.0	3.27
172.4	80.0	76.8	73.5	48.0	2.37

Table A5.9 Additional Experimental Data (Rotella X15W/40, 3500rpm)

Journal Rotational Freqency (rpm)	Effective Oil Temperature (°C)			Inlet Oil Temperature (°C)	Oil Flow Rate (Q)
	T_o	T_{av}	T_5	T_{in}	m^3/s x10^6
1500	80.0	79.6	78.2	74.0	4.54
2000	80.0	79.1	77.1	70.0	4.43
2500	80.0	78.3	75.6	63.0	4.79
3000	80.0	76.9	73.6	55.0	4.65
3500	100.0	98.6	95.8	87.0	6.91
4000	100.0	97.5	94.5	78.0	6.95
4500	100.0	97.4	94.9	70.0	6.69

Table A5.10 Additional Experimental Data (Rotella X15W/40, P_s = 172.4 kN/m^2)